

IN SITU THREE-DIMENSIONAL RECONSTRUCTION OF MOUSE HEART
SYMPATHETIC INNERVATION BY TWO-PHOTON EXCITATION
FLUORESCENCE IMAGING

Kim Renee Freeman

Submitted to the faculty of the University Graduate School
in partial fulfillment of the requirements
for the degree
Doctor of Philosophy
in the Program of Biomedical Imaging and Biophysics,
Indiana University

August 2013

Accepted by the Faculty of Indiana University, in partial fulfillment of the requirements for the degree of Doctor of Philosophy.

Michael Rubart von der Lohe, M.D., Chair

Simon J. Atkinson, Ph.D.

Doctoral Committee

Thomas D. Hurley, Ph.D.

April 30, 2013

Vincent H. Gattone II, Ph.D.

DEDICATION

For my daughter, Taylor May. I worked on this story for you. When I started it, I didn't realize that little girls grow faster than scientific know-how. As a result you have witnessed the struggles of attaining a foothold in an educated society. I can only hope that someday you will understand why we sacrificed. I love you.

ACKNOWLEDGEMENTS

This work was supported by a CTSI Predoctoral Training Award in Translational Research to Kim Freeman, a Biomedical Imaging Applications in Translational Research Award to Michael Rubart, and an NHLBI R01 HL075165 to Michael Rubart.

It is of utmost imperativeness to also acknowledge the many people who played a part in attaining this degree. First, to the members of my committee: Dr. Atkinson, you took a chance on me and it is most appreciated. When others turned their back, you stood tall and showed me what could be accomplished. Thank you for providing the path to follow. Dr. Hurley, your guidance throughout my graduate studies has been crucial in shaping who I am today, thank you. No one else could have beaten crystallography into my head. Dr. Gattone, you widened my imaging horizons and brought new aspects to this endeavor, thank you for being a part of this journey.

There are so many others to thank. Those who supported me, cheered me on, bought the Girl Scout cookies, and shared so many smiles. I cannot thank everyone enough. There are a special few who must be mentioned, though. Dr. Soonpaa: for being a shoulder to cry on, a friend at my side, and for feeding my chocolate addiction; Dr. Field, for teaching me that getting flipped off doesn't always mean what I think it means; Sean Reauter, for "man riding on a horse", that got me through some pretty dark times; Dr. Payne, for giving my daughter someone to admire; and of course Dr. Rubart: your patience has been never-ending with this project. You let me fail and helped me stumble through to find the right path. You gave me the freedom to make mistakes, to try new things, and to learn to think on my own. I am forever grateful to you. Ich werde immer halten Sie in den höchsten Respekt. Du bist ein wahrer Mentor. Ich danke Ihnen von ganzem Herzen.

ABSTRACT

Kim Renee Freeman

In situ three-dimensional reconstruction of mouse heart sympathetic innervation by two-photon excitation fluorescence imaging

The sympathetic nervous system strongly modulates the contractile and electrical function of the heart. The anatomical underpinnings that enable a spatially and temporally coordinated dissemination of sympathetic signals within the cardiac tissue are only incompletely characterized. In this work we took the first step of unraveling the *in situ* 3D microarchitecture of the cardiac sympathetic nervous system. Using a combination of two-photon excitation fluorescence microscopy and computer-assisted image analyses, we reconstructed the sympathetic network in a portion of the left ventricular epicardium from adult transgenic mice expressing a fluorescent reporter protein in all peripheral sympathetic neurons. The reconstruction revealed several organizational principles of the local sympathetic tree that synergize to enable a coordinated and efficient signal transfer to the target tissue. First, synaptic boutons are aligned with high density along much of axon-cell contacts. Second, axon segments are oriented parallel to the main, i.e., longitudinal, axes of their apposed cardiomyocytes, optimizing the frequency of transmitter release sites per axon/per cardiomyocyte. Third, the local network was partitioned into branched and/or looped sub-trees which extended both radially and tangentially through the image volume. Fourth, sub-trees arrange to not much overlap, giving rise to multiple annexed innervation domains of variable complexity and configuration. The sympathetic network in the epicardial border zone of a chronic myocardial infarction was observed to undergo substantive remodeling, which included almost complete loss of fibers at depths $>10\ \mu\text{m}$ from the surface, spatially heterogeneous gain of axons, irregularly shaped synaptic boutons, and formation of axonal plexuses composed of nested loops of variable length. In conclusion, we provide, to the best of our knowledge, the first *in situ* 3D reconstruction of the local cardiac sympathetic network in normal and injured

mammalian myocardium. Mapping the sympathetic network connectivity will aid in elucidating its role in sympathetic signal transmission and processing.

Michael Rubart von der Lohe, M.D., Chair

TABLE OF CONTENTS

I.	INTRODUCTION	1
A.	The mammalian peripheral sympathetic nervous system	1
1.	General function	1
2.	Anatomy of the peripheral sympathetic nervous system	1
3.	Sympathetic neurotransmitters	2
4.	Neuroeffector junctions	3
B.	The cardiac sympathetic nervous system	4
1.	Physiological effects of sympathetic nerve stimulation in the heart	4
2.	Previous studies on the distribution of sympathetic nerves in adult mammalian heart	4
3.	Long-term effects of sympathetic innervation on cardiac functional and structural properties	8
4.	Sympathetic remodeling in the adult diseased heart	9
C.	Current gaps of knowledge on cardiac sympathetic innervations	12
D.	Two-photon excitation fluorescence microscopy	13
1.	Principle of two-photon excitation fluorescence microscopy	13
2.	Biological applications of two-photon excitation fluorescence microscopy	15
3.	Cell lineage-restricted expression of green fluorescent protein and its variants for in vivo labeling	16
E.	Hypotheses	18
II.	MATERIALS AND METHODS	20
A.	Generation and identification of transgenic mice expressing enhanced green fluorescent protein in peripheral sympathetic neurons	20
B.	Immunolabeling	21
C.	EGFP expression in sympathetic ganglia	23
D.	Measurement of cardiac sympathetic nerve density	24

E.	EGFP expression in intracardiac sympathetic nerves - quantitative co-localization analyses	24
1.	Immunolabeling and confocal imaging parameters	24
2.	Specificity of primary antibodies and signal bleed through	25
3.	Image pre-processing.....	27
4.	Calculation of Pearson's coefficient.....	27
5.	Calculation of Mander's 1 and Mander's 2 coefficients	28
F.	Transmembrane action potential recording in isolated postganglionic sympathetic neurons	29
G.	Two-photon laser scanning microscopy (TPLSM) of Langendorff-perfused mouse heart.....	30
1.	Description of the two-photon excitation imaging system	30
2.	Heart preparation for TPLSM imaging.....	30
3.	TPLSM image acquisition parameters.....	31
4.	Image pre-processing.....	32
H.	Permanent coronary artery occlusion.....	35
I.	Statistical Analyses	36
III.	RESULTS	37
A.	Transgene expression in postganglionic sympathetic neurons	37
B.	Intramyocardial EGFP distribution tracks sympathetic nerves in hD β H-EGFP hearts-quantitative co-localization analyses	39
C.	Live morphology of the local sympathetic network in left ventricular subepicardium as reconstructed from two-photon imaging data	41
D.	Live morphology of the remodeled sympathetic innervation in the peri-infarct border zone	48
IV.	DISCUSSION	55
V.	REFERENCES	121
	CIRRICULUM VITAE	

LIST OF FIGURES

Figure 1.	The autonomic nervous system	65
Figure 2.	Anatomy of sympathetic pathways.....	66
Figure 3.	Norepinephrine synthesis pathway	66
Figure 4.	Cartoon depicting the anatomy of the cardiac sympathetic innervations.....	67
Figure 5.	Optical system of a confocal laser scanning microscope	68
Figure 6.	Comparison between epifluorescent and confocal microscopic images.....	69
Figure 7.	Comparison of fluorescence distribution within a fluorophore-containing solution during single-photon and dual-photon excitation.....	70
Figure 8.	Schematic of the hD β H-EGFP transgene	71
Figure 9.	Specificity of primary antibodies used for co-localization analyses.....	72
Figure 10.	Examination of fluorescence signal bleed through between channels.....	73
Figure 11.	Image pre-processing for co-localization analyses.....	74
Figure 12.	Two-photon laser scanning microscope.....	75
Figure 13.	Heart perfusion chamber used for TPLSM imaging	76
Figure 14.	Two-photon excitation-induced tissue autofluorescence and EGFP fluorescence	77
Figure 15.	Removal of tissue autofluorescence	80
Figure 16.	Flow chart of image pre-processing steps for 3D neuron tracking	81
Figure 17.	Expression of hD β H-EGFP in peripheral sympathetic neurons	82
Figure 18.	EGFP expression in the soma and proximal dendrites of postganglionic sympathetic neurons	83
Figure 19.	EGFP is expressed in intracardiac portions of postganglionic sympathetic neurons	84
Figure 20.	Adult transgenic hD β H-EGFP hearts are structurally normal	85
Figure 21.	Prolonged EGFP expression does not alter neuron density in peripheral sympathetic ganglia or their electrical properties	86

Figure 22.	Adult transgenic hearts have normal sympathetic innervation density.....	88
Figure 23.	Determination of the empirical upper and lower limits of co-localization	90
Figure 24.	Intracardiac distribution of EGFP tracks sympathetic nerves	91
Figure 25.	Rare example of an intracardiac TH-expressing nerve not expressing EGFP	92
Figure 26.	Three-dimensional reconstruction of the sympathetic neurite network within a portion of the outermost left ventricular epicardial layer in a living, adult hD β H-EGFP heart.....	93
Figure 27.	Similar morphology of intramural sympathetic neurites in living and fixed cardiac tissue	98
Figure 28.	Method for semi-automated 3D skeletonization of axonal arbors from two-photon imaging stacks	100
Figure 29.	User invariance of 3D neurite tracing	102
Figure 30.	3D rendering of skeletonized sympathetic arbors within a finite volume of the left ventricular subepicardium.....	105
Figure 31.	Branching pattern of sympathetic subtrees	107
Figure 32.	Subtree arbors arrange to not overlap very much within the local sympathetic network.....	108
Figure 33.	Sympathetic remodeling in chronically infarcted myocardium.....	109
Figure 34.	Determination of the empirical upper and lower limits of co-localization in infarcted non-transgenic heart.....	112
Figure 35.	Intracardiac distribution of EGFP tracks sympathetic axons in chronically infarcted heart	113
Figure 36.	Three-dimensional reconstruction of the local sympathetic neurite network within the epicardial border zone of a 2 week old myocardial infarction in a living, adult hD β H-EGFP heart.....	114
Figure 37.	3D rendering of the skeletonized sympathetic arbor within a finite volume of the epicardial border zone of a 2 week old myocardial infarction in a living hD β H-EGFP heart.....	118
Figure 38.	Multiple-loop architecture of the sympathetic circuitry in the epicardial infarct border zone.....	119

LIST OF ABBREVIATIONS

ACH	acetylcholine
AV	atrialventricular
BSA	bovine serum albumin
Ca ⁺⁺	calcium
cAMP	cyclic adenosine monophosphate
CARS	coherent anti-stokes raman scattering
CICR	calcium induced calcium release
CLSM	confocal laser scanning microscopy
Cx43	connexin 43
DAG	diacyl glycerol
D β H	dopamine beta hydroxylase
eGFP	enhanced green fluorescent protein
GPCR	G-protein coupled receptor
GAP-43	growth associated protein-43
hD β H	human dopamine beta hydroxylase promoter
IP ₃	inositol triphosphate
K ⁺	potassium
LAD	left anterior descending
M ₁	Manders' Coefficient for channel 1
M ₂	Manders' Coefficient for channel 2
MI	myocardial infarction
mPrm1	murine protamine 1 gene
Na ⁺	sodium
NE	norepinephrine
NGF	nerve growth factor
NPY	neuropeptide y
NSC	neural stem cell
PBS	phosphate buffered saline
PKA	protein kinase A

PKC	protein kinase C
PMT	photomultiplier tube
PSF	point spread function
r_p	Pearson's Coefficient
SA	sinoatrial
SCI	spinal cord injury
SNS	sympathetic nervous system
SR	sarcoplasmic reticulum
STED	stimulated emission depletion
TH	tyrosine hydroxylase
TPE	two-photon excitation
TPLSM	two-photon laser scanning microscopy

INTRODUCTION

A. The mammalian peripheral sympathetic nervous system

1. General function

The sympathetic nervous system (SNS) is the branch of the Autonomic Nervous System responsible for the famed “fight-or-flight” response to stress, as well as general regulation and maintenance of physiological homeostatic environments in living organisms. It has broad ranging effects throughout multiple organ systems and is highly concentrated in sensory input and essential organ function. Working opposite the parasympathetic system, SNS activation results in: pupil dilation, bronchiole expansion, increases cardiac output, and inhibits peristalsis among other effects.

2. Anatomy of the peripheral sympathetic nervous system

Preganglionic sympathetic nerves originating in the spinal column conduct impulses from the central nervous system to postganglionic sympathetic neurons located in the paravertebral ganglia^[1] (Figure 1). The vast majority of postganglionic sympathetic neurons innervating the mammalian heart originate in the cervical and stellate ganglia (also known as superior thoracic ganglia)^[2] (Figure 1).

Electrical excitation of preganglionic fibers induces release of the neurotransmitter acetylcholine (ACH) from their presynaptic vesicles (Figure 2). ACH binds to nicotinic ACH receptors located in the postsynaptic membrane of postganglionic sympathetic neurons, causing postsynaptic excitatory potentials via influx of monovalent cations. Spatial and/or temporal summation of subthreshold excitatory potentials can give rise to a regenerative action potential which travels along the axon to the target organ. These axons can be approximately 1 cm long in small rodents and up to 25 cm long in the human body. Postganglionic sympathetic fiber morphology differs drastically from that of other neurons,

e.g. motor neurons. Once a fiber enters the vicinity of an effector, it can branch to form a fiber plexus^[1]. Along this plexus the fibers develop varicosities, which are known to house neurotransmitter vesicles (Figure 2). Action potentials propagating down the axon can successively trigger transmitter release from all varicosities along that axon.

The actual contact zone between a sympathetic neurite and a myocyte has been studied in-depth by the Kobilka laboratory, using co-cultures of ganglionic sympathetic neurons and cardiomyocytes. They found morphologically distinct nerve-muscle contact regions, where the two cell types are linked through cadherin-catenin domains. Functional domains are also present in these contact zones. β -adrenergic receptor subtypes exhibit distinct distribution patterns throughout the myocyte outer membrane. β -1 receptors accumulate in the contact zone, whilst β -2 receptors are excluded from them after stimulation of neural activity^[3]. It is believed that differences in receptor membrane organization play a role in heart failure pathogenesis and differences in cardiac response to acute and chronic stressors.

3. Sympathetic neurotransmitters

The predominant neurotransmitter in postganglionic sympathetic neurons is norepinephrine, although there is a vast heterogeneity and a myriad of other neurotransmitters either singularly or co-expressed. Synthesis of norepinephrine (NE) from its precursor tyrosine in postganglionic fibers requires the enzymes tyrosine hydroxylase (TH), dopa decarboxylase, and dopamine- β -hydroxylase (D β H) as shown in Figure 3. D β H is the enzyme of the catecholamine biosynthesis pathway that converts dopamine into norepinephrine in adrenergic and noradrenergic cells. Immune staining against these enzymes enables typification and quantification of neuronal subpopulations. For example, dopaminergic neurons contain TH but not D β H, whereas noradrenergic neurons contain TH and D β H. D β H was previously found to be expressed

in 95% of peripheral sympathetic neurons in different mammalian species^[4]. Jobling and co-workers found that TH was detectable in 88% of neurons in thoracic paravertebral ganglia of adult mice, while close to 100% of neurons in celiac ganglia were found to express this enzyme. Neuropeptide Y (NPY) is another neurotransmitter of peripheral sympathetic neurons. NPY can be, but does not have to be, co-expressed with TH. In murine thoracic ganglia, immunoreactivity to NPY was found to occur in 32% of TH-expressing neurons, whereas 4% of neurons with NPY immunoreactivity did not contain TH^[5].

4. Neuroeffector junctions

Norepinephrine released by postganglionic sympathetic neurons binds to α - and β -adrenergic receptors in the outer membranes of target cells. They belong to the class of G-protein coupled receptors (GPCR), a very diverse family of signaling proteins. Upon agonist binding to β receptors, a signaling cascade is launched involving the heterotrimeric G protein G_q , which activates phospholipase C, increasing inositol trisphosphate (IP_3) and diacyl glycerol levels (DAG). DAG initiates downstream protein phosphorylation while IP_3 stimulates calcium release from internal stores leading to coronary artery vasoconstriction and other cardiac effects^[6]. Stimulation of β receptors, specifically β_2 receptors that are functionally coupled to the cardiac L-type calcium channel Cav1.2, activates heterotrimeric G-protein G_s , which in-turn activates adenylyl cyclase, resulting in formation of cyclic adenosine monophosphate (cAMP). Increased cytosolic cAMP levels enhance phosphorylation of target proteins via protein kinase A (PKA)^[7], ^[8].

A well characterized effect of norepinephrine is an increase in cardiomyocyte contractility via PKA-dependent modulation of key Ca^{2+} transport proteins. NE-induced stimulation of β -adrenergic receptors leads to an increase in the phosphorylation of sarcolemmal L-type Ca^{2+} channels and ryanodine-sensitive Ca^{2+} release channels in the SR

membrane, which act synergistically to enhance systolic increases in cytosolic free Ca^{2+} , ultimately resulting in increased contractile force via Ca^{2+} -dependent activation of contractile proteins. From a functional point of view it is important that the inotropic response to an increase in sympathetic tone occurs in a spatially and temporally uniform pattern throughout the heart muscle. The anatomical underpinnings enabling such uniform responses of the heart to increases in sympathetic input have been largely unknown. Part of my thesis will therefore investigate the structural features of the cardiac sympathetic nervous system that enable a synchronous and spatially uniform transmission of nerve impulses to the myocardium during sympathetic activation.

B. The cardiac sympathetic nervous system

1. Physiological effects of sympathetic nerve stimulation in the heart

Sympathetic stimulation not only plays a vital role in maintaining homeostasis, but is also responsible for the well characterized “Fight-or-Flight” response. The cardiac stress response is multifaceted. Sympathetic stimulation increases chronotropy (the rate of pacemaker firing), dromotropy (electrical conduction in the specialized cardiac conduction system), inotropy (contractility), and lusitropy (myocardial relaxation)^[9].

2. Previous studies on the distribution of sympathetic nerves in adult mammalian heart

Cardiac sympathetic nerves extend from the postganglionic sympathetic neurons in the cervical and stellate ganglia. The nerve fibers project from the base of the heart into the myocardium, and run in bundles predominantly in the subepicardium of the ventricles. Individual fibers eventually egress the epicardial bundles to enter the underlying deeper portions of the myocardial walls (see Figure 4). The scheme of sympathetic nerve distribution shown in Figure 4 is consistent with a number of experimental observations. First, circumferential application of

phenol to the ventricular epicardium results in complete sympathetic denervation apical, but not basal, to the site of injury^[10]. Second, instillation of a tetrodotoxin-containing solution into the pericardial sac acutely interrupts sympathetic responses of the heart^[11]. Third, myocardial infarctions involving the epicardial layer lead to structural sympathetic denervation of viable myocardium distal to the site of ischemic injury^[12]. The latter experimental finding explains the vulnerability of the cardiac sympathetic network to ischemic insults.

Quantitative immunohistochemical studies have demonstrated regional differences in the density of sympathetic nerves in the heart. The central conduction system, including the sinoatrial node, atrioventricular node, and His bundle, is abundantly innervated compared to the working myocardium. On the other hand, there is a transmural gradient decreasing in innervation density from the epi- to endocardial layers of the left ventricle^[13]. Mühlfeld and co-workers explored a method to quantify total axon length in the murine left ventricle. Paraffin sections were randomly stained for a pan-neuronal marker (PGP 9.5). Estimations and calculations gave rise to a nerve length/heart volume fraction of 0.016% based on 75 m of total axon length in the left ventricle, including the septum^[14]. Although this investigation provided a non-biased method for determining axon length/region, it does so only for unspecified neurons in processed tissue. An assay to aid in unraveling the organizational principles specifically of the sympathetic network in the mammalian heart in living, intact tissue would be a crucial step in deciphering the impact of structural remodeling on disease states.

The postganglionic nerve fibers can be divided into two morphologically distinct regions. Axons proximal to their intracardiac arborization exhibit relatively uniform thickness, whereas intracardiac branches are characterized by periodic swellings ('varicosities') separated by short and thin (< 1 μm in diameter) nerve segments. Because proteins that are required for excitation-triggered neurotransmitter exocytosis (e.g.,

synapsin I) are abundantly expressed at these varicosities^[15], they very likely correspond to the neurotransmitter release sites. However, direct proof of this concept for the *in situ* myocardium is lacking. Action potentials propagating along individual axons can trigger release of norepinephrine (or other sympathetic transmitters) from multiple varicosities located along their path, enabling spatially synchronized responses of the target tissue to sympathetic stimuli. In contrast to e.g. motor neurons, which form neuroeffector junctions exclusively at nerve terminals, nerve-muscle junctions of postganglionic sympathetic nerves are distributed along their entire intramural segments. This patterning appears to facilitate rapid transmission of sympathetic signals to the target tissue and enables coordinated responses of different cell types to quickly adjust the myocardium to hemodynamic changes. For example, co-innervation of cardiomyocytes and adjacent small arteries by the same nerve would facilitate rapid adaptation of local blood flow (via sympathetically mediated arteriolar dilation) to increases in energy demand due to sympathetic stimulation-induced rise in cardiac muscle inotropy. Such nerve patterning would thus be vital for maintenance of a balanced energy demand/supply ratio in the heart. Alterations of sympathetic innervation density in the diseased heart (e.g., heart failure) would facilitate energy demand/supply mismatch (ischemia).

Despite being the main relay of excitatory sympathetic signals to the heart, little is known about the structural organization of the intracardiac sympathetic network. Both the form of axonal structures and their branching pattern importantly influence their function^[16-18]. For example, diameter of intramural segments determines the velocity of action potential propagation. Source-sink (impedance) mismatches at branching points can give rise to propagation failure. On the other hand, convergence of multiple thin nerve segments can facilitate conduction via summation of multiple sub-threshold electrical responses in thin nerve segments. Thus, a detailed delineation of the intracardiac sympathetic

network structure would aid in better understanding the anatomical underpinnings of functional compartmentalization within the sympathetic neurons innervating the normal and diseased heart.

Parameters that are of relevance to gain insight into the functional implications of nerve form and branching pattern are as follows: a) the total tissue volume that is innervated by a single postganglionic sympathetic neuron (i.e., the sympathetic nerve 'unit'); and b) the extent to which innervation units spatially overlap in the heart. For example, do intramural thin branches form physical connections with branches from other sympathetic neurons ('looping')? Do target cells receive input from multiple nerves (convergence)? c) The impact of regional variations in sympathetic nerve density on functional properties of target tissue. Numerous studies by others have demonstrated that sympathetic innervation is an important regulator of electrical and contractile phenotype during cardiac development, via transcriptional regulation and long-lasting post-translational modifications. It has been unknown, however, whether phenotypic switches similarly occur in the adult myocardium following alterations in sympathetic nerve density. An assay that enables simultaneous assessment of regional sympathetic nerve density and functional (i.e., electrical and/or calcium handling) properties in the living heart would shed light on the causal role of sympathetic innervation patterning in modulating the functional attributes of the heart muscle.

The goals of my thesis work were twofold. First, development and validation of an assay for imaging sympathetic nerves in the living mouse heart, and, second, use of this technique to obtain a three-dimensional wiring diagram of sympathetic nerves in a well-defined volume of the left ventricular epicardial layer from normal and chronically infarcted hearts.

These experiments constitute a first step of unraveling the organizational principles of the sympathetic network (the sympathetic

'connectome') in the mammalian heart and the impact of heart disease on structural alterations (remodeling) of these sympathetic circuits.

The assay for imaging the cardiac sympathetic net had to fulfill two major requirements:

- a. The ability to detect sympathetic nerves and to unambiguously discriminate them versus other cellular and non-cellular components in the living heart;
- and
- b. The ability to obtain optical sections with subcellular resolution from deep within living heart tissue for three-dimensional reconstruction of the sympathetic network.

To accomplish these experimental goals, I used a transgenic mouse model of sympathetic neuron-specific expression of a fluorescent reporter protein in conjunction with two-photon excitation fluorescence microscopy of the living, Langendorff-perfused mouse heart. Computer-assisted image processing algorithms were used for three-dimensional rendering of fluorescent nerves and generation of 3D wiring maps.

3. Long-term effects of sympathetic innervation on cardiac functional and structural properties

It is well established that sympathetic innervation patterning determines the electrical phenotype of the postnatal heart. In an embryonic state, the heart is minimally innervated, and yet functional. There is significant interest in determining the system's remodeling and the role played by neurotransmitters^[19]. For example, Lui et al. demonstrated decreases and increases in sympathetic nerve density in hearts from rats treated with an antibody against nerve growth factor (NGF) or NGF injections, respectively. Cardiomyocytes isolated from NGF-treated animals exhibited significantly shorter action potentials than those obtained from antibody-treated animals, owing to lasting posttranslational modifications of a repolarizing K^+ current^[20]. The Fukuda laboratory found that cardiomyocyte-restricted overexpression of Sema3a

(a neuro-repellent cytokine) in transgenic mice caused a reduction in overall sympathetic innervation density and inversion of the physiological transmural innervation gradient, leading to spatially heterogeneous action potential prolongation, increased susceptibility to tachyarrhythmias, and sudden death. Contrastingly, Sema3a-deficient mice exhibited sympathetic hyperinnervation which was associated with sinus bradycardia^[21]. These observations suggest that sympathetic innervation plays role in determining the electrical phenotype of the developing as well as the adult mammalian heart.

Other sympathetic neurotransmitters also play a role in regulation of myocardial function. Protas and colleagues demonstrated that the density of $I_{Ca,L}$ increases via an NPY-dependent pathway involving sustained posttranslational modification of the calcium channel protein(s) in adult mice^[22]. Furthermore, exposure of cultured cardiomyocytes to NPY mimicked the sympathetic nerve effect on $I_{Ca,L}$, suggesting that neurally released NPY regulates the L-type Ca^{2+} channel properties. On the contrary, treatment of cultured myocytes with NE recapitulates the effect of sympathetic neuron co-culture on the fast Na^+ current, I_{Na} ^[23], indicating involvement of different signaling pathways for different channels.

4. Sympathetic remodeling in the adult diseased heart

a. Myocardial infarction

Prior myocardial infarct has long been implicated as a risk factor for cardiac arrhythmias and arrhythmogenic sudden death. Miyauchi et al. found that chronic myocardial infarction in canines without atrial involvement causes biatrial heterogeneous sympathetic nerve sprouting and increased susceptibility to atrial fibrillation^[24]. This study demonstrated that an infarct of the left ventricle could cause sympathetic hyperinnervation in myocardial regions remote from the infarct scar,

promoting fibrillatory activity. The mechanisms underlying atrial hyperinnervation post-myocardial infarction are yet unknown.

Sympathetic hyperinnervation at the infarct border zone is very well documented. Changes in sympathetic density have long been implicated in post-infarction arrhythmogenesis. The Chen laboratory previously found that levels of cardiac-derived NGF and growth associated protein-43 (GAP-43) increased at the peri-infarct sites following permanent occlusion of the left anterior descending coronary artery in dogs^[25]. Those same dogs had significantly higher overall TH-positive axon density in comparison to sham operated dogs and increased propensity to spontaneous ventricular tachyarrhythmias. Chen's group also previously reported sympathetic hyperinnervation at the scar-muscle junction in human patients with a history of ventricular tachyarrhythmias post-myocardial infarction^[26].

b. Cardiac hypertrophy

Innervation function and density of a region is effected by target organ-derived neurotrophic factors^[27]. Results from the Fukuda laboratory indeed suggest that cardiac sympathetic axon growth is regulated via cardiomyocyte-derived NGF^[28]. Cardiomyocyte-restricted transgenic overexpression of NGF has been shown to induce cardiac hypertrophy, which was associated with arrhythmogenic electrophysiological alteration^[29]. Wistar rats when exposed to monocrotaline develop symptoms signifying human pulmonary hypertension^[30]. Fukuda's laboratory used this right ventricular pressure overload model to show localized increases in TH-expressing nerves. Interestingly, even though sympathetic hyperinnervation occurred, it was accompanied by a downregulation of neuronal function. Further investigations into the phenomenon concluded that the hypertrophic response of the cardiomyocytes led to rejuvenation of regional cardiac sympathetic nerves^[31].

c. Role of altered sympathetic innervation in cardiac arrhythmogenesis

Changes in regional density and/or distribution of sympathetic nerves in the heart have been causally implicated in the genesis of life-threatening ventricular tachyarrhythmias leading to sudden cardiac death^[32]. Indeed, regional sympathetic denervation leading to arrhythmogenic sensitivity apical to a myocardial infarction has been confirmed in mongrel dogs^[10]. Stanton and co-workers confirmed findings that the human myocardium follows similar neurological remodeling post-myocardial infarction^[33]. It has also been shown that local defects in sympathetic neurotransmitter release generate increased heterogeneity of the myocardial response to anti-arrhythmic drugs^[34]. The discordant pharmacodynamics feasibly pose an increased risk of sudden death due to arrhythmia.

Despite a large body of clinical and experimental evidence supporting a role of sympathetic remodeling in cardiac arrhythmogenesis, a causal link has not been established. In other words, there is no study directly demonstrating induction of arrhythmias by changes in innervation pattern (density and/or distribution) alone in the absence of confounding structural and/or functional abnormalities typically occurring in the diseased heart. Further, it has been unknown how sympathetic remodeling alone alters the functional and structural properties of the heart. Although *in vitro* studies demonstrate profound effects of sympathetic innervation on ion handling properties of the myocardium via translational and/or lasting posttranslational mechanisms, there is no study investigating the effect of altered sympathetic innervation on the electrical or calcium handling properties of the target myocardium in the intact heart. There is a known increase in sympathetic activity in a variety of cardiac disease states. Hyperactivity has been associated with hypertension, obesity, ischemic heart failure, unstable angina and acute myocardial infarction among others^[35]. Areas of hyperinnervation are thought to play a significant role in electrical remodeling of the ventricular

myocardium leading to various arrhythmia and sudden cardiac death^[36]. Even though there is mounting evidence linking insult to hyperinnervated states and the subsequent complications thereof, little is understood about the direct sympathetic/myocyte interactions. Up until now there has been no means to specifically observe cardiac sympathetic innervations in its native tissue under physiological conditions.

C. Current gaps of knowledge on cardiac sympathetic innervation

Little is known of the cardiac sympathetic “connectome”. Other than the most basic of interactions and responses to certain disease states, in-depth research on the structure/function relationship has been lacking. For example, it is currently unknown how many myocytes are innervated by a single neural input. The range of target tissue volume innervated by a single postganglionic neuron is also undetermined. Do multiple neurons innervate the same region of the heart? Conversely, does a single neuron innervate multiple areas of the heart? Are certain areas innervated in a redundant pattern to protect against disease-induced rarefication of sympathetic nerves, or would injury leading to redundant innervation be pro-arrhythmogenic?

There are certainly a number of intriguing sympathetic structural anomalies currently unexplained or even researched. It is unknown if single nerves innervate multiple cardiac cell types, i.e., does a nerve innervating an artery also innervate the immediately surrounding cardiomyocytes allowing for a matched signal response? There is also a looping phenomenon seen in the neurites, the functional implications of which have not been examined previously. Also, the structure of the axon trajectories has not been studied, although the organization of the axonal arbor has profound effects on the signal transmission and processing. Accordingly, this study focuses on development of an imaging-based system which will begin to allow the unraveling of such quandaries.

D. Two-photon excitation fluorescence microscopy

1. Principle of two-photon excitation fluorescence microscopy

Standard epifluorescent microscopy is excellent for obtaining fluorescence from thin sections of tissue or monolayers of cells. However, the image attained contains out-of-focus light. To overcome this problem, confocal microscopy was developed (Figure 5). It uses spatial filtering to eliminate out-of-focus light, and therefore can be used in specimens thicker than the plane of focus. The advantages to this are many, including: the ability to reduce or eliminate background interference from the focal plane, the capability to collect optical sections from thick specimens, and the use of specific wavelength tuned lasers for illumination of the desired fluorophores. This provides for extremely high-quality images from specimens which can be prepared similarly to conventional fluorescence microscopy or even in living systems^[37]. Instead of illuminating the whole specimen, as in epifluorescent microscopy, the confocal optical system focuses a spot of light onto a single point at a desired depth in the specimen. To achieve the bright pinpoint of illumination required, a specific wavelength laser is passed through a pinhole. The emitted fluorescence from the specimen is subsequently collected and amplified by a light detector such as a photomultiplier tube (PMT). A pinhole aperture is placed in front of the detector, at a position that is confocal with the illuminating pinhole; where the rays emitted from the illuminated point in the specimen come to a focus. Only the rays of light that are in focus will then pass through the aperture and enter the PMT^[38].

Confocal Microscopy also carries limitations. Due to the pinhole exclusion of scattered fluorescence light originating in the focal plane, a portion of the signal is lost, lowering the intensity of the fluorescence signal and reducing the depth at which signals can be obtained from within light-scattering biological specimens. Illumination of the entire depth of tissue (see left panel in Figure 6) can cause fluorophore bleaching and

phototoxicity, leading to reduction in signal quality and uncontrollable side effects. Alleviation of these issues comes through two-photon fluorescence microscopy.

Two-photon excitation (TPE) microscopy is based on the idea that two photons of lower energy can be synergistically used to excite a fluorophore if each photon carries approximately half the energy necessary to excite the molecule. The subsequent fluorescent emission has a resultant energy higher than the incident photons. The incident photon absorption must be essentially simultaneous for effective fluorophore excitation. This would have too low a rate of occurrence to be exploitable for fluorescence microscopy. In order to augment the incidence of two-photon excitation events, high-frequency (60 MHz) femto-second pulses of long wavelength laser light (typically twice the wavelength of the single-photon excitation peak) are delivered to the specimen, increasing the likelihood of multiphoton absorptions. Where such absorptions occur is effectively restricted to a minuscule ellipsoid volume around the focal point of the objective (Figure 7)^[39]. The axial and lateral dimensions of TPE volume are determined by the excitation wavelength and the numerical aperture of the objective lens. A 4-fold reduction in the numerical aperture of the objective lens will increase the spread of the excitation volume ≈ 22 -fold axially and ≈ 4 -fold laterally, amounting to an increase in TPE volume by more than two orders of magnitude, whereas increasing excitation wavelength from 700 to 1000 nm will increase TPE volume by only ≈ 3 -fold. Thus, using TPE microscopy with a uniformly illuminated, high numerical aperture objective, fluorescence excitation is confined to less than femtoliter volumes around the focal point of the objective, with $< 1 \mu\text{m}$ resolution in the z direction. The confinement of the TPE within the specimen gives two-photon fluorescence imaging its intrinsic three-dimensional resolution.

Several factors improve penetration depth when compared to single-photon confocal microscopy, without a significant loss of spatial

resolution. First, the dependence of fluorophore excitation on the second power of laser light intensity confines photon absorption to a narrow region at the plane of focus, where photon flux is highest. Thus, unlike single-photon confocal microscopy, TPE microscopy lacks linear absorption of the excitation beam by fluorophores above the plane of focus, which can significantly reduce excitation light before it reaches fluorophores within deeper tissue regions. Second, the longer wavelengths used for TPE are scattered by the tissue much less than the shorter wavelengths used for confocal microscopy, resulting in deeper penetration of the focused laser beam. Third, scattered light emitted from an excited fluorophore within the focal volume does not contribute to the final image in confocal microscopy because it is indistinguishable from fluorescent light generated in out-of-focus areas and is rejected by the pinhole in the emission path. By contrast, because TPE never generates out-of-focus fluorescence, scattered photons from fluorophore emission can be used to generate the TPE image; resulting in increased fluorescence collection efficiency and thus greater signal intensity at any given tissue depth. The fluorescent emission is collected by large external detectors without interposition of a pinhole in the emission path of the microscope, increasing the fluorescence light that contributes to the final image.

Collectively, the properties of 2-p fluorescence microscopy, including improved penetration depth in light-scattering biological specimens without loss of spatial resolution compared to confocal 1-p microscopy and its intrinsic three-dimensional resolution, make this technique ideally suited to map the cardiac sympathetic network.

2. Biological applications of TPE fluorescence microscopy

Given the physical properties of TPE fluorescence microscopy, its use for *in vivo* imaging of structure and function with subcellular resolution in a variety of tissues does not come as a surprise. Multiphoton imaging techniques are seemingly limitless. For example, two-photon fluorescence

lifetime imaging has been used to discover varying pH microdomains in stratum corneum - the uppermost epidermal layer^[40]. CARS imaging, short for coherent anti-Stokes Raman scattering, has been used to witness in real-time the actual progress of demyelination in the central nervous system^[41]. Stimulated emission depletion (STED) microscopy, a technique which uses dually focused laser beams to excite a fluorophore in a specified area and deplete non-fluorescent decay to a grounded state, has been beautifully documented in the literature exposing nanoscale imaging of neuronal structures beyond TPLSM diffraction limits^[42].

Traditional TPE microscopy is just as valued a research tool. The depth penetration of TPE in strongly scattering tissue is superior to simple confocal microscopy. TPE microscopy has been proven effective in determining calcium dynamics between individual myocytes of intact perfused hearts^[39], neuronal activity mapping^[43], and determination of oxidative stress using intrinsic fluorescence in various disease states^[44].

3. Cell lineage-restricted expression of green fluorescent protein and its variants for in vivo labeling

Imaging has become an irreplaceable tool for studying an array of neural disease or injury models. Fluorescence can be used for the delineation of transplanted cells, to track neural development, and exploration of events leading to and surrounding neural plasticity. Restriction of fluorescent reporter protein expression, e.g. green fluorescent protein (GFP), to neuronal subpopulations allows specific subsets of neurons to be observed and studied by virtue of their reporter expression while in living contact with native surroundings^[45]. Abematsu et al. used GFP expressing neural stem cells (NSC) transplanted into a spinal cord injury (SCI) mouse model. Here, the group was able to not only monitor transplanted cells synapsing with host tissue during hind limb recovery of the injured mice post NSC transplantation into the SCI epicenter, but also confirm loss of recovered motion via ablation of transplanted neural tissue^[46]. The use of GFP allowed for the true

distinction of transplanted NSC-derived tissue from native host tissue. Without fluorophore labeling of the NSCs, *in vivo* cataloging neurons from a specific origin would have been impossible.

Understanding neural development and migration is crucial basic research. Vallee and co-workers introduced GFP into neural progenitor cells in the mouse neocortex by *in utero* electroporation. The lab was able to study neuronal migration in the developing neocortex in wild-type and functionally impaired “Legs at Odd Angles” mice by imaging the GFP expression in developing neurons^[47]. Impaired mice showed a reduction in the neural migration to the neocortex. The use of fluorescence expressing neural progenitors allowed for the monitoring of neural development and migration, leading to the discovery of neural deficits in specific areas of the brain being associated with this particular phenotype.

The use of GFP in conjunction with TPE microscopy has been used to explore neural plasticity as an experience-dependent response in the adult mouse neocortex. Remodeling of axonal and dendritic spine subsets were found through synapse appearance or elimination on a daily basis. Most newly formed spines were not persistent. However, when every-other whisker was trimmed, newly formed spines were unrelenting, suggesting that sensory experiences stabilize new spinal protrusions and promote synaptic formation^[48]. Fluorescently labeled neurons could be imaged over a period of time, allowing for spine formation and dissolution to be quantified under various circumstances.

Transgene expression of fluorescent reporter proteins is not limited to single color applications. The Lichtman laboratory has developed an elegant system of targeting fluorophore combinations to subpopulations of neurons using unique Cre/lox recombinations. This allows for varying levels of three spectral variants of GFP to be expressed, creating up to 90 colors, allowing the reconstruction and determination of intertwined neighboring neurites^[49].

E. Hypotheses

Specific Aim 1. Create, characterize and validate a transgenic fluorescent reporter mouse model for tracking cardiac sympathetic nerves.

We generated transgenic mouse lines in which expression of enhanced green fluorescent protein (EGFP) is under the control of the human dopamine- β -hydroxylase (hD β H) gene promoter, to direct transgene expression to peripheral sympathetic neurons. We initially performed immunohistochemical analyses of paravertebral sympathetic ganglia to confirm restriction of EGFP expression to the target cell type and to screen for the line with the highest penetrance of transgene expression. Quantitative co-localization analyses on cardiac sections obtained from a high-penetrance/high-specificity line were then employed to validate the utility of the transgenic approach to track the micro-anatomy of cardiac sympathetic nerves in the adult heart. The morphology of hD β H-EGFP paravertebral ganglia and heart as well as transmembrane action potentials of isolated hD β H-EGFP postganglionic sympathetic neurons was compared with those of wild-type littermates to assess the potential toxicity of transgene expression.

Specific Aim 2. Obtain three-dimensional reconstructions of the sympathetic network in the left ventricular subepicardium of the adult hD β H-EGFP heart.

Once the utility of the hD β H-EGFP mouse model for tracking cardiac sympathetic nerves had been validated, we used two-photon laser scanning microscopy (TPLSM) to determine the spatial distribution of EGFP fluorescence in subepicardial layers of adult transgenic hearts. Frame-mode images were acquired at increasing depth (z-stacks) from within contiguous tissue volumes encompassing the subepicardium of electromechanically dissociated, Langendorff-perfused mouse hearts. Following image processing which included spatial filtering, thresholding, and removal of tissue autofluorescence, individual image stacks were stitched and rendered in 3D for subsequent quantitative measurements.

Specific Aim 3. Measure sympathetic nerve length as well as branching and looping pattern of the subepicardial sympathetic network in normal and infarcted hD β H-EGFP hearts.

TPLSM image stacks were obtained from normal and infarcted hD β H-EGFP hearts. Volume rendered image stacks were skeletonized in 3D using an interactive tracking algorithm implemented in Amira. The effect of interobserver variability on the appearance of the skeletonized arbor was assessed. Cumulative nerve length per imaged tissue volume as well as branching and looping patterns were determined and compared between normal and injured hearts.

II. Materials and Methods

A. Generation and identification of transgenic mice expressing enhanced green fluorescent protein in peripheral sympathetic neurons

A transgenic mouse model was generated to quantitate cardiac sympathetic innervation density in living heart. The mouse model utilized the 5.9 kb human dopamine- β -hydroxylase (hDBH) gene promoter sequence (provided by Dr. Palmiter, Washington University, Seattle, Washington) fused to the EGFP-encoding cDNA sequence. A 530-base pair fragment of the murine protamine-1 gene (mPrm1) including the poly(A) adenylation site and signal was inserted downstream of the EGFP sequence^[50]. The hDBH-EGFP fusion gene was linearized and microinjected into the male pronucleus of fertilized C3HeB/FeJ embryos using standard techniques^[51]. The microinjected embryos were cultured to the two-cell stage, implanted into the oviducts of pseudopregnant females and allowed to develop to term. The resulting pups were screened for the presence of the transgene by a modified polymerase chain reaction (PCR) protocol. For PCR analysis, biopsied tissue (approximately 10 mg) was digested overnight at 55° C with proteinase K (0.05 mg/ml in 1 x PCR buffer: 50 mM KCl, 10 mM Tris-HCl, pH 8.3, 2.5 mM MgCl₂, 0.1 mg/ml gelatin; 50 ml). The next morning, the proteinase K was heat-inactivated at 85° C for 15 minutes, and 1 μ l of the digest was added directly to 49 μ l of 1 x PCR buffer containing 1.25 μ M of each oligonucleotide primer, 0.25 mM of each deoxynucleotide, 1 unit *Taq* polymerase (Perkin-Elmer Cetus; Norwalk, CT). Amplification was performed over 35 cycles with 1 minute of denaturation at 95° C, 2 minutes of annealing at 63° C, and 3 minutes of extension at 72° C. After PCR amplification, the samples were displayed on agarose gels containing ethidium bromide and visualized directly by ultraviolet fluorescence. Only samples derived from animals carrying the hDBH-EGFP transgene gave rise to diagnostic PCR amplification products. The transgene-specific oligonucleotide primers were (5' ATCGAGCTGAAGGGCATCGACTTCAAGGAG3') and

(5'CTCCAGCAGGACCATGTGATCGCGCTTCTC 3'). A segment of an endogenous single copy mouse gene provided an internal control for the reaction.

Six transgenic lineages were generated. Initial screening for EGFP expression in superior cervical and stellate ganglia revealed mosaic transgene expression, with anywhere from 10% to 80% of the sympathetic neurons exhibiting EGFP fluorescence of varying strength in the adult ganglia. After crossing the mosaic expressing mice into a DBA/2J background, 95% of the sympathetic neurons in mouse line 4 expressed EGFP (based on the analyses of 8 ganglia distributed among 4 adult mice). A similar genetic background effect has been observed in a number of other α -myosin-heavy-chain-promoted transgenes^[52]. Consequently, line 4 was used for experiments. Only results from mice which had been backcrossed into the DBA/2J background for > 5 generations were used for analyses.

B. Immunolabeling

Mice of either sex and genotype between 12 and 38 weeks of age received intraperitoneal injections of heparin (125 I.U./kg bodyweight) and were sacrificed via cervical dislocation in accordance with animal usage protocols. The heart was quickly excised, the ascending aorta was cannulated with an 18-gauge cannula, and the heart was perfused retrogradely at constant pressure with oxygenated Tyrode's solution, containing (in mmol/L) 140 NaCl, 5 KCl, 1 MgCl₂, 2 CaCl₂, 10 HEPES and 10 glucose, pH of 7.4 (adjusted with 1 M NaOH). Once the coronary effluent became clear of blood, the perfusate was switched to a fixation solution containing (in mmol/L) 78 cacodylic acid, 333 paraformaldehyde, and 114 NaCl; pH 7.4. After 10 minutes of continuous perfusion, the heart was submerged in fixation solution at ~ 5 °C overnight. Cervical and stellate ganglia were removed bilaterally and submersion fixed overnight. Post fixation, the tissues were cryoprotected via overnight incubation in an

ice-cold 30%-sucrose-PBS solution, embedded in O.C.T. (Sakura Finetek; Torrance, CA) tissue freezing medium, stored at -80° C for 1 hour, sectioned at 10 µm thickness, and mounted on frosted slides.

The following primary antibodies were used: a rabbit polyclonal antibody directed against tyrosine hydroxylase (AB 152; Millipore; Billerica, MA); a chicken polyclonal antibody directed against tyrosine hydroxylase (AB76442; Abcam; Cambridge, MA); a rabbit polyclonal antibody directed against GFP (AB3080; Millipore; Billerica, MA); a rabbit polyclonal antibody directed against connexin43 (AB1728; Millipore; Billerica, MA); a FITC-preconjugated, goat polyclonal antibody directed against GFP (NB100-177; 1Novus Biologicals; Littleton, CO). All antibodies had been affinity purified. Secondary antibodies were either goat polyclonal anti-rabbit IgG or goat polyclonal anti-chicken IgY conjugated to one of the fluorophores, Alexa546, Alexa555, Alexa633 (Invitrogen; Grand Island, NY), or DyLight405 (Thermoscientific; Pittsburgh, PA). These antibodies had been affinity-purified and had been highly adsorbed to minimize species cross-reactivity.

Sections were incubated with 0.2% Triton X-100 (Sigma-Aldrich; St. Louis, MO) in PBS for 1 hour, followed by 30 minutes of blocking with 2% BSA. Sections were then incubated for 12 hours with primary antibodies in PBS supplemented with 2% BSA and 10% normal goat serum, and subsequently reacted with appropriate secondary antibodies for 1.5 hours, followed by a 5 minute incubation in PBS containing Hoechst (1:1000). All incubation steps were performed at room temperature, and between all incubation steps the slides were thoroughly washed with PBS three times for 5 minutes each. Sections were mounted in Vectashield (H-1000; Vectorlabs; Burlingame, CA) or ProLong Gold solution (A21103; Life Technologies, Inc; Grand Island, NY). Coverslips were fixed to the slides with nail polish if Vectashield was used as the mounting medium. Sections that had been incubated with secondary antibody without having been labeled with primary antibody served as control.

To determine the empirical upper limit of co-localization, sections from an adult non-transgenic heart were first incubated with a rabbit polyclonal antibody against TH, followed by dual labeling with Alexa546- and Alexa633-conjugated goat polyclonal anti-rabbit IgG. To determine the lower limit of co-localization, sections were dually stained with a rabbit polyclonal antibody directed against connexin43 (Cx43) and a chicken polyclonal antibody directed against tyrosine hydroxylase, followed by incubation with Alexa546- and Alexa633-conjugated goat polyclonal antibodies directed against rabbit IgG and chicken IgY, respectively. The control experiments skipped incubation with the primary antibodies.

C. EGFP expression in sympathetic ganglia

Ten-micron thick midsections from cervical and stellate ganglia of transgenic and control animals between 12 and 38 weeks of age were assayed for dual EGFP and tyrosine hydroxylase expression by examining the distributions of anti-GFP and anti-TH immunoreactivities. Tissue sections were double stained with a FITC-preconjugated rabbit polyclonal antibody directed against GFP and a rabbit polyclonal antibody directed against tyrosine hydroxylase as outlined above. A polyclonal goat anti-rabbit IgG conjugated to Alexa555 was used to visualize anti-TH immunoreactivity. Stained sections were imaged using a Leica fluorescence microscope equipped with a 20x 0.5 NA objective and the following filter cubes (excitation/emission): 340-380/425 LP (Hoechst), 450-490/515 LP (FITC or EGFP) and 515-560/590 LP (Alexa555). We acquired 440 x 340 μm^2 non-overlapping images from each of the 3 sections per ganglion per animal. Exposure times for each excitation wavelength were the same for sections with and without primary antibody incubation. FITC and Alexa555 fluorescence images from hD β H-EGFP ganglia were thresholded against images obtained from wild-type ganglia stained with anti-GFP antibodies and from transgenic ganglia incubated only with the anti-rabbit IgG secondary antibody, respectively. Transgenic

sympathetic neurons were identified by virtue of co-localization of cytoplasmic anti-TH and anti-GFP immunofluorescence. Penetrance of transgene expression was defined as the percentage of tyrosine hydroxylase-positive, i.e., sympathetic, neurons expressing EGFP. Metamorph software (Molecular Devices; Sunnyvale, CA) was used for image processing.

D. Measurement of cardiac sympathetic nerve density

Ten-micron-thick sections from the heart of adult transgenic and non-transgenic animals between 12 and 38 weeks of age were dually immunostained with a rabbit polyclonal antibody against TH and a mouse monoclonal antibody against sarcomeric α -actinin, followed by incubation with FITC- and rhodamine-conjugated secondary antibodies, and subjected to epifluorescence microscopy. Five images were acquired each from the left and right atrium, and left and right ventricular free wall, using a 20x 0.5 NA objective. FITC and rhodamine fluorescence images were thresholded against images obtained from adjacent sections that had been incubated with the secondary antibodies only, and binarized. Sympathetic nerve density was measured as the number of pixels containing tyrosine hydroxylase divided by the number of pixels containing sarcomeric α -actinin. Metamorph version 7.1.0.0 was used for image processing.

E. EGFP expression in intracardiac sympathetic nerves - quantitative co-localization analyses

1. Immunolabeling and confocal imaging parameters

Four-chamber longitudinal sections were obtained from hearts of transgenic and control mice between 12 and 38 weeks of age and dually stained with a rabbit polyclonal antibody directed against GFP and a chicken polyclonal antibody directed against TH as outlined above. Alexa555- and Alexa633-conjugated goat polyclonal antibodies directed against rabbit IgG and chicken IgY, respectively, were used to visualize

tissue distribution of anti-GFP and anti-TH immunoreactivities. Tissue samples were imaged using a confocal laser scanning microscope (FV1000; Olympus; Center Valley, PA). We used a 63 x 1.42 NA oil-immersion (RI = 1.515) objective and optically zoomed-in by a factor of 4. Alexa555 fluorescence was excited with a 559 nm laser and detected through a band-pass emission filter of 570-625 nm. Alexa633 fluorescence was excited with a 635 nm laser and collected through a band-pass filter of 655-755 nm. Images were acquired at the Nyquist frequency (i.e., twice the maximal spatial frequency) in the x-y direction (pixel size = 0.106 μm) and oversampled by a factor of ~ 3 in the z direction (z-step size = 0.3 μm), with a 12-bit range. In our imaging system, the maximal spatial frequency is determined by the resolution of the microscope, and for the particular imaging conditions that we used the resolution is ~ 200 nm in x-y plane, and ~ 850 nm along the z axis^[53]. We thus used the zoom-in feature of the microscope to obtain a pixel size that corresponded to the Nyquist frequency. Images for each detection channel were acquired sequentially using a pixel dwell time of 4 μs and a Kalman integration of 4. Laser power, pixel time, and detector sensitivity were adjusted for both channels individually to obtain relatively balanced signal intensity distributions for each channel.

2. Specificity of primary antibodies and signal bleed through

Pilot experiments were performed to verify specificity of primary antibodies as well as to exclude fluorescence bleed through from one channel to the other under the imaging conditions employed. To examine the specificity of the primary antibodies used, we took advantage of our previously generated transgenic reporter mouse which exhibits mosaic EGFP expression in the heart^[52]. Accordingly, a 10- μm section from a mosaic transgenic heart was immunostained with the same rabbit polyclonal anti-GFP and chicken polyclonal anti-TH antibodies as above, followed by Dylight405-conjugated goat anti-rabbit IgG and Alexa555-

conjugated goat anti-chicken IgY, and subjected to epifluorescence imaging. Figure 9 demonstrates that areas exhibiting anti-GFP (blue) or anti-TH (red) immunofluorescence were mutually exclusive, indicating that the combination and concentrations of primary antibodies used for co-localization analyses enabled specific antigen recognition in the tissue of interest.

Next, we examined the possibility of fluorescence signal bleed through between the red and far-red channel under the imaging conditions employed. Bleed through was estimated creating controls with fluorescence labeling in one channel and none in the other and then recording the signal coming from the unlabeled wavelength. Accordingly, a section from an adult hD β H-EGFP heart was immunostained with an anti-GFP antibody, followed by incubation with an Alexa546-labeled secondary antibody, and subjected to laser confocal microscopy. Fluorescence signals were sequentially collected in the 570-625 nm and 655-755 nm range during excitation with 559 nm or 635 nm laser light, respectively. Figure 10A and B demonstrate that the Alexa546 signal that was recorded in the 570-625 nm channel during 559 nm illumination (left panels in Figure 10) followed the contours of an intracardiac nerve, whereas the image collected in the far-red channel during 635 nm excitation did not exhibit a discernible pattern, and its intensity was less than the chosen threshold (right panel in Figure 10). Another section from an adult hD β H-EGFP heart was reacted with an anti-TH antibody, followed by an Alexa633-conjugated secondary antibody, and the same imaging sequence as described for the anti-GFP/Alexa546 antibody combination was obtained. The results are shown in Figure 10C. Anti-TH immunoreactivity was readily detectable along an intracardiac sympathetic nerve in the 655-755 nm channel during 633 nm illumination, whereas no distinct fluorescence pattern was visible in the 570-625 nm emission range during 559 nm illumination. Overall, these results indicate the absence of a significant signal bleed through between Alexa555 and Alexa633 under

the imaging conditions employed, and further support the utility of this fluorophore combination for measuring co-localization.

3. Image pre-processing

A flow chart of the image processing steps is shown in Figure 11. Confocal image stacks were deconvolved using Huygen's Professional software 32bit version 4.1.1p2. Point spread functions used for deconvolution were calculated based on lens specifications and pinhole diameters of 1 airy unit. Post-deconvolution, image stacks were thresholded in each channel to remove background noise. Threshold levels were determined by first generating intensity histograms of areas that contained no fluorescence signal. The lower threshold was then set to the intensity value corresponding to the 75th percentile of the intensity distribution. To eliminate single pixel noise, a median filter with a 3 x 3 kernel was applied. The deconvoluted, background-corrected and filtered image stacks were then segmented into their three orthogonal stacks and maximum projections in the XY dimensions were obtained using Metamorph software (Molecular Devices; Sunnyvale, CA). Maximum projections were used for co-localization analyses. Pearson's, coefficients were derived from these projections using the *ImageJ* plugin "Colocalisation Threshold".

4. Calculation of Pearson's coefficient

Pearson's coefficient was calculated according to the following equation:

$$R = \frac{\sum (S1_i - S1_{avg}) \times (S2_i - S2_{avg})}{\sqrt{\sum_i (S1_i - S1_{avg})^2 \times \sum_i (S2_i - S2_{avg})^2}}$$

wherein $S1_i$ is the intensity of the i th pixel in channel 1; $S1_{avg}$ is the average intensity of all pixels in channel 1; $S2_i$ is the intensity of the i th

pixel in channel 2; and $S2_{avg}$ is the average intensity of all pixels in channel 2.

The Pearson's coefficient, R , measures the correlation between the intensity distributions in two channels in terms of a least-square fit. Its value can be between - 1 and 1. A value of 1 indicates complete correlation between the two channels and a value of - 1 indicates complete exclusion. R is effectively the ratio between the covariance of the channels and the product of their standard deviations; therefore its value is dependent on a balance between the intensities of corresponding channels. Consequently, a pixel-pair of similar intensities would be considered "more" co-localized than a pixel pair of widely differing intensities.

5. Calculation of Mander's 1 and Mander's 2 coefficients

The colocalization coefficients M1 and M2 are calculated according to the following equations:

$$M1 = \frac{\sum_i S1_{i,coloc}}{\sum_i S1_i}$$

where $S_{1i,coloc} = S1$ if $S2_i > 0$ and $S_{1i,coloc} = 0$ if $S2_i = 0$;

$$M2 = \frac{\sum_i S2_{i,coloc}}{\sum_i S2_i}$$

where $S_{2i,coloc} = S2$ if $S1_i > 0$ and $S_{2i,coloc} = 0$ if $S1_i = 0$.

$M1$ is the sum of the intensities in channel 1 which have a signal of any intensity in channel 2 divided by the total sum of pixels, above threshold, with intensity in channel 1. $M2$ is the sum of the intensities in channel 2 which have a signal of any intensity in channel 1 divided by the total sum of pixels, above threshold, with intensity in channel 2. Absolute intensities of each channel are not taken into consideration. For instance, a bright signal in channel 1 colocalizing with a faint signal in channel 2 is considered equivalent to a bright signal in channel 1 colocalizing with a bright signal in channel 2. Because all non-zero signals are correlated, meticulous background correction is required to calculate the amount of signal overlap of each channel on the other. The *Image J* plug-in 'Colocalization Threshold' estimates thresholds for both channels simultaneously over a range of decreasing thresholds until the probability of correlation equals zero^[54].

F. Transmembrane action potential recording in isolated postganglionic sympathetic neurons

Stellate and cervical ganglia were excised from hD β H-EGFP transgenic mice and wild-type litter mates. Single neurons were obtained by enzymatic digestion and cultured for 12 - 24 hours before use. Transmembrane action potentials were recorded in current-clamp mode of the whole-cell patch-clamp technique. Experiments were carried out at room temperature. The bath solution contained (in mmol/l) 140 NaCl, 5 KCl, 1 MgCl₂, 2 CaCl₂, 10 HEPES, 10 D-glucose, pH 7.4 (adjusted with 1 N NaOH). Patch electrodes were prepared from borosilicate glass (Sutter Instruments, Inc.; Novato, CA) by a two-stage pull on a horizontal puller (Sutter Instruments; Novato, CA). The electrodes were filled with a filtered solution containing (in mmol/l) L-aspartic acid, 2 MgCl₂, 5 HEPES, 5 Na₂ATP, 1.1 EGTA, 0.1 CaCl₂, pH 7.2 (adjusted with 1 N KOH). Action potentials were induced by square wave currents of 1-ms duration. Signals were recorded with an Axon Multiclamp 700B amplifier (Molecular Devices; Sunnyvale, CA), filtered at 10 kHz, digitized at 50 kHz, and

stored on the computer's hard disk with 16-bit resolution. Recordings were analyzed using the Clampfit suite of the pClamp10 software (Molecular Devices; Sunnyvale, CA).

G. Two-photon laser scanning microscopy (TPLSM) of Langendorff-perfused mouse heart

1. Description of the two-photon excitation imaging system

The imaging system is schematically illustrated in Figure 12. It consists of an Olympus FV1000 confocal scanning microscope (Olympus; Center Valley, PA) modified for two-photon excitation. Illumination for two-photon excitation is provided by a mode-locked Titanium:Sapphire laser (Spectra-physics; Santa Clara, CA), which generates trains of 100 fs pulses at a repetition rate of 80 MHz. Excitation wavelengths between 700 and 1000 nm can be selected. Hearts were imaged through a 60X 1.2 NA water-immersion objective with a working distance of 280 μm . Emitted light is split by two dichroic mirrors (DM485 and DM570) in series, passed through narrow-band pass filters (420-460 nm [blue], 495-540 nm [green], and 575-630 nm [red]) and collected with three independent external photomultipliers. Thus, emission from the fluorophore is not descanned using a pinhole as in single-photon laser scanning microscopy. The intensity of each pixel is digitized at 12-bit and stored on the computer's hard disk for off-line analyses. Pixel sizes, as set by the objective and hardware zoom-in factor of the laser scanning unit, ranged from 0.104 μm and 0.207 μm in the in the xy dimension. Pixel dwell time was set to 8 μs . Thus, acquisition time for a single 512 x 512 pixel frame image was ~ 2.1 s.

2. Heart preparation for TPLSM imaging

Five minutes after intraperitoneal injection of heparin (125 I.U./kg bodyweight), the mouse was sacrificed by dislocation of the neck, the heart rapidly removed, connected to a Langendorff apparatus, and the coronary arteries were continuously perfused at 60 cm H₂O via a

customized, 18G cannula in the aortic root with oxygenated, HEPES-buffered Tyrode's solution (room temperature). The solution consisted of the following (in mmol/L): 140 NaCl, 5 KCl, 1 MgCl₂, 2 CaCl₂, 10 HEPES, 10 D-glucose at a pH of 7.4 adjusted with 1 M NaOH. The heart was then transferred to a custom-built holding apparatus on the stage of the laser scanning microscope (see Figure 13). The holding apparatus (designed and manufactured by Mark Soonpaa, PhD) consisted of a 35mm O.D. plastic Delta T Dish with a 23 mm central aperture and a 170 μm thick glass coverslip at its bottom, sandwiched between a tight-fit plexiglass insert facing the objective revolver and a double plastic ring on top. The two plastic rings were fused together at a 1 cm vertical distance by 8 equally spaced holding screws. The perfusion cannula plus seven positioning screws were hinged between the upper and lower ring, allowing adjustment of their vertical angle to lock the heart in position for imaging. Once the heart was in a fixed position, the buffer was switched to Tyrode's solution supplemented with 1 μM ryanodine (R-500; Alomone Labs; Jerusalem, Israel) and 50 μM cytochalasin D (C8273; Sigma-Aldrich; St. Louis, MO) for immobilization.

3. TPLSM image acquisition parameters

Fluorescence emission was recorded in all three channels simultaneously during pulsed illumination with 940 nm light. This wavelength is very close to the peak of the two-photon excitation cross section for EGFP as published previously^[55]. Images were taken at a zoom of 2 or 4 in the x-y dimension (pixel size = 0.207 μm and 0.103 μm, respectively) and at 0.5-μm steps in the z-direction, with a 12-bit dynamic range. Because the axial resolution of the imaging system has been measured previously to be $\geq 1 \mu\text{m}$ (increasing with tissue depth) under the imaging conditions employed^[39, 56] a z-step size of 0.5 μm was in accordance with the Nyquist criteria. A Kalman filter of 2 was used. Adjacent stacks had ~ 10% overlap and were obtained along a nominal

vertical distance of 50 μm starting from the epicardial surface. Thus, each stack was composed of 100 images. Acquisition time per stack was ~ 7 min. We obtained a total of 9 (3 x 3) adjacent stacks per heart, encompassing nominal volumes of $\sim 0.560 \times 10^{-3} \text{ mm}^3$ (zoom 2) or $0.14 \times 10^{-3} \text{ mm}^3$ (zoom 4).

4. Image pre-processing

A previous study demonstrated intrinsic fluorescence ('autofluorescence') emission from living cardiac tissue during two-photon excitation^[44]. To examine the possibility that two-photon excitation gives rise to autofluorescence spectrally overlapping with the EGFP signal under our experimental conditions, we acquired TPLSM images from Langendorff-perfused hearts of both transgenic mice and non-transgenic littermates. TPLSM z-stacks taken from the left ventricular epicardial layer of a wild-type heart during 940 nm illumination revealed punctuate signals which manifested at a higher density in the green and red channel compared with the blue channel (Figure 14A-C). Visual inspection of the volume rendered merged image stack (Figure 14D), with two small regions of the sample [white boxes in (D)] shown at higher magnification (Figure 14E), demonstrated that voxels were one of yellow (indicating co-incidence of green and red signal), cyan (indicating co-incidence of blue and green signal), magenta (indicating co-incidence of red and blue signal), or black (no signal). We did not detect green pixels in the merged stack, suggesting that the green signal was invariably associated with emission in the red or blue channel. To confirm this visual impression, we performed quantitative co-localization analyses of autofluorescence signals in two-photon image stacks from wild-type hearts. First, we generated maximum intensity xy projections of 20-slice z-stacks (axial step size, 0.5 μm) for each emission channel, which were then analyzed with ImageJ Colocalization plugin to create maps of co-localization and calculate the colocalization coefficients Mander's 1 (M_1) and Mander's 2

(M₂). Co-localization maps are shown in Figure 14F. Green and red signals [Figure 14Fa; a zoom-in view of the boxed area in (a) is shown in (b)] appear to be largely co-localized, and numerical analyses confirm this impression. In xy maximum intensity projections, the proportions of contribution to colocalization by the two channels (M₁ and M₂) are 31% for the red channel (M₁) and 98% for the green channel, i.e., 98% of the pixels containing the green signal also contained red signal. In co-localization maps between the green and blue channel [Figure 14Fc; a zoom-in view of the boxed area in (c) is shown in (d)], 97% of the blue pixels exhibited a green component. To examine whether green pixels not containing a red component co-localized with blue pixels, we first removed yellow pixels from the green channel image, using the green-red co-localization map as a mask. The result is shown in Figure 14Fe and Ff. Visual inspection of the co-localization map between the subtracted green channel image and the blue channel image suggested absence of green pixels (Figure 14Fg and Fh). Indeed, numerical analyses confirmed that 94% of the green pixels also contained a blue component. Overall, these results indicate that the vast majority of pixels containing a green signal invariably also contained either a red or a blue component.

Volume rendered two-photon z-stacks acquired from a transgenic heart are shown in Figure 14G-I, unveiling bundles of green fluorescent nerves as well as prominent punctuate fluorescence in both the green and red channel, and sparse punctuate fluorescence in the blue channel. Magnitudes of incident laser power, pixel dwell time, as well as offsets and gains of each detector were identical for image stacks obtained from the transgenic and non-transgenic heart. Inspection of the volume-rendered merged z-stack (Figure 14J) suggested two populations of green voxels. The first one was composed of voxels exhibiting an additional red (yellow color) or blue (cyan color) component, identical to what was observed in the wild-type heart. A second population of voxels, predominately aligned along nerves, was devoid of both a red and a blue component. Maximum

intensity *xy* projections for each channel were generated from the two-photon *z*-stacks, and colocalization maps were obtained (Figure 14L). Colocalization maps between the green and red channel as well as between the green and blue channel revealed large green areas of non-overlap (Figure 14La-d). Additional co-localization analyses were performed as outlined above for wild-type hearts, demonstrating the presence of a large number of green pixels lacking both a red and blue signal component (Figure 14Le-h). We interpreted these pixels as reflecting EGFP fluorescence, based on previously published two-photon EGFP emission spectra^[57].

Overall, these results supported the utility of emission fingerprints to discriminate autofluorescence versus EGFP signals in Langendorff-perfused mouse heart under the imaging conditions employed. Accordingly, all green voxels coinciding with red or blue voxels were counted as reflecting autofluorescence and were removed from the *z*-stacks as follows: each image in each of the three channels was thresholded and median filtered with a 3 x 3 kernel. Threshold levels were determined by first generating intensity histograms of areas that contained no fluorescence signal. The lower threshold was then set to the intensity value corresponding to the 75th percentile of the intensity distribution. The red and blue channel images were then multiplied by a factor of three and subtracted from the green channel to remove pixels with autofluorescence in the EGFP image. A representative result is shown in Figure 15. Image stacks were thresholded to remove background noise from individual channels by setting the lower threshold limit to a value which corresponded to the 75th percentile of the intensity distribution obtained from a fluorescence signal-free region. A flow chart of the image pre-processing steps is shown in Figure 16. Image stacks containing the extracted EGFP signal were subsequently subjected to semi-automatic neuronal tracing. Details of the tracking procedure are provided in Results.

H. Permanent coronary artery occlusion

Adult transgenic hD β H-EGFP mice were anesthetized in a chamber with 3.5% isoflurane in oxygen. Once anesthesia was achieved, the incision site was shaved, and the site cleaned with Betadine. Anesthesia was maintained with isoflurane (~ 2.5%) in oxygen delivered with a mask. The mouse was placed in supine position and secured with limb restraints. A midline ventral skin incision from the caudal end of the sternum to the cricoid cartilage was made. After splitting of the thyroid gland and strapping muscles with blunt forceps, an endotracheal tube was inserted. The mouse was ventilated at 180 cycles/min and approximately 0.1 cc volume with isoflurane (~ 2.5%) in oxygen. Skin was bluntly dissected from the left chest wall, the pectoralis major was retracted, and the pectoralis minor bluntly dissected from its origin from about the 2nd to the 5th rib. Using a blunt probe, the inferior border of the 3rd interspace was penetrated. Using a second probe in the same opening, the opening was spread to about 5-6 mm in length. Using 8-0 Prolene with a 6 mm 3/8 circle taper needle, a ligature was placed around the left anterior descending coronary artery, close to the inferior border of the auricle. It was tied with a double surgeon's knot. The retractors were removed. The opening between the ribs was closed with one suture (4-0 silk) around the surrounding ribs. The pectoral muscles were returned to their original positions, forming dual flaps over the incision. The skin incision was closed with interrupted sutures and the animal was weaned off the respirator.

I. Statistical Analyses

The *t*-test or Mann-Whitney Rank Sum test was used for comparison between two groups. The Kruskal-Wallis test (followed by Dunn's *post-hoc* test) was used for comparison between multiple groups. Values are presented as mean \pm SEM. SigmaPlot (Systat Software, Inc.; San Jose, CA) was used for all statistical analyses.

III. Results

A. Transgene expression in postganglionic sympathetic neurons

The Palmiter laboratory previously demonstrated the ability of a 5.8 kb fragment of the human D β H gene 5' flanking region to target expression of *lacZ* to noradrenergic and adrenergic cells of the peripheral sympathetic nervous system, adrenal medulla, and brain^[4]. Here, we used the D β H promoter to direct expression of EGFP to sympathetic neurons in mice. Transgenic and control mice, between 12 and 38 weeks of age, were assayed for EGFP expression using immunohistochemistry. A total of 7 independent mouse lines bearing D β H-EGFP transgenes were examined, and EGFP expression in sympathetic ganglia could be detected in 6 of these. To examine transgene expression, 3 animals were selected from each of the various lines and cryosections from their superior cervical and stellate ganglia were processed for anti-GFP immunofluorescence. We observed that, in 5 out of the 6 EGFP-expressing lines, only a fraction of sympathetic neurons located in these ganglia expressed the transgene. Fluorescence screening of sympathetic ganglia from the remaining mouse line suggested high penetrance of transgene expression. Accordingly, this line was subjected to extensive analyses. Dual anti-TH and anti-GFP immunostaining of cervical and stellate ganglia revealed that GFP expression was restricted to TH-positive cells, i.e., sympathetic neurons (Figure 17A-D), whereas no anti-GFP immunoreactivity was observed in nontransgenic controls (Figure 17E-H). Penetrance, defined as the percentage of tyrosine hydroxylase-positive neurons expressing EGFP, was on average $94 \pm 1\%$, based on analyses of 8 ganglia distributed among 4 hD β H-EGFP mice between 12 and 38 weeks of age. Consequently, line 4 was used for experiments. Only results from mice which had been backcrossed into the DBA/2J background for > 5 generations were used for analyses. The 95% penetrance is identical to that previously found in superior cervical

ganglion neurons of a transgenic mouse line expressing a nuclear localized *E. coli* β -galactosidase under control of the hD β H promoter (95%^[4]). The small fraction of neurons not expressing the reporter transgene may represent dopaminergic cells, in accordance with previous immunohistochemical evidence for the existence of TH-positive, D β H-negative cells in the superior cervical ganglion of adult rodents^[58]. It is also possible that methylation of the transgene^[59] silenced its transcription and/or expression levels of EGFP were too low to be detectable by immunofluorescence.

EGFP was found to be distributed throughout the cyto- and nucleoplasm of sympathetic neurons. This subcellular distribution pattern is in agreement with previous observations in other transgenic GFP reporter mouse lines^[52]. Size and morphology of transgenic neurons appeared to be unaltered compared with non-transgenic cells. Further, volume rendering of a confocal z-stack taken from an adult hD β H-EGFP stellate ganglion also revealed EGFP labeling of proximal dendrites (Figure 18), supporting the notion that EGFP molecules had diffused or had been transported along axons to stain sympathetic neurons in their entirety, including their intracardiac segments. To confirm this, histological sections from an adult hD β H-EGFP heart were reacted with anti-TH and anti-GFP primary antibodies, followed by fluorescently labeled secondary antibodies, and subjected to confocal fluorescence microscopy. A representative result is shown in Figure 19. Pixels containing EGFP were found to coincide with pixels containing TH, as indicated by the abundance of white voxels in the merged image (Figure 19C and D). Overall, these results strongly supported the notion that the intramyocardial EGFP distribution tracks sympathetic nerves in our reporter mouse model, warranting additional, more detailed, numerical colocalization analyses as described below.

A few previous studies have raised the possibility that EGFP expression can be toxic in transgenic mice^[60, 61]. To examine this

possibility, we performed a number of additional analyses in mice between 12 and 38 weeks of age. Average heart weight/body weight ratio of mice was similar between genotypes (Figure 20A), and transgenic hearts appeared macroscopically and microscopically normal (Figure 20B and C). Mean densities of sympathetic neurons in peripheral ganglia or of sympathetic nerves in the heart were not significantly different between transgenic and non-transgenic mice (Figure 21A and 22). Transmembrane action potentials recorded from isolated wild-type and transgenic sympathetic neurons were super imposable (Figure 21B). Overall, these results support the notion that prolonged expression of EGFP had no detectable adverse effects on cardiac and sympathetic nerve structure, or on sympathetic neuron function.

B. Intramyocardial EGFP distribution tracks sympathetic nerves in hD β H-EGFP hearts - quantitative co-localization analyses

We initially determined the maximum amount of co-localization that could be measured under our imaging conditions and with our labeling techniques. Sections from an adult non-transgenic heart were incubated with a tyrosine hydroxylase antibody, followed by dual labeling with Alexa546- and Alexa633-conjugated secondary antibodies, and subjected to laser scanning confocal microscopy. Representative 3D renderings of 30-slice confocal z-stacks (axial step size, 0.3 μ m) from the red and far-red channel are shown in Figure 23A and B, respectively. Maximum intensity xy projections of both channels were generated to obtain co-localization maps and calculate Pearson's correlation coefficients with ImageJ Colocalization plugin. A representative example is shown in Figure 23C. There was extensive spatial overlap of the two fluorophores, as evidenced by the appearance of white pixels along the tyrosine hydroxylase-stained nerves. This experiment defines the empirical upper limit of the Pearson's co-localization coefficient, $95 \pm 1\%$, and reflects a small residual mismatch between the image pairs, which may result from limitations of image processing and/or labeling proteins with antibodies.

Because secondary antibodies were polyclonal, multiple epitopes on IgG molecules are targeted, making competitive inhibition of secondary antibody binding an unlikely explanation for the small mismatch. Representative examples of confocal image stacks obtained from sections that were double immunostained with antibodies against Cx43 and TH are shown in Figure 23D and E, respectively. These proteins are expected to distribute independently from each other and should therefore be ideal candidates for determination of the empirical lower limit of co-localization. Analyses of maximum intensity xy projections of the two-channel merged confocal z-stacks from TH and Cx43 double stained sections yielded the lower limit of Pearson's co-localization coefficient, $-23 \pm 17\%$, consistent with a lack of coincidence of the two proteins (Figure 23F).

Next, we quantified the extent of co-localization between TH and EGFP in cardiac sections from adult hD β H-EGFP hearts, the results of which are presented in Figure 24. A representative pair of volume-rendered z-stacks from the left ventricular myocardium of an hD β H-EGFP mouse is shown in Figure 24A and B. Maximum intensity xy projections of the merged z-stack were obtained and subjected to co-localization analyses. The abundance of white pixels in the co-localization map (Figure 24C) implies that most of the EGFP was co-incident with tyrosine hydroxylase, and the numerical analysis presented in Figure 24D confirms the visual impression: the correlation coefficient, averaged across a total of 15 pairs of identically labeled image stacks, was $91 \pm 1\%$. This value was not significantly different ($p > 0.05$) from the empirical maximum that we can record with this technique. Average Pearson's coefficients from the other anatomic regions for which quantitative co-localization analyses were performed, ranged between $87 \pm 2\%$ in the right ventricle to $92 \pm 1\%$ in the right atrium (Figure 24D). Again, the magnitudes of region-specific coefficients were not significantly different from each other nor from the empirical maximum of co-localization ($P > 0.05$), with the exception of the coefficient for the RV which significantly differed from the

empirical upper limit ($P < 0.05$). In a total of 70 image stacks distributed among 3 transgenic hearts, each stack encompassing a volume of $\sim 28,000 \mu\text{m}^3$, we found one example of a tyrosine hydroxylase-expressing intracardiac nerve, that did not stain for anti-GFP immunoreactivity (Figure 25). This observation is consistent with the 95% penetrance of transgene expression as measured at the ganglionic level (see Figure 1). Thus, this nerve segment may belong to a non-catecholaminergic neuron, or the absence of EGFP may result from transgene methylation. We did not detect EGFP-expressing nerves that were tyrosine hydroxylase negative, confirming the specificity of transgene expression at the level of individual intracardiac axons. Overall, these results support the notion that the intracardiac EGFP distribution faithfully recapitulates the microanatomy of the sympathetic network and further suggests its suitability to image sympathetic nerves in living heart.

C. Live morphology of the local sympathetic network in left ventricular subepicardium as reconstructed from two-photon imaging data

We next sought to examine the utility of the hD β H-EGFP mouse model in conjunction with TPLSM imaging and semi-automated three-dimensional reconstruction tools to generate wiring diagrams of local sympathetic networks in living heart. We chose to study innervation in subepicardial layers of the left ventricular free wall for three reasons. First, this anatomical region is readily accessible to fluorescence imaging by two-photon excitation microscopy of the intact heart^[52]. Second, sympathetic axons invade the cardiac muscle from the epicardial surface and begin to branch in the sub-epicardial layer prior to innervating their target cells in the same or deeper layers of the ventricular myocardium^[10, 11]. We thus argued that three-dimensional reconstructions of the EGFP fluorescence distribution in this region would provide valuable information on organizational principles of the cardiac sympathetic network. Third, previous studies by others have demonstrated marked structural remodeling of sympathetic innervation in the epicardial border zone of

chronic myocardial infarctions. Thus, direct comparisons of the three-dimensionally reconstructed epicardial sympathetic subnetworks obtained from uninjured and infarcted hearts would provide an opportunity to gain insights into disease-related variations in cardiac sympathetic wiring.

A representative example of a three-dimensional reconstruction of EGFP-expressing, i.e., sympathetic, axons from two-photon imaging data acquired in a living heart is shown in Figure 26A. All EGFP-labeled axons in a 230 μm by 280 μm by 50 μm volume within the outermost left ventricular epicardial layer in an adult hD β H-EGFP heart were imaged by TPLSM and processed images were reconstructed in 3D using Amira software. The data set consisted of 9 image stacks, each stack containing 100 images (12-bit, 512 x 512 pixels).

The sympathetic axons innervating the heart usually have their somata in the cervical or upper thoracic ganglia remote from the imaged region. They, thus, cannot be imaged in the same procedure. Previous studies by others, both anatomical and functional, have demonstrated that postganglionic efferent fibers project to the great vessels, invade the base of the heart, and run over the epicardial surface predominately in multi-nerve bundles. Individual fibers eventually branch off their bundles to enter the deeper layers of the myocardial wall. In agreement with those findings, volume rendering of all EGFP-labeled axons in two-photon image stacks revealed the presence of two nerve bundles on the epicardial surface (demarcated by arrowheads in Figure 26A; magnified views of portions of each epicardial bundle are shown in panels Ba and Bb of Figure 26). No axon branches off the epicardial nerve bundle marked by the yellow arrowheads. In contrast, the second nerve bundle (denoted by red arrowheads) executes a sharp, nearly orthogonal, inward turn before invading the myocardial wall and eventually splitting into its constituent two axons (Figure 26Bc).

Some intramural axons (denoted by asterisks in Figure 26A) were found to follow a zig-zag trajectory, wherein segments of the same axon

running tangentially to, but at different depths from, the epicardial surface are connected by axonal portions that project radially, i.e. parallel to the transmural axis. In addition, some of the tangentially projecting axon segments run parallel to each other over distances of several tens of microns with more or less regular spacing between them. Such ordered arrangement probably reflects the alignment of axons in parallel to the long axes of the cardiomyocytes, because epicardial myocytes have been shown previously to preferentially orient their longitudinal axes to the surface lining^[62].

Radially projecting portions of sympathetic axons (denoted by asterisks in Figure 26A) span transmural distances ranging from 10.8 to 29.4 μm . These values exceed the average depth of rodent ventricular cardiomyocytes ($\sim 13 \mu\text{m}$ ^[63]) by 2- to 3-fold, suggesting that those axonal segments extend over several layers of myocytes. Thus, the staircase-like 3D trajectories of single axons in conjunction with en passant neuroeffector junctions enables synchronous signal transfer to multiple cardiomyocytes lying at different tissue depths within laterally adjoined muscle regions, providing a structural basis enabling uniform sympathetic activation within the target tissue.

Axonal branching in the target zone enables innervation of multiple cells by the same neuron, further promoting uniformity of the tissue's response to neural stimuli. In the 2-p imaging data shown in Figure 26, we found multiple bifurcations (magnified views of two bifurcation examples are displayed in panels *Bd* and *Be*), as well as one example for a trifurcation (Figure 26*Bf*).

Most intramural neurites typically exhibited high contrast in EGFP fluorescence, giving rise to their punctuated morphology as shown in Figure 26*Bg* and *Bh* and Figure 27A and B. Note the presence of multiple loops of different sizes that are arranged both in series and in parallel with each other along the intramural course of a sympathetic axon (Figure 27B).

An identical pattern of periodic, intensely fluorescent axon swellings (boutons) that were connected by thin, weakly fluorescent segments, was also seen in confocal image stacks obtained from fixed cardiac sections double immunostained for tyrosine hydroxylase and sarcomeric α -actinin, to outline sympathetic nerves and cardiomyocytes, respectively (Figure 27C). This result indicates that the punctuated fluorescence pattern of EGFP-labeled neurites mirrors the normal microanatomy of intramural sympathetic fibers. Further, immunofluorescence analyses of cardiac sections support the notion that the boutons constitute the neurotransmitter release sites, i.e., neuroeffector junctions, as indicated by the expression of synapsin I, a synaptic protein necessary for neurotransmitter exocytosis (Figure 27D). The high density of these release zones along much of the length of axon-cell contacts facilitates spatially and temporally coordinated dispersion of the sympathetic input signal within the target tissue.

To reconstruct the 3D trajectory of the sympathetic arbor from the two-photon imaging data and derive from it the axonal branching topology, we adapted a previously developed semi-automated tracing algorithm. The reconstruction is based on a geometric model wherein neurite segments are approximated as discrete series of circular cylinders (termed 'snaxels') which are generated by moving a two-dimensional circular cross section along an axis in three-dimensional space (see Figure 28A). The direction of the axis can change with location along a neurite segment, and the cross section is always perpendicular to the tangent of the axis. To achieve maximal congruency of the reconstructed neurite segment with the two-photon image stacks, the snaxels' axes and diameters are fitted into the image data using the active contour model by Kass et al.^[64]. To outline the connectedness among reconstructed neurite segments, their respective midlines are connected to each other at branching points (denoted by arrow in Figure 28A), giving rise to a 3D skeleton of the axonal arbor.

The tracing procedure is illustrated in Figure 28B-H. A bifurcating portion of an EGFP-labeled sympathetic neurite is shown as volume rendering from a stack of two-photon images (Figure 28B). The voxel size was 0.2 μm by 0.2 μm by 0.5 μm . The user selects a starting and an end point (white and yellow arrow, respectively, in Figure 28C) by clicking on the appropriate locations in the image stack. Snaxels are created at these points and are connected by automatically inserting intermediate snaxels along a preliminary line at a predefined step size (red dots in Figure 28C). Each snaxel's axis and diameter are then fitted to the two-photon image stack by iteratively optimizing their values to maximize congruency of the reconstructed segment with the image data (Figure 28D). To add a new piece to the skeleton, the user selects an existing snaxel as a starting point. If the selected snaxel is an end point of a previously reconstructed segment (white arrow in Figure 28E; the starting snaxel of the new, to-be-traced segment is identical to the end point of the previous segment), the segment will be extended. To provide the endpoint of the segment to be added, the user selects an appropriate voxel in the image stack (yellow arrow in Figure 28E). A new snaxel is generated at this location and connected to the selected point by inserting additional, preliminary snaxels. The fitting algorithm is then repeated on this string of preliminary snaxels to obtain a new reconstructed segment which is then added to the existing skeleton, as shown in Figure 28F. If the selected seed point has two neighbors (arrow in Figure 28G), the snaxel becomes a branching point and a new segment will be attached to it (Figure 28H). Successive application of the neurite-tracing method to contiguous portions of the image data enables complete 3D digital reconstruction (skeletonization) of an axonal tree within the boundaries of the imaged volume as shown in Figure 28I. Following removal of each snaxel's spheric contours and connecting their center coordinates with each other, one obtains a 3D midline skeleton of the imaged axonal network (Figure 28J), allowing us to outline the branching topology of the sympathetic subnetwork. The

skeleton can be corrected manually by moving, adding, or deleting segments or branching points at any stage if necessary.

In order to verify reconstruction accuracy, two different persons independently traced the same portions of an image stack. Figure 29 shows the resulting two 3D midline skeletons, revealing no large-scale discrepancies that would have led to different interpretations of the connectedness of axonal branches. The total lengths of the traced arbors were 719 μm and 699 μm .

The complete midline skeleton superimposed onto the 3D two-photon image data set from Figure 26A is displayed in Figure 30. Axonal midlines were delineated and rendered in 3D using the semi-automatic tracing software. Visual inspection of the 3D rendered trajectory suggested that the local network is segregated into multiple subtrees. Accordingly, to further examine the spatial extension as well as the branching topology of individual subtrees within the confines of the imaged volume, we mapped 3D trajectories of two subtree arbors by selectively highlighting all axonal segments that were physically linked to subtree-specific reference points. The two reference points were chosen to be the entry point of a subtree initial segment into the volume (cyan arrow in Figure 31A) and the first branching point of a subtree close to the epicardial bundle (red arrow in Figure 31A). Overlays of the 3D subtree skeletons and the 3D imaging data are displayed in Figure 31B. Snapshots of the 3D skeletons from different view angles (Figure 31). Revealed repetitive bifurcations in either subtree. In addition, the red trajectory contained a tertiary branching node and three small-diameter loops (zoom-in views in *B*; arrows in right panel of Figure 31C), possibly innervating coronary vessel walls^[65]. Proximal segments of child axons were oriented at sharp angles with each other and/or with the distal segment of their parent branch at their bi- or trifurcation points, yet child axons were non-recurrent, i.e., they did not turn back in the opposite direction of the parent branch. Branches were of variable lengths and

changed, often abruptly, their spatial orientation, giving rise to meandering 3D trajectories. Cumulative path lengths of the red and cyan arbor in Figure 31 were 431 μm and 509.67 μm , respectively. Branching and looping patterns of the subtrees tracked in Figure 31B are schematically depicted in the axograms shown in Figure 31C, revealing marked differences in arborization patterning. Together, these findings suggest that differences in geometrical properties (i.e., length and angle of branches) between subtrees combine with those in branching and looping topology to give rise to variable configurations of the innervation domains of an axon arbor on a microscopic scale.

Because the locations of end-branches typically coincided with the image borders, they most likely exceeded the boundaries of the imaged volume, and it thus seems improbable that they represent axon terminals. Similarly, because the size of the imaged volume was too small to backtrack each subtree's proximal trajectory, we were unable to determine whether they originated from the same or different parent axons, or whether they formed connections with axons from other neurons outside the volume.

In order to further examine the relative spatial relationship of all subtrees in the image volume, we obtained their 3D trajectories and assigned them different colors. Figure 32 shows the resulting 3D color map of the trajectory ensemble from three different view angles. Close inspection of the map revealed that the individual subtree trajectories arrange to not much overlap, suggesting that each subtree arbor covers discrete tissue domains which superimpose onto and/or juxtapose with each other in the volume. The total axon length, defined as the sum of lengths of all branches, was found to be 4,271 μm , which when normalized to the total volume imaged, yielded an axon density of 0.0013 $\mu\text{m}/\mu\text{m}^3$.

Overall, the 3D reconstruction of the local cardiac sympathetic circuitry reveals organizational and structural principles that allow for

coordinated and efficient transmission of signals to a large number of cells within a finite volume of the heart. These include high density of *en passant* synaptic boutons along much of axon-cell contacts, alignment of neurite segments parallel to the main axes of their apposed cardiomyocytes, and ramification of individual subtrees both within and between tissue layers via axonal meandering, branching and looping. In addition, the approach presented here enables quantitation of total sympathetic axon length and axon density within finite volume elements in intact, living heart.

D. Live morphology of the remodeled sympathetic innervation in the peri-infarct border zone

Previous experimental studies employing immunohistochemical assays have demonstrated extensive remodeling of the cardiac sympathetic nervous system in chronically infarcted hearts of large and small mammals. The remodeling process entails both denervation and hyperinnervation, profoundly altering the spatial innervation pattern. Denervation is typically observed both in infarcted myocardium and in viable myocardium apical to the site of permanent injury. Denervation of the latter is accompanied by denervation hypersensitivity, i.e., exaggerated response to catecholamines. In contrast, the peri-infarct border zone exhibits sympathetic hyperinnervation. Clinical studies, using radioactively labeled analogs of sympathetic neurotransmitters, similarly found a co-existence of sympathetically de- and hyperinnervated regions in human patients with previous myocardial infarctions. Importantly, these alterations in sympathetic nerve density have been implicated in postinfarction arrhythmogenesis. Here, we sought to probe the utility of our hD β H-EGFP transgenic mouse model for assessment of changes in sympathetic innervation patterning occurring in the peri-infarct border zone following permanent coronary artery occlusion.

Accordingly, adult hD β H-EGFP mice underwent permanent occlusion of the distal left anterior descending coronary artery. This

procedure resulted in a myocardial infarction encompassing the left ventricular apex as shown in Figure 33A. A histological section from an infarcted heart at 2 weeks following injury revealed thinning of the apical left ventricular wall and accumulation of collagen in this area (Figure 33B). A magnified view of a lateral border zone revealed the presence of collagen bundles interdigitating between strands of surviving cardiomyocytes (Figure 33C). In addition, staining of sections from chronically infarcted hearts with antibodies directed against tyrosine hydroxylase and sarcomeric α -actinin to specifically label sympathetic nerves and cardiomyocytes, respectively, unveiled increased nerve density both in the epicardial border zone and at the junction between border zone cardiomyocytes and non-myocytes (identified by the appearance and lack of periodic anti- α -actinin immunoreactivity, respectively; Figure 33D) compared with the non-infarcted left ventricular myocardium basal to the infarct scar (lower panel in Figure 33D). Overall, these findings demonstrated the utility of our infarct model to induce sympathetic remodeling of the infarct border zone,

To examine the possibility that ischemic injury results in loss of EGFP expression in sympathetic neurons supplying the peri-infarct myocardium, we repeated quantitative co-localization analyses on infarcted hearts at 2 weeks following permanent coronary artery occlusion, employing the same approach outlined above for uninjured hearts. Accordingly, to determine the maximum amount of co-localization that could be measured under our imaging conditions and with our labeling techniques, sections from an adult non-transgenic heart at 14 days following artery ligation were incubated with a tyrosine hydroxylase antibody, followed by dual labeling with Alexa546- and Alexa633-conjugated secondary antibodies, and subjected to laser scanning confocal microscopy. Representative 3D renderings of 30-slide confocal z-stacks (axial step size = 0.3 μm) from the red and far-red channel are displayed in Figure 34A and B, respectively. Maximum intensity xy

projections of both channels were generated to obtain co-localization maps and calculate Pearson's correlation coefficients. A representative example is shown in Figure 34C. The abundance of white pixels indicates extensive spatial overlap along the tyrosine hydroxylase-stained nerves. The empirical upper limit of the Pearson's correlation coefficient was derived from a total of 5 co-localization maps obtained from the peri-infarct regions of 1 non-transgenic hearts and was found to be $92.7 \pm 0.4\%$. To determine the empirical lower limits of co-localization in hearts with healing myocardial infarction, sections were dually stained with antibodies directed against Cx43 and tyrosine hydroxylase, followed by incubation with Alexa546- and Alexa633-conjugated secondary antibodies. Representative examples of volume-rendered confocal z-stacks for the red and far-red emission channel are shown in Figure 34D and E, respectively. Analyses of 5 maximum intensity xy projections obtained of both channels yielded the lower limit of Pearson's co-localization coefficient, $1.1 \pm 0.4\%$ (value is from 5 stacks in 1 infarcted heart), consistent with a lack of coincidence of the two proteins. Note the more diffuse anti-Cx43 staining in the infarcted compared with the non-infarcted tissue (compare Figure 23D and Figure 34D), which is a typical characteristic of the peri-infarct border zone^[66]. Values for the upper and lower limit of co-localization in infarcted hearts were not significantly different from those in non-injured hearts ($P > 0.05$; Kruskal-Wallis test for multiple comparisons).

Next, we quantitated the extent to which tyrosine hydroxylase and EGFP co-localize in cardiac sections from adult, chronically infarcted hD β H-EGFP hearts. The results are summarized in Figure 35. A representative pair of volume-rendered z-stacks from the peri-infarct border zone of an hD β H-EGFP heart is shown in Figure 35A and B. Maximum intensity xy projections of the merged^[66] z-stack were obtained and subjected to co-localization analyses. The abundance of white pixels in the co-localization map (Figure 35C) indicated that most of the EGFP

was coincident with tyrosine hydroxylase. This visual impression was confirmed by the numerical analyses, because the correlation coefficient, averaged across a total of 5 pairs of identically labeled image stacks from the same heart of which the empirical limits were derived, was $85.7 \pm 3.7\%$. This value was not significantly different from the empirical upper limit of co-localization that we can record with this technique ($92.4 \pm 0.4\%$; $P > 0.05$ by Mann-Whitney Rank Sum -test). Overall, these results support the notion that the EGFP distribution reproduces the anatomy of the sympathetic nerves in the border zone of chronic myocardial infarctions, suggesting the suitability of the transgenic hD β H-EGFP mouse model to track remodeling of the cardiac sympathetic network in previously infarcted, living heart.

We next sought to obtain a three-dimensional reconstruction of EGFP-expressing axons from two-photon imaging data acquired in a living, previously infarcted heart. All EGFP-labeled axons in a $250 \mu\text{m}$ by $280 \mu\text{m}$ by $50 \mu\text{m}$ volume within the epicardial border zone in an adult hD β H-EGFP heart at 2 weeks after ligation of the distal left anterior descending coronary artery were imaged by TPLSM. The images were processed as outlined above (see also flow-chart of image processing in Figure 16), and the processed images were rendered in 3D using Amira software. The entire data set consisted of 9 image stacks, each stack containing 100 images (12-bit resolution, 512×512 pixels). Volume renderings of the two-photon image data are displayed in Figure 36A.

A $+90$ degree rotation of the 3D rendered image data about the y axis (Figure 36A, middle panel) reveals nearly complete absence of EGFP-expressing axons at tissue depths between 10 and $50 \mu\text{m}$ below the epicardial surface. Only a few axon fragments were detected at depths exceeding $10 \mu\text{m}$ (denoted by arrowheads in Figure 36A), giving rise to a steep, epi- to endocardially oriented innervation gradient within the image volume. This pattern sharply contrasts with the spread of EGFP-expressing axons across the entire epicardial-endocardial axis in 3D

image data sets obtained from the left ventricular subepicardium of uninjured hD β H-EGFP hearts (see Figure 26 and 27). Also, sympathetic nerve density appeared to largely vary within the anterior portion of the imaged volume. Close inspection of the three-dimensionally reconstructed image data revealed that axons in small subvolumes (denoted by the red rings) were observed to form convoluted fiber loops, locally increasing axon density. Figure 36*Ba* displays a representative example of two connected loops. Overall, these findings suggest that both loss and gain of axons occur simultaneously on a microscopic scale within the epicardial peri-infarct border zone, locally altering sympathetic innervation patterning. These non-uniform changes in sympathetic nerve density assessed by 3D rendering of tissue EGFP fluorescence are in agreement with those seen in accompanying immunohistochemical analyses (Figure 33), further supporting the utility of our model for tracking sympathetic axon reorganization associated with chronic ischemic injury.

Visual inspection of the 3D image data further unveiled the presence of larger-diameter axon loops. A representative example is demonstrated in Figure 36*Bb*. Overall, these observations suggest that multiple axon loops with variable diameter and geometry co-exist within the anterior compartment of the imaged volume. Axon loops with variable circumferential length were also observed in two-photon image stacks obtained from uninjured hearts (see Figure 27), suggesting that looping constitutes a physiological structural component of the cardiac sympathetic network.

Sympathetic nerves in the imaged border zone cuboid followed a predominantly tangential trajectory and were observed to run in bundles or as solitary nerve fibers. Representative examples of nerve bundles splitting into their respective two constituent axons are shown in Figure 36*Bc* and *Bd*. Binary or tertiary branching of solitary fibers was frequently observed throughout the imaged volume. Representative examples of a bi- and trifurcation are displayed in Figure 36*Be* and *Bf*, respectively.

EGFP fluorescence pattern was largely variable both within and among individual axons. Some axonal segments exhibited smooth contours with little variation in diameter, whereas others displayed periodic swellings alternating with thin interconnecting segments (Figure 36Bc and Be, respectively). Occasionally, these axonal swellings were eccentric with respect to the axon's midline (arrowheads in Figure 36Bf).

We subsequently used the semi-automatic tracing algorithm to generate the 3D wiring diagram of the imaged network. Overlays of the 3D skeleton and the 3D image data are presented in Figure 37. Visual inspection of the 3D skeleton (Figure 38) suggested that multiple axonal loops with variable diameter and geometry interconnect to form plexuses. To further explore plexus topology, we sequentially traced the 3D trajectories of all identified loops that were physically linked with each other within a selected subvolume. Trajectories of individually identified loops were assigned different colors and superimposed onto the 3D display of the two-photon image data set to generate the loop map shown in Figure 38. The map unveils several distinct structural properties of the axonal plexuses. First, trajectories of juxtaposed loops were observed to partially overlap, giving rise to a nested-loop configuration of the local network. Second, portions of individual loops could be heterogeneous with regard to fiber morphology and axonal branching topology. Third, single loops followed meandering trajectories of largely varying lengths. The spatial distribution of loop lengths appeared to be random. Loop lengths ranged from $\sim 23 \mu\text{m}$ to $\sim 872 \mu\text{m}$. Fourth, a small subset of juxtaposed loops were coupled in series via short axonal segments (see asterisk in Figure 38). Recent studies, both experimental and computational, support the notion that direct electrical coupling between axonal loops of variable lengths can be the origin of network high-frequency oscillations^[67]. Thus, axonal reorganization seen here may have profound implications for sympathetic signaling in the epicardial border zone of chronic myocardial infarctions.

Overall, these results demonstrate that the combined use of transgenic reporter technology, two-photon fluorescence microscopy and quantitative image processing tools enables high-fidelity 3D reconstructions of myocardial infarction-induced sympathetic remodeling on a microscopic scale in the living, intact mouse heart. The remodeling process includes spatially heterogeneous loss and gain of sympathetic fibers, significantly altering microscopic innervation gradients within the peri-infarct border zone, as well as promotion of axonal looping, giving rise to a nested-loop architecture of the axonal circuitry. Loop length distribution and loop connectivity likely determine the electrical activity of the local network and, thus, sympathetic input to the underlying tissue.

IV. DISCUSSION

A. Major findings

The key observations of the present study are as follows:

1. We have established a transgenic mouse line in which the human dopamine- β -hydroxylase gene promoter targets expression of EGFP to noradrenergic cells of the peripheral nervous system. Specifically, EGFP labeled postganglionic sympathetic neurons in their entirety, including cyto-, nucleo- and axoplasm. Transgene expression had no discernible adverse effects on sympathetic neuron structure or function.
2. EGFP distribution in adult hD β H-EGFP hearts faithfully recapitulated the anatomy of the cardiac sympathetic nervous system.
3. With TPLSM and semi-automated 3D reconstruction tools, we were able to obtain 3D wiring maps (connectomes) of the sympathetic arbor in a finite volume of circuitry within the left ventricular subepicardium of living, Langendorff-perfused hD β H-EGFP hearts.
4. In the uninjured heart, individual axons were observed a) to bifurcate symmetrically along their paths, b) to project both tangentially and radially across the image volume, c) to form *en passant* boutons along much of their intramural trajectories, d) to give rise to juxtaposed loops of variable lengths nested within each other, and e) to extend beyond the boundaries of the imaged volume.
5. In the epicardial border zone of a chronic myocardial infarction, we found a) profound axonal reorganization including localized loss and gain of sympathetic fibers, b) higher-order axonal branching, and c) formation

of axonal plexuses composed of nested loops of variable circumferential length.

In this work we demonstrate the basic utility of transgenic technology to label neuronal populations, combined with TPLSM and 3D image analyses tools, to reconstruct the local wiring diagram of the sympathetic nervous system in living whole heart. Although the finite volumes of the imaged tissue contain axons entering and leaving the volume, precluding complete reconstruction of the local sympathetic circuitry, this approach provides, to the best of our knowledge, the first glimpses at the 3D micro-architecture of the left ventricular sympathetic arbor in living heart. The results thus constitute a starting point to unravel the structural organization of the cardiac sympathetic nervous system. Cataloguing the connective information in well-defined sample volumes will aid in understanding how individual axons integrate into the organization of the circuit. Also, comparing corresponding connectomes between different hearts can help dissect the contribution of genetics and disease to circuit organization and/or function.

B. Transgenic approaches for labeling peripheral sympathetic nerves

Transgenic technology has been widely used to direct expression of GFP or its spectral variants to neuronal populations in a variety of species. For example, the Lichtman laboratory previously generated transgenic mouse lines in which expression of spectral GFP variants (termed XFP) was driven by the neuron-specific *thy1* promoter^[68]. Transgenic XFPs were shown to label axons *in vivo* over centimeter-long distances although they were not fused to peptides designed to facilitate their transport (e.g., GAP-43 or Tau). Among other neuronal cohorts, XFP expression was also readily detectable in a fraction of postganglionic sympathetic neurons of superior cervical ganglia, labeling them in their entirety. The Fukuda laboratory previously generated sympathetic nervous system-specific EGFP reporter mice by crossing D β H-Cre recombinase

transgenic mice with EGFP-floxed mice and reported that 57% of the neuronal bodies of the stellate ganglia were marked with EGFP^[69]. However, information about intracellular EGFP labeling pattern was not provided. Finally, the utility of tyrosine hydroxylase promoter-driven transgenic EGFP expression for tracking sympathetic axon sprouting *in vivo* has recently been demonstrated^[70]. Our results confirm the earlier observation by the Palmiter laboratory demonstrating the ability of the cloned hD β H gene promoter to direct expression of a reporter protein to noradrenergic cells of the peripheral nervous system^[4]. In addition, our systematic analyses indicate almost complete penetrance of transgene expression in the target cohort as well as EGFP labeling extending over centimeter-long distances along individual axons, including intramyocardial fiber segments. Very importantly, levels of reporter protein expression were adequate for *in vivo* imaging by two-photon molecular excitation, without evoking discernible toxicity. Overall, these features support the unique utility of our reporter mouse model for both quantitation of sympathetic axon density and reconstruction of sympathetic axon connectivity in intact, living heart.

C. Quantifying cardiac sympathetic innervation

Cardiac sympathetic nerve density is an important determinant of the functional response of the myocardium to sympathetic nerve activity. Conventional methods to quantitate sympathetic innervation in heart muscle often involves embedding and sectioning^[31, 71] or dehydration and heating^[14, 26]. Such techniques can markedly perturb tissue histomorphology compared to what is manifested in the intact system. The method we present here allows quantitation of total axon length per unit volume of tissue within intact, living heart, i.e., under conditions of preserved three-dimensional structure. We further suggest that total axon length per unit volume of tissue is a useful standard for reference while acknowledging that neurotransmitters are likely to be released *en route*

from varicosities positioned along intramural axons (see below). *In vivo* quantitation of neuroeffector junction density clearly requires novel approaches to mark functional sites of adrenergic transmitter release.

D. Micro-architecture of the cardiac sympathetic nervous system

Based on three-dimensional reconstructions of the sympathetic subnetwork in the left ventricular epicardium, we are able to identify several organizational principles that synergistically contribute, on a microscopic scale, to a spatially and temporally coordinated distribution of sympathetic signals to the target tissue. These include multiplicity of neuroeffector junctions along much of the axon-cell contact as well as branching and looping of axons while they meander, both radially and tangentially, over distances of several hundreds of microns through the tissue volume. Further, subtree arbors within a ~ 4.5-nl tissue volume arrange not to overlap very much, giving rise to multiple annexed innervation domains of variable complexity and configuration.

Three-dimensional reconstructions of two-photon image data revealed that the postganglionic sympathetic neurons do not form discrete nerve terminals, suggesting that neurotransmitters are released along intramural axons. Co-staining of cardiac tissue for sarcomeric α -actinin, tyrosine hydroxylase and synapsin I, a peripheral membrane protein of synaptic vesicles^[15], revealed clustering of synapsin I in sympathetic axon swellings, i.e., varicosities, that were in physical contact with cardiomyocytes. Although synapsin I accumulation may not necessarily mark functional sites of transmitter release, our findings strongly support the notion that release occurs at closely spaced but discrete sites along the entire axon-cell contact. Such patterning of synapses enables propagating impulses to successively trigger transmitter secretion from a string of varicosities, contributing to a coordinated sympathetic activation of the target territory.

Volume-renderings of the two-photon image stacks further revealed that portions of intramural axons projecting tangentially to the epicardial surface run parallel to each other with more or less regular spacing between them (see Figure 26). Intriguingly, previous studies by others have demonstrated that the majority of left ventricular epicardial cardiomyocytes are oriented with their longitudinal axes approximately tangential to the epicardial lining^[62], and, further, that myocardial capillaries preferentially run parallel to the long axes of their juxtaposed cardiomyocytes^[72]. It is therefore tempting to speculate that sympathetic fibers extend predominately alongside their apposed cardiomyocytes and capillaries. Such triple co-linearity may serve to optimize the frequency of sympathetic synapses per axon/per myocyte, while reducing effective neurotransmitter diffusion distances to nearby capillary endothelial cells. Studies utilizing multiple cell-lineage specific markers simultaneously are necessary to delineate the topographic anatomy of nerves, capillaries and cardiomyocytes in heart.

3D wiring maps demonstrate that the local sympathetic circuitry is partitioned into multiple, minimally-overlapping axonal subtrees, each one following radial and/or tangential trajectories over cumulative distances of up to several hundreds of microns through a ~ 4.5-nl image volume. Because trajectories did not start and/or did not terminate within the boundaries of the volume, the measured total wiring length of an individual subtree arbor likely represents an underestimate. Thus, the omnidirectional expansion of an axonal sub-tree, in association with the close spacing of sympathetic synapses along much of the axon-cell contact, serves to ensure rapid distribution of the sympathetic signal to cells disseminated both within and between layers of the myocardium.

It is noteworthy that despite large degree of complexity and variability in subtree architecture and, thus, in spatial configuration of the innervation domain of an axonal arbor, subtrees did not seem to overlap much, as though axons of neighboring subtrees repel each other. Such

arrangement would serve to optimize inter-axonal distances, providing a structural foundation for minimizing transmitter diffusion distances between the synapses and the postsynaptic receptor sites. Future studies employing multiple, cell-lineage restricted reporter systems are necessary to delineate the anatomical arrangements between sympathetic nerves and target cells as well as to identify the mechanisms that give rise to efficient innervation coverage.

E. Sympathetic remodeling in the epicardial border zone of a chronic myocardial infarction

Our finding of simultaneous loss and gain of sympathetic axons in the border zone of a chronic myocardial infarction is in agreement with previous studies by others employing conventional immunohistological approaches for monitoring sympathetic axon density in infarcted heart tissue. For example, Cao and co-workers reported sympathetic denervation and hyperinnervation of the infarct scar and the scar-muscle junction, respectively in hearts from human patients with a history of postinfarction arrhythmias^[32]. Li et al.^[71] detected areas of disorganized sympathetic hyperinnervation along the border zone of denervated and innervated myocardium in rat hearts one week following ischemia-reperfusion injury. In rats with permanent coronary artery ligation, Clarke and co-workers similarly found sympathetic hyperinnervation in the infarct border region, and loss of sympathetic axons in viable myocardium apical to the infarct region^[73]. Our imaging data recapitulate the pronounced heterogeneity in sympathetic axon density in the border zone of chronic infarcts, strengthening the utility of our hD β H-EGFP model for investigating ischemic injury-induced sympathetic remodeling in living hearts.

One major advantage of our approach compared to conventional immunohistological techniques is the ability to three-dimensionally resolve sympathetic axon connectivity in a well-defined volume of living myocardium. Our results reveal pronounced re-organization of sympathetic

arborization in the epicardial border zone, manifested in axonal plexuses of geometrically complex configurations, including higher-order branching, irregularly sized varicosities, and formation of multiple nested and/or serial loops of variable circumferential length. Sympathetic axons in the uninjured left ventricular epicardium were also found to loop, suggesting that intracardiac axonal looping is physiological. A previous immunohistological study by the Segal laboratory revealed mesh-like arrangement of sympathetic nerves in the wall of excised, intact arteries^[65]. Thus, the location of the small-diameter loops shown in Figure 27 may coincide with a subepicardial vessel. By comparison, the looping architecture in the epicardial infarct border zone was markedly different from that in the normal heart with regard to both frequency and circumferential length of the axonal loops. Such spatial arrangement likely has consequences for electrical function of the local circuit as outlined in the following paragraph.

F. Functional implications of axon morphology and axonal tree organization

Previous studies, both experimental and computational, have provided evidence for the role of geometrical constraints in defining impulse conduction through a region of an axon^[17, 18]. For example, morphological inhomogeneities such as branch points and dilations may result in regions of low safety factor, i.e., regions where impulse propagation has a high likelihood of failing.

The presence of multiple varicosities that are distributed in an ‘*en passant*’, bead-on-a string’ manner along thin axonal branches has been shown to slow spike propagation^[74]. The degree to which synaptic boutons reduced axial conduction velocity was demonstrated to depend, apart from active electrical properties of the membrane, on the dimensions (length, diameter) of both the varicosities and the intervaricosity segments. These computational analyses suggest that alterations in axonal morphology seen in the infarct border zone, e.g. changes in bouton geometry (see

Figure 36) significantly impact on axonal conduction properties and, thus, modify the information - carrying capacity of the axon.

Axonal branch points are prone to propagation failure^[17, 18]. These failures arise because the electrical load is significantly higher on the arriving action potential, and the current generated by the parent axon is not sufficient to support propagation^[75]. In the case of axonal bifurcations, experimental studies in nonvertebrate axons have demonstrated that propagation failure can occur selectively in the thicker branch while conduction along the thinner child branch is sustained, or propagation stopped completely when both child branches exhibit similar diameters^[72]. Extrapolating from these observations to the electrical behavior of the local sympathetic network in the mammalian heart may be difficult. However, we suspect that axonal branching has important functional significance for the spatial and/or temporal transformation of impulses that occur along axonal trees and, therefore, for the distribution of the sympathetic signal in the target domain. Specifically, the occurrence of higher order branching and the shortening of internodal distances seen in some regions of the epicardial infarct border zone are likely to significantly alter impulse propagation and processing. Thus, alterations in varicosal geometry and axonal branching structure synergistically contribute to remodel sympathetic signaling in the chronically infarcted heart.

In contrast to inhomogeneities in axonal morphology, very little is known about the electrical behavior of axonal plexuses composed of nested loops. Intriguingly, recent computational analyses by the Traub laboratory suggest that axonal plexuses composed of multiple, electrically coupled, bidirectionally conducting loops are susceptible to reentry, leading to sustained high-frequency oscillations of the network^[67]. The length of the longest loop in the infarct border zone was 872 μm . The wavelength of a reentrant wave, which equals the product of conduction velocity and axonal refractory time, cannot exceed this value. Thus, for axonal refractory times typically ranging from 2 to 5 ms^[67], the magnitude

of conduction velocity may not exceed 0.17 to 0.44 m/s for reentry to occur in an 872 μm long loop. Conduction velocities as low as 0.25 m/s have previously been reported for unmyelinated axons^[76, 77], suggesting that the loop length observed in the epicardial infarct border zone is appropriate for reentrant activity. For a loop that is 872 μm long and for a conduction velocity of 0.44 m/s, the upper limit for reentry frequency would be ~ 500 Hz. An additional requirement for reentry to occur is localized conduction slowing/block along the loop trajectory. As outlined above, inhomogeneities in axonal morphology, e.g. branching, can locally impair axial conduction. Irregular spacing of branch nodes as seen in the 3D skeletons of the infarct border zone would thus provide a structural base for non-uniform impulse propagation along the loop. Collectively, these considerations support the notion that the sympathetic network in the epicardial infarct border zone is in principle capable of self-sustained electrical reentry, which in turn may give rise to high-frequency network oscillations. Future studies will need to examine the extent to which axonal reentry occurs *in situ* and impacts on function of the underlying border zone myocardium.

G. Limitations

The depth to which useful images can be collected using two-photon fluorescence microscopy is limited due to light scattering, absorption and spherical aberration^[56], restricting image acquisition to superficial tissue layers. Future technical innovations (e.g., adaptive optics^[78], use of an immersion medium that better matches the refractive index of living biological specimens, e.g., silicone^[79]) may overcome some of these limitations.

The punctuated appearance of EGFP-labeled intracardiac axons, owing to intensely fluorescent varicosities alternating with thin, weakly fluorescent intervaricosal segments, poses limitations on the ability to image details of axonal connectivity in intact tissue. The resolution of

diffraction-limited light microscopy may be insufficient even when used in conjunction with two-photon excitation to eliminate signals from out-of-focus structures. The advent of super-resolution techniques may provide a new avenue for imaging microstructures that have not been accessible with conventional light microscopy. Also, the overall fluorescence signal from and/or the EGFP labeling density in thin intervaricosal segments may have been insufficient to provide low noise images.

Imaging and analyses speeds limit the tissue volume for which a full circuit reconstruction can be obtained. Five nanoliter of heart volume resolved to the level of identifying every axon and bouton requires 3 hours to image and at least the same amount of time to analyze. Because the image volume contains axonal processes entering and leaving the volume, the local sympathetic circuit cannot be reconstructed completely. As a consequence, we were unable to determine the extent of myocardial territory innervated by individual postganglionic neurons nor were we able to assess their spatial relationships with each other (overlapping versus non-overlapping).

Finally, our fluorescence-based approach allows selective labeling of the cardiac sympathetic nervous system, but excludes information about the structural context. Future studies will need to employ a multi-color fluorescence approach in combination with cell lineage-restricted gene promoters to co-label sympathetic nerves and cellular components of the surrounding myocardium.

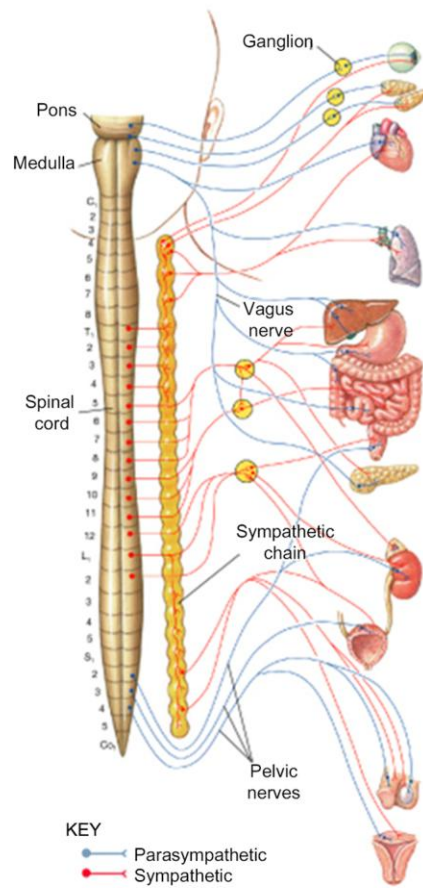


Figure 1. The autonomic nervous system
 Blue: Parasympathetic, Red: Sympathetic^[6]

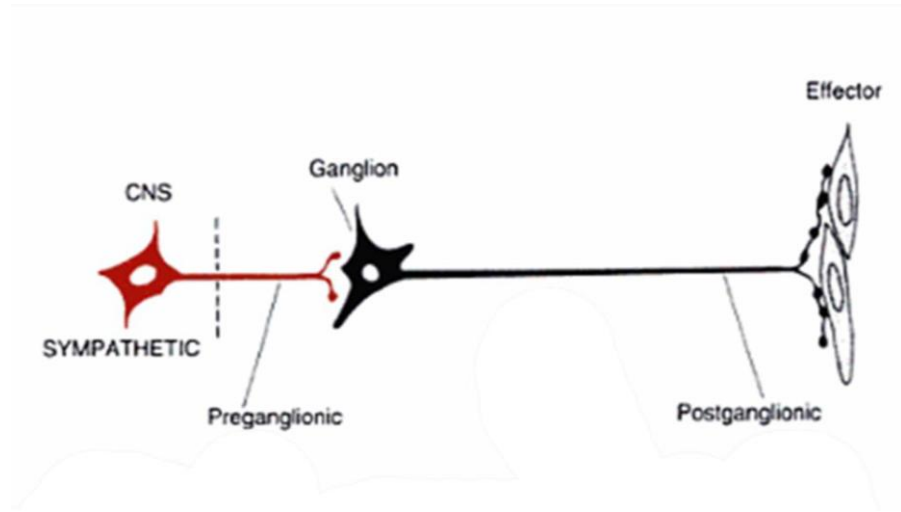


Figure 2. Anatomy of sympathetic pathways

Preganglionic fiber cell bodies originate in the spinal column and extend to paravertebral ganglia, housing the postganglionic fiber cell bodies. Postganglionic axons extend toward effectors where they branch to form plexuses of varicose neurites. Image modified from Brodal^[1]

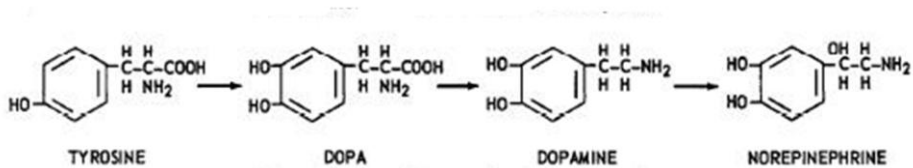


Figure 3. Norepinephrine synthesis pathway

Synthesis of norepinephrine from its precursor tyrosine in postganglionic fibers requires the enzymes tyrosine hydroxylase, dopa decarboxylase and dopamine-β-hydroxylase^[80].

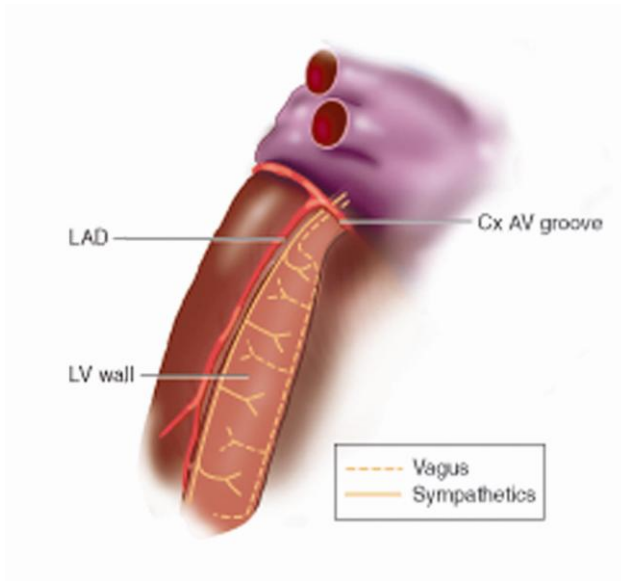


Figure 4. Cartoon depicting the anatomy of the cardiac sympathetic innervation

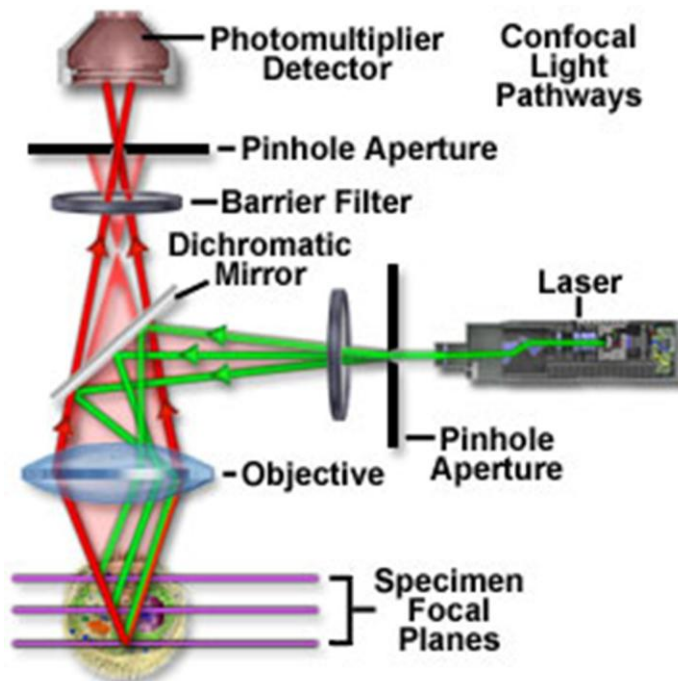


Figure 5. *Optical system of a confocal laser scanning microscope*^[81]

The laser illumination not in the plane of focus is also out of focus at the detector's pinhole aperture and is therefore excluded from entering the PMT. Two-dimensional images are built through sequentially scanning across the field in a raster pattern and are displayed on a video screen. Three-dimensional images can be rendered through stacking the optical sections on top of each other^[38].

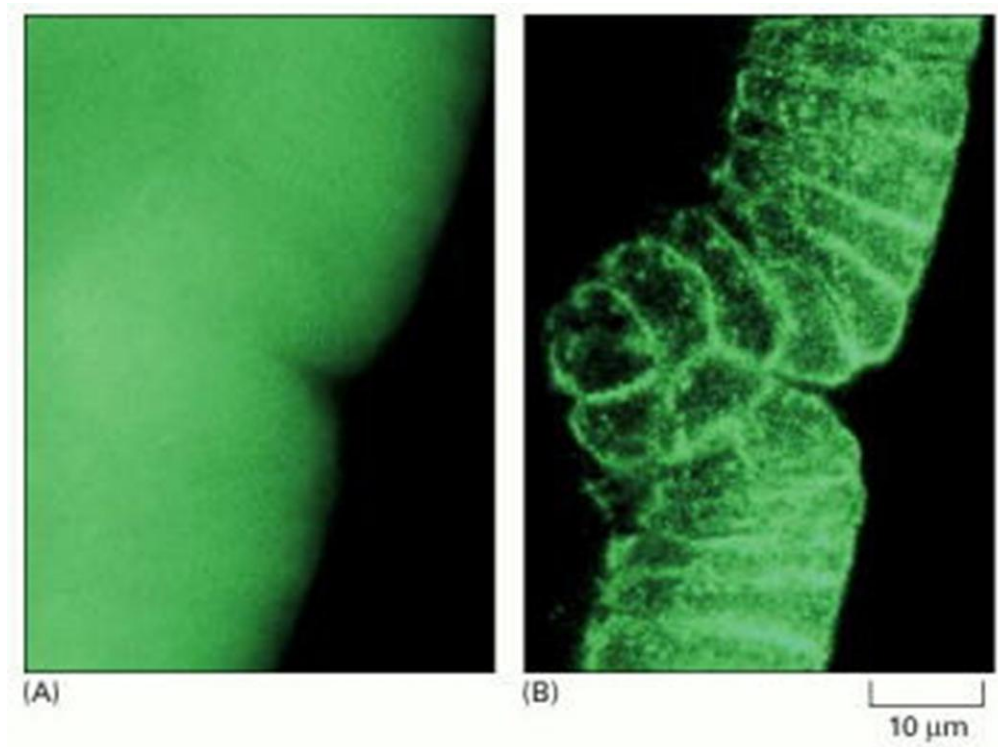


Figure 6. *Comparison between epifluorescent and confocal microscope images*

Comparison between A) epifluorescent and B) confocal microscopic images of the same intact gastrula-stage *Drosophila* embryo that has been stained with a fluorescent probe for actin filaments ^[38].

1-photon vs. 2-photon

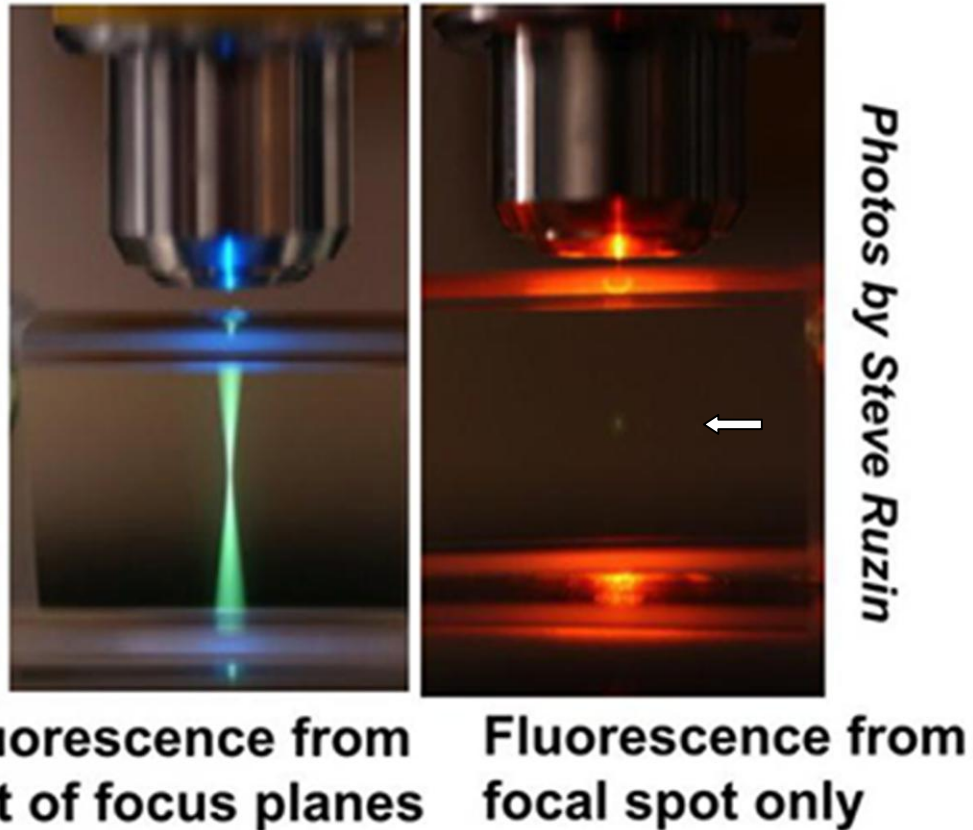


Figure 7. *Comparison of fluorescence distribution within a fluorophore-containing solution during single-photon (left) and dual-photon excitation (right)*

Delivery of continuous short-wave laser light through the objective gives rise to a bi-conical distribution of the fluorescence, with the waist being located in the focal point of the objective. In contrast, illumination with infrared pulsed laser light gives rise to fluorescence that is confined to a minuscule volume around the focal point of the objective lens (arrow). No rejection of out-of-focus fluorescence is necessary to selectively collect light from the focal plane.

<http://mcb.berkeley.edu/labs2/robey/sites/mcb.berkeley.edu.labs2.robey/files/u6/fluorescence.jpg>

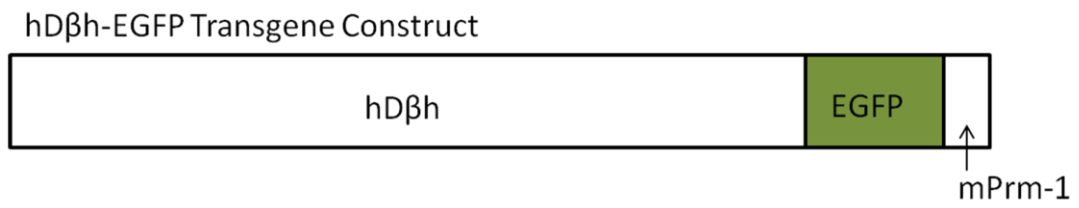


Figure 8. Schematic of the hD β H-EGFP transgene; mPRM-1, murine protamine-1

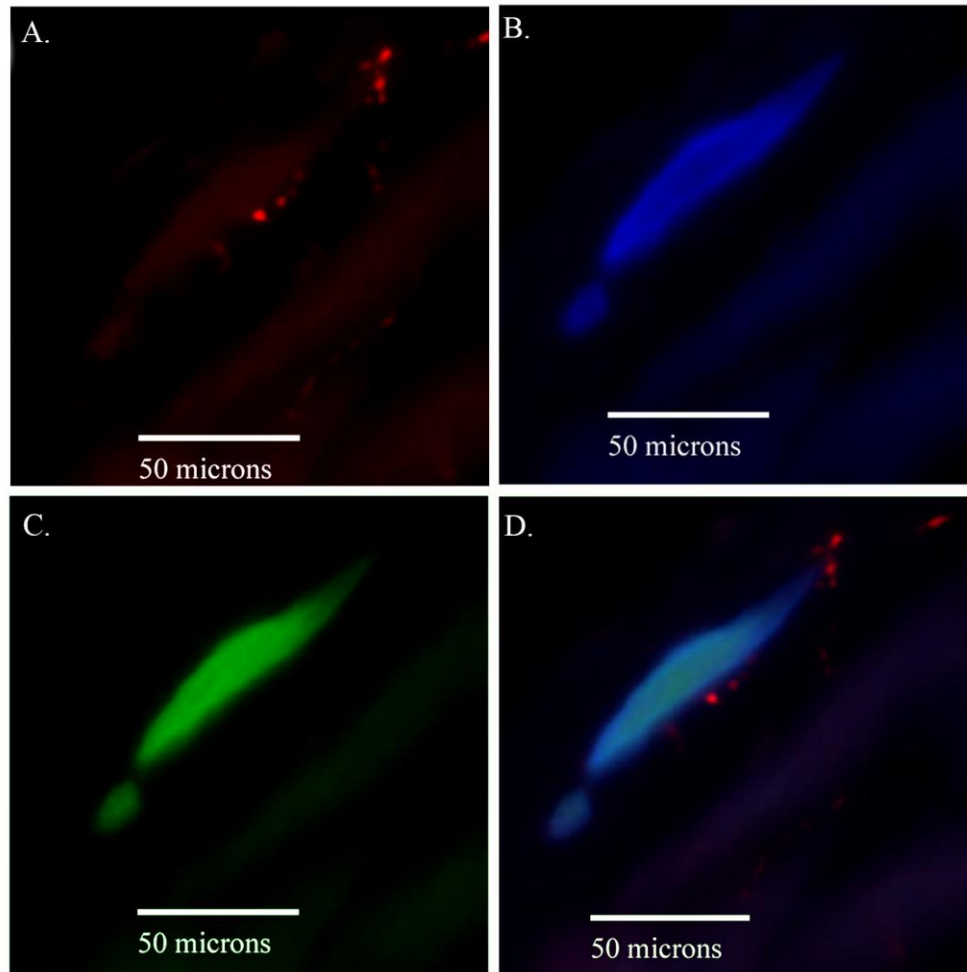


Figure 9. Specificity of primary antibodies used for co-localization analyses

A tissue section from a transgenic heart with mosaic EGFP expression was double immunostained with anti-GFP and anti-TH antibodies, followed by Dylight405- and Alexa555-labeled secondary antibodies. Panels show anti-TH (A; red Alexa555 signal) and anti-GFP (B; blue Dylight405 signal) immunofluorescence, native EGFP fluorescence in a cardiomyocyte (C), and a merged three-channel image (D). Anti-GFP and native EGFP fluorescence were co-localized, whereas there was no overlap between anti-TH and anti-GFP immunofluorescence.

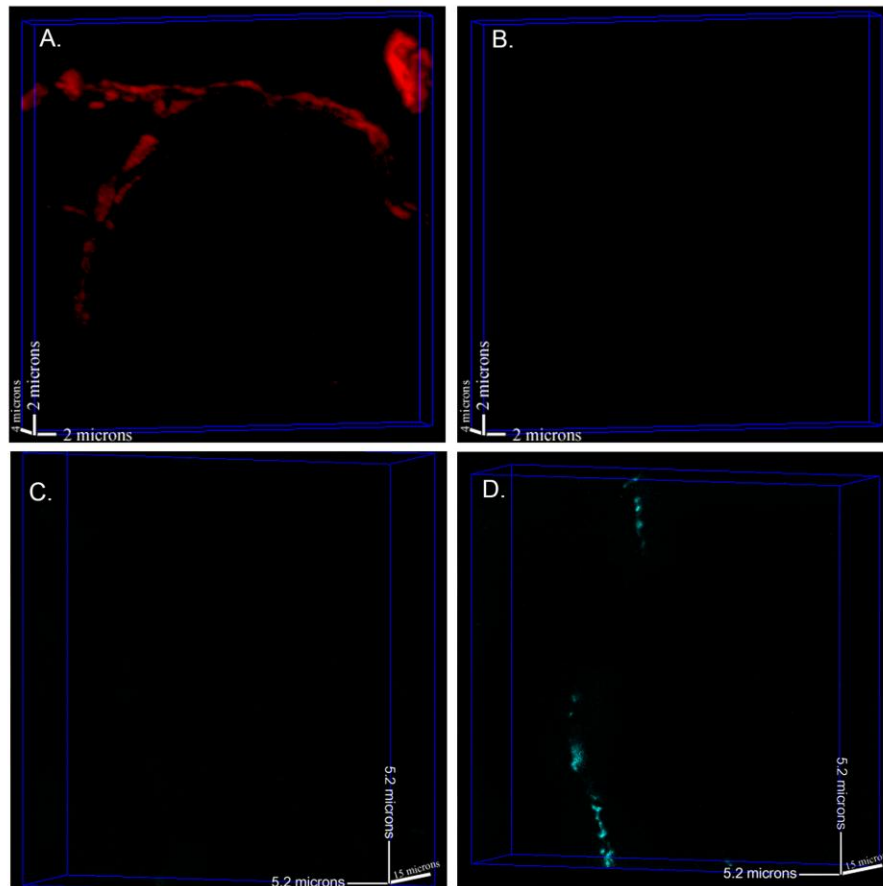
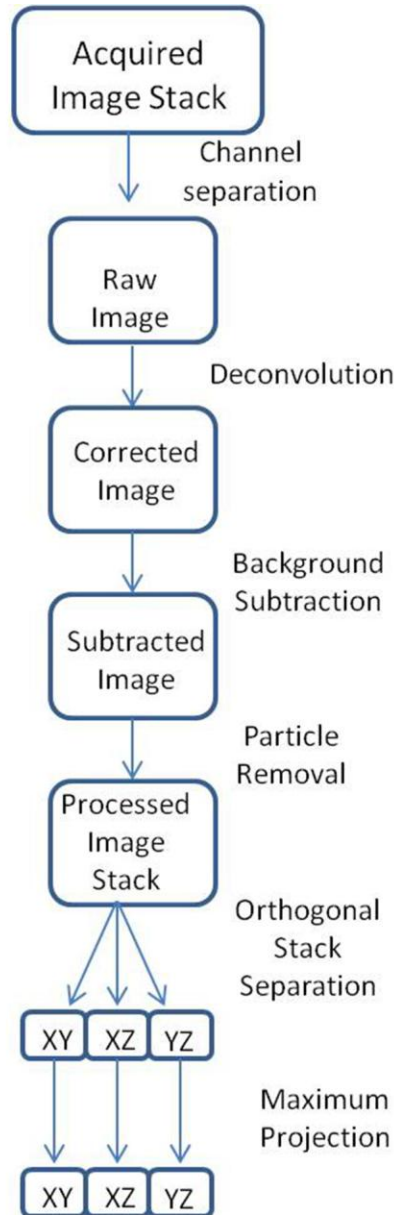


Figure 10. Examination of fluorescence signal bleed through between channels

Volume renderings of confocal z-stacks obtained across 10- μ m-thick sections from a transgenic h β H-EGFP heart immunostained with an anti-GFP antibody (A and B) or an anti-TH antibody (C and D) followed by an Alexa546- (A and B) or Alexa633- (C and D) conjugated secondary antibody, respectively. Image stacks were acquired during sequential illumination with 559 nm (A and B) and 635 nm (C and D) laser light while fluorescence emissions were recorded in the 570-625 nm (A and C) or 655-755 nm (B and D) channel, respectively. Confocal images were subjected to deconvolution, background subtraction, and filtering (see Figure 11 for a flow chart of image processing steps). We were unable to detect significant signal contamination between the two recording channels under the imaging conditions employed.

Anti-GFP
AlexaFluor 546



Anti-TH
AlexaFluor 633

Colocalize with
Image J Plugin
"Colocalization Threshold"

Figure 11. Image pre-processing for co-localization analyses

TPLSM Imaging System

- Langendorff-perfused heart on the stage of a 2-photon laser scanning microscope
- Perfuse with Tyrode's, and cytochalasin D (to facilitate E-C uncoupling)

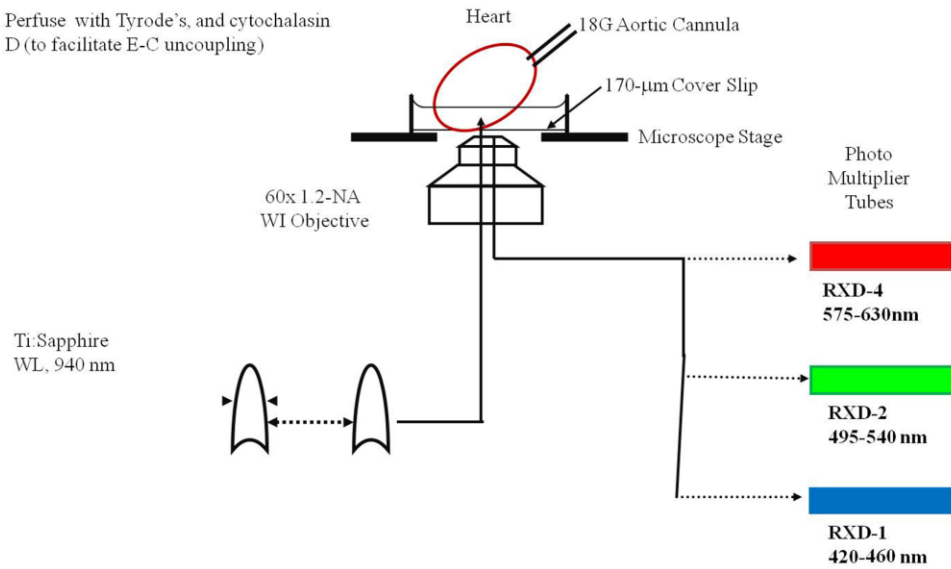


Figure 12. Two-photon laser scanning microscope

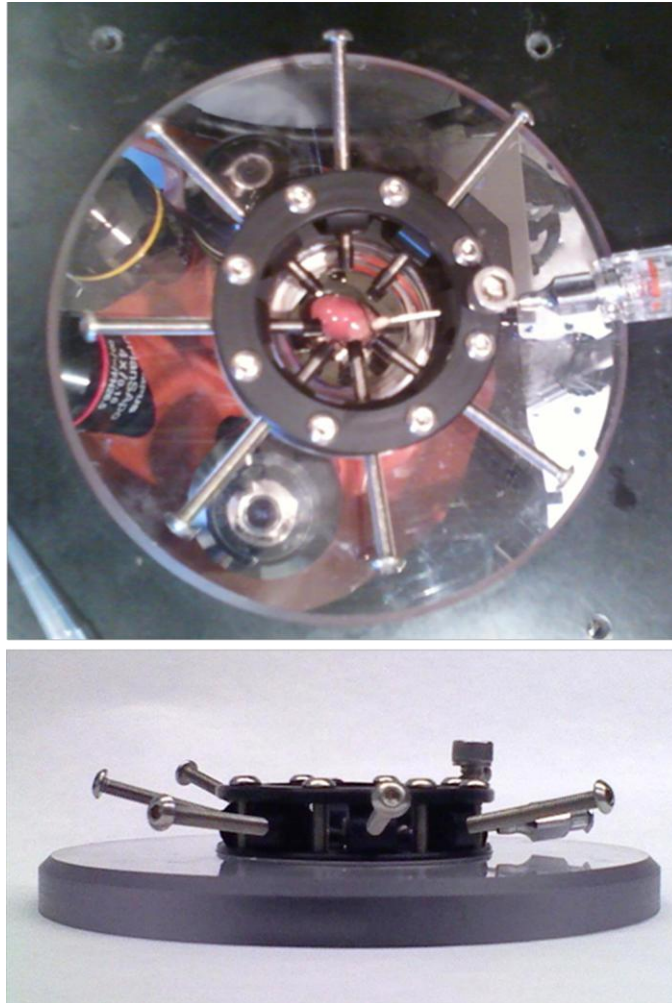
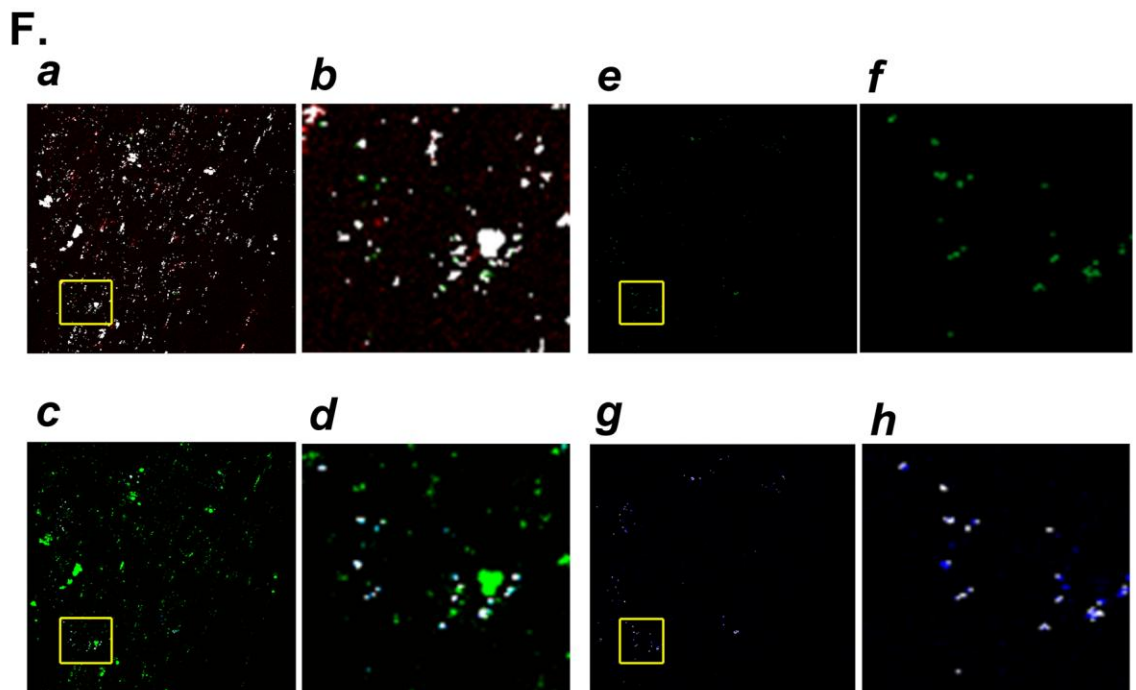
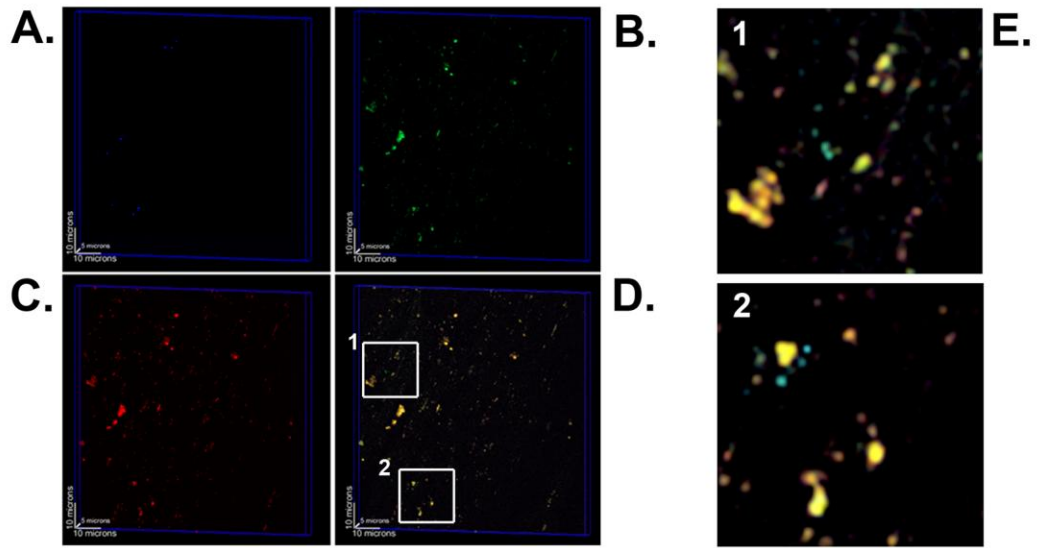


Figure 13. Heart perfusion chamber used for TPLSM imaging
Top and side aspect of the heart perfusion chamber used for TPLSM imaging.



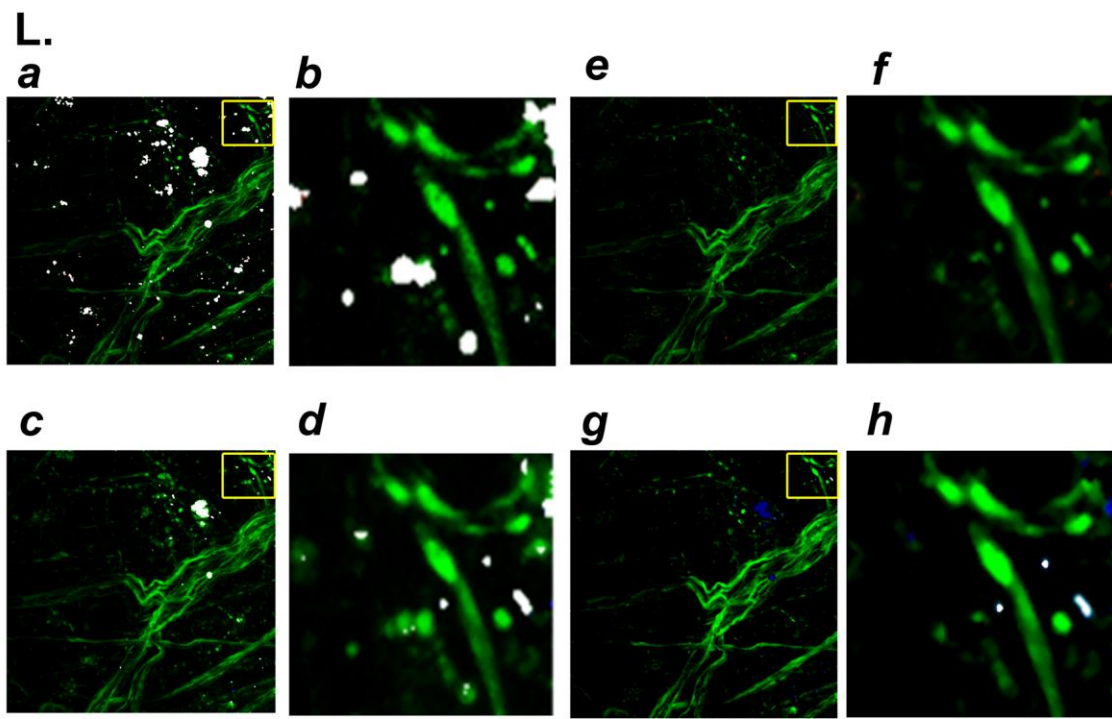
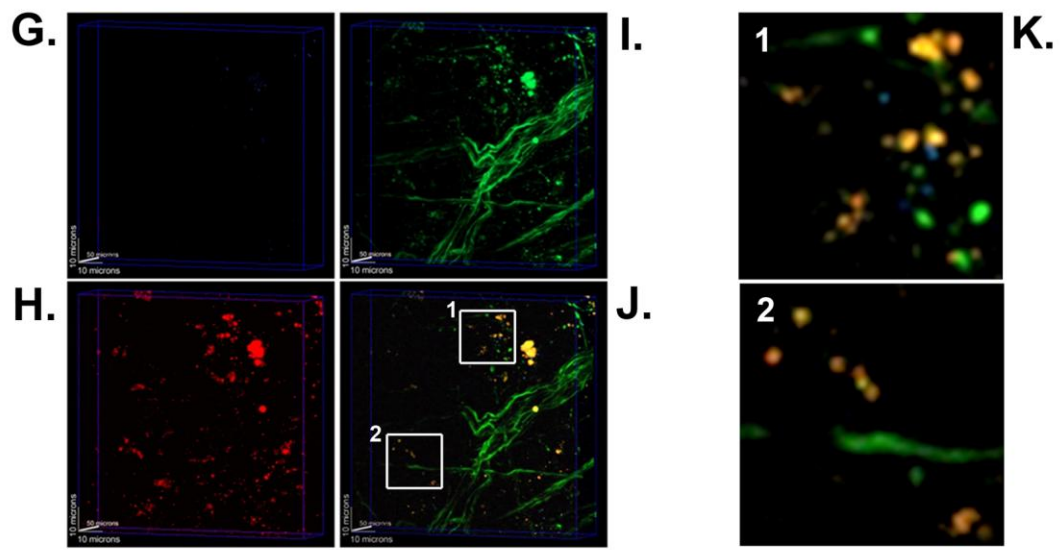


Figure 14. Two-photon excitation-induced tissue autofluorescence and EGFP fluorescence

Two-photon excitation-induced tissue autofluorescence and EGFP fluorescence exhibit distinct emission spectra in Langendorff-perfused mouse heart. **A-C** and **G-I**, 3D renderings of z-stacks taken from $53 \times 53 \times 15 \mu\text{m}^3$ segments within the left ventricular epicardium of a wild-type (A-C) and a transgenic hD β H-EGFP heart (G-I) during two-photon illumination with pulsed 940 nm laser light. Signals recorded in the blue (420-460 nm; A and G), green (495-540 nm; B and H) and red (575-630 nm; C and I) channel. The three-channel merged image stacks are shown in D and J. White denotes co-localization. E and K, magnified views of the boxed regions in D and J. F and L, Co-localization maps between maximum intensity xy projections of the green and red channel (a), and the green and blue channel (c). Images shown in (Fe) and (Le) were obtained by removing all pixels containing a red component from the green channel images. Images shown in (Fg) and (Lg) represent the co-localization maps between the subtracted green channel images and their corresponding blue channel images. Images in (b), (d), (f) and (h) represent magnified views of the boxed regions in (a), (c), (e) and (g), respectively.

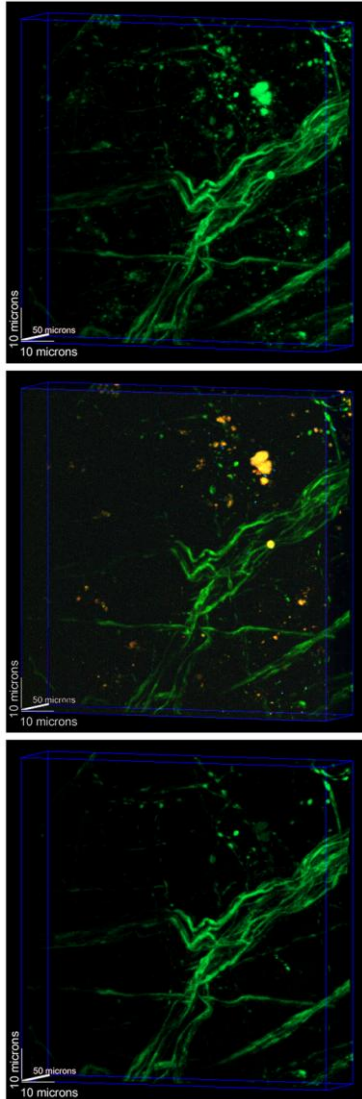


Figure 15. Removal of tissue autofluorescence

Removal of autofluorescence in a TPLSM z-stack from an hD β H-EGFP heart. Volume rendering of the same three-channel merged z-stack shown in Figure 14J following removal of autofluorescence.

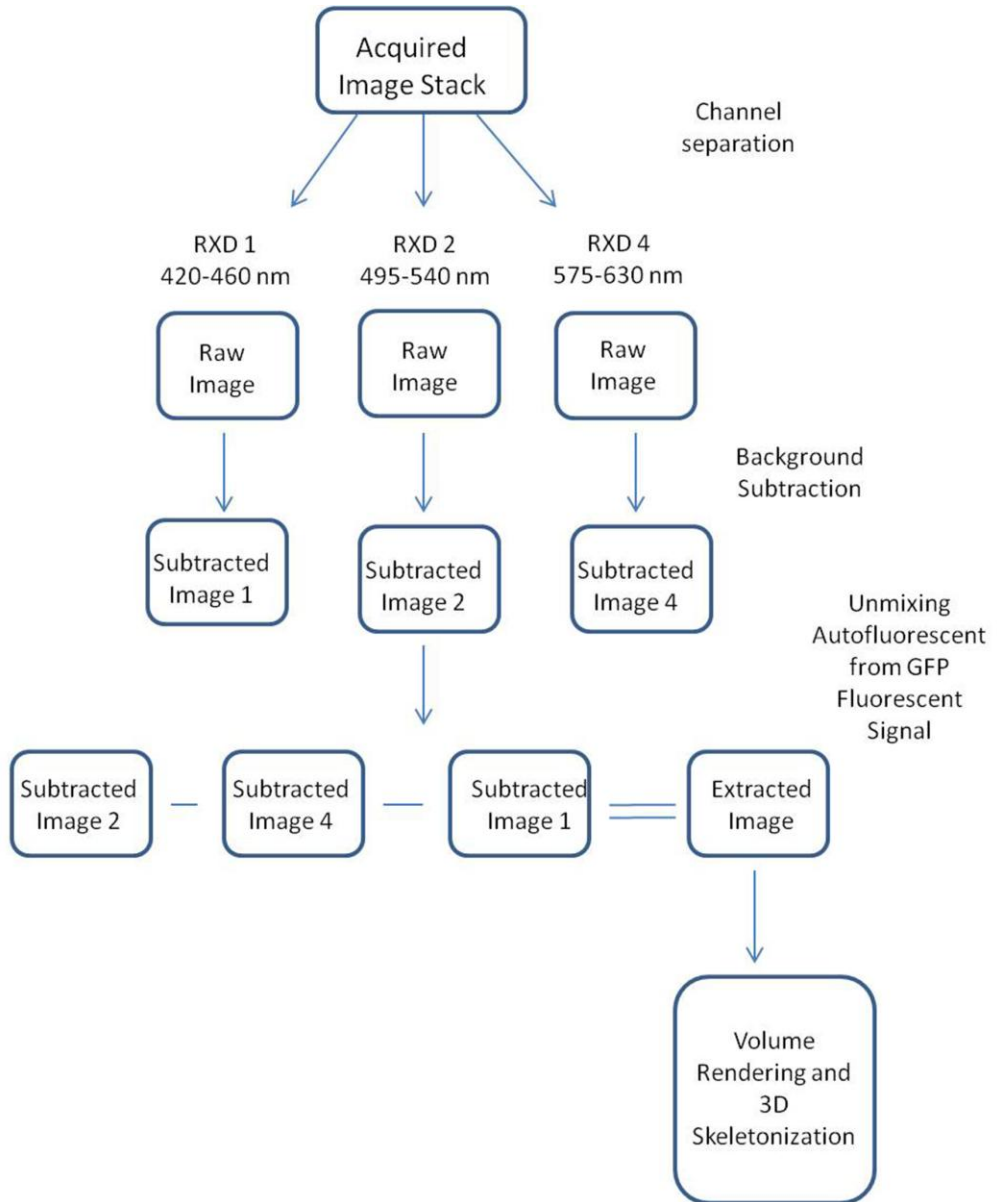


Figure 16. Flow chart of image pre-processing steps for 3D neuron tracking

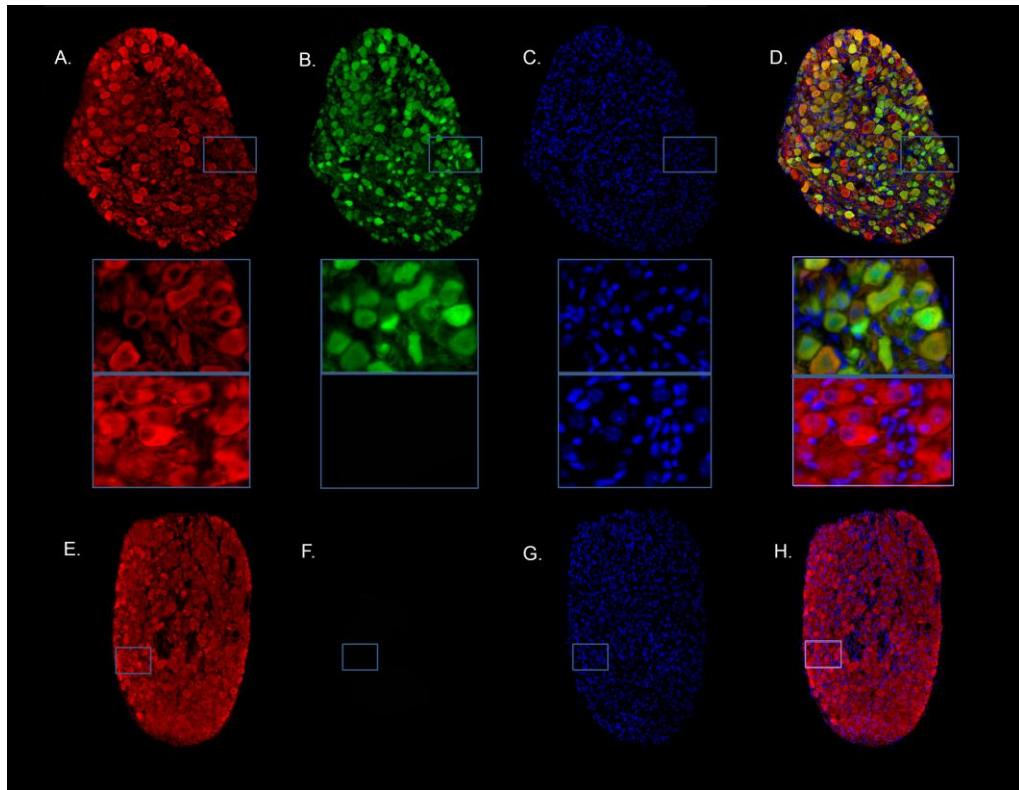


Figure 17. Expression of hD β H-EGFP in peripheral sympathetic neurons

A to D, Section through a transgenic stellate ganglion stained for anti-TH (red) and anti-GFP (green) immunoreactivity, and counterstained with nuclear Hoechst (blue). A three-channel merged image is shown in D. TH-expressing cells, i.e. sympathetic neurons, exhibit cytoplasmic and nuclear anti-GFP immunofluorescence, whereas EGFP-negative cells only show nuclear counterstaining. **E to H**, Section through a control stellate ganglion stained as in the transgenic ganglion, showing TH-expressing and non-expressing cells.

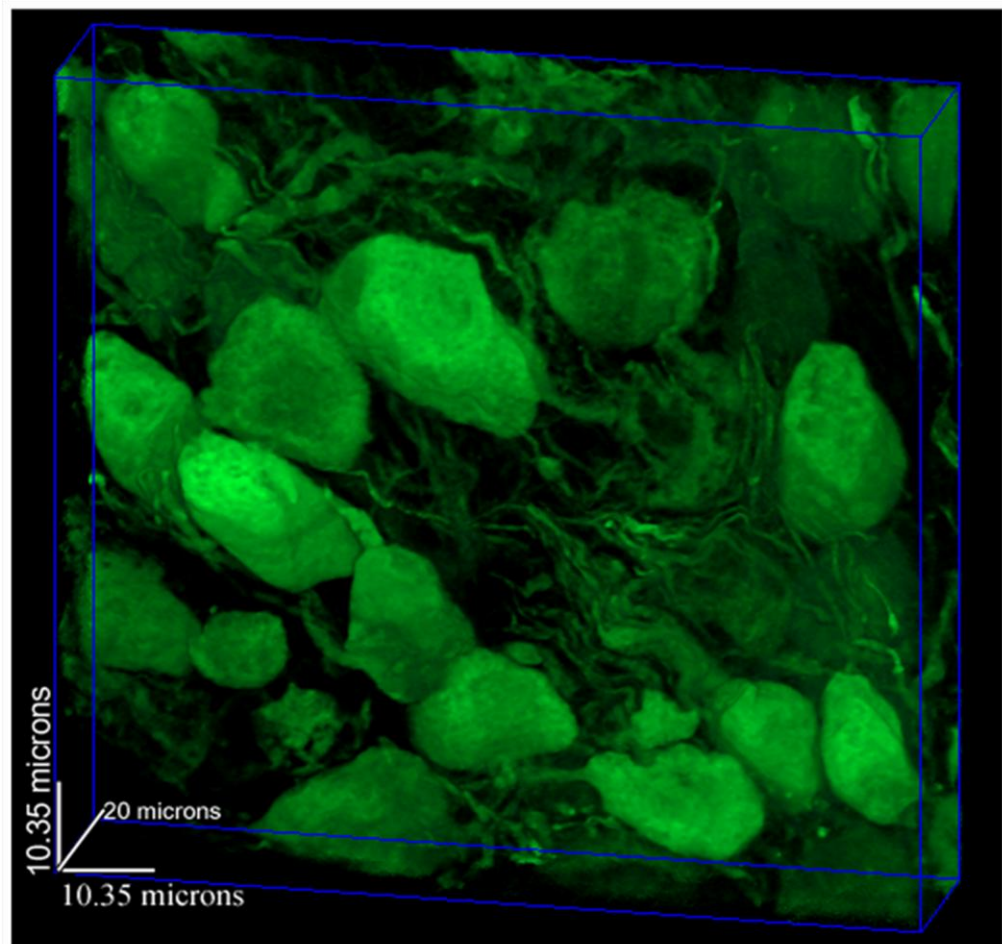


Figure 18. *EGFP expression in the soma and proximal dendrites of postganglionic sympathetic neurons*

A confocal z-stack was obtained from a 20 μm thick section of an adult hD β H-EGFP stellate ganglion stained with an anti-GFP primary antibody followed by a FITC-conjugated secondary antibody and rendered in three dimensions. Note appearance of anti-GFP immunoreactivity in nuclei, cytoplasm and proximal dendrites of transgenic neurons.

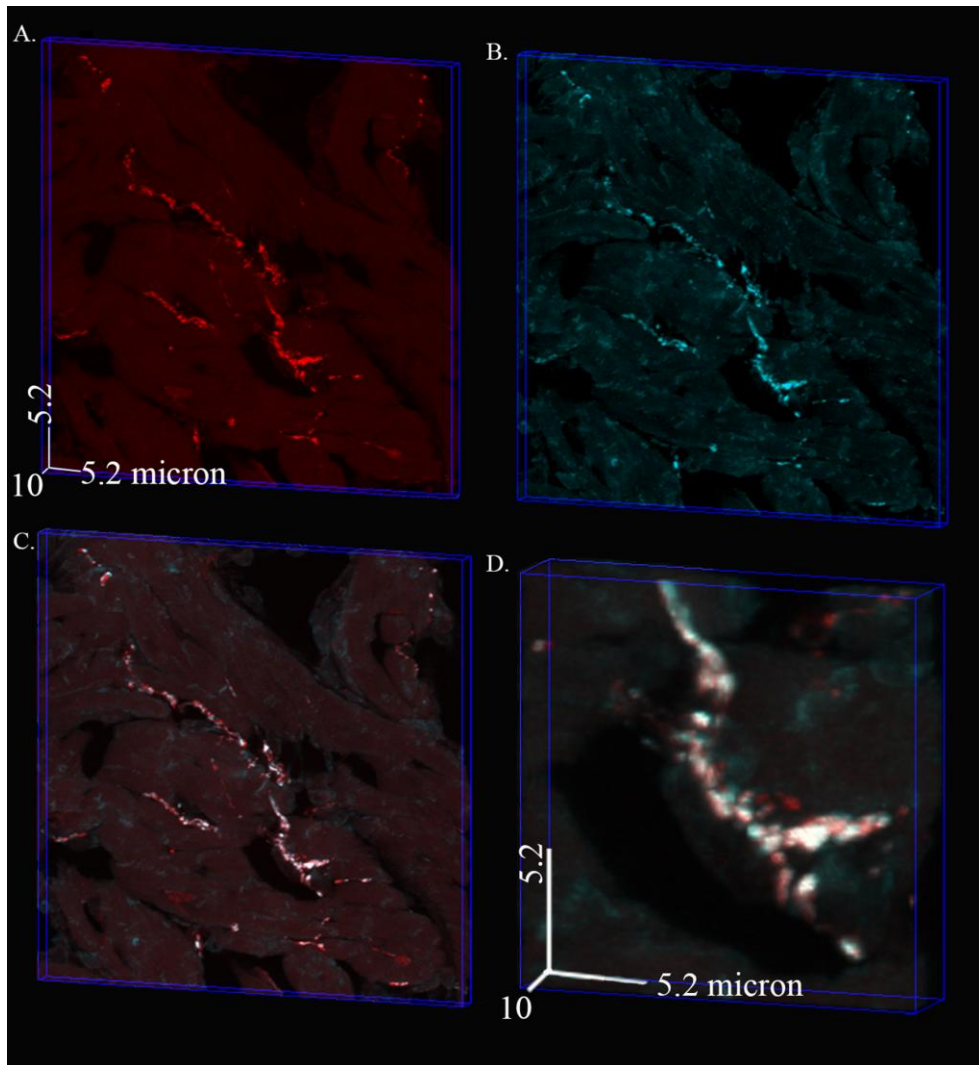


Figure 19. EGFP is expressed in intracardiac portions of postganglionic sympathetic neurons

A 10 μm thick section from an adult hD β H-EGFP heart was dually stained with an anti-TH and an anti-GFP antibody, followed by incubation with Alexa546- and Alexa633-conjugated secondary antibodies, and subjected to confocal microscopy. **A** and **B**, 3D renderings showing a myocardial segment (size, in μm : 0.1 x 0.1 x 0.3) labeled with antibodies against GFP (A) and TH (B). **C**, Two-channel merged image. **D**, Zoom-in view of the boxed region in C. If the pixel is white, then both proteins occupy that pixel.

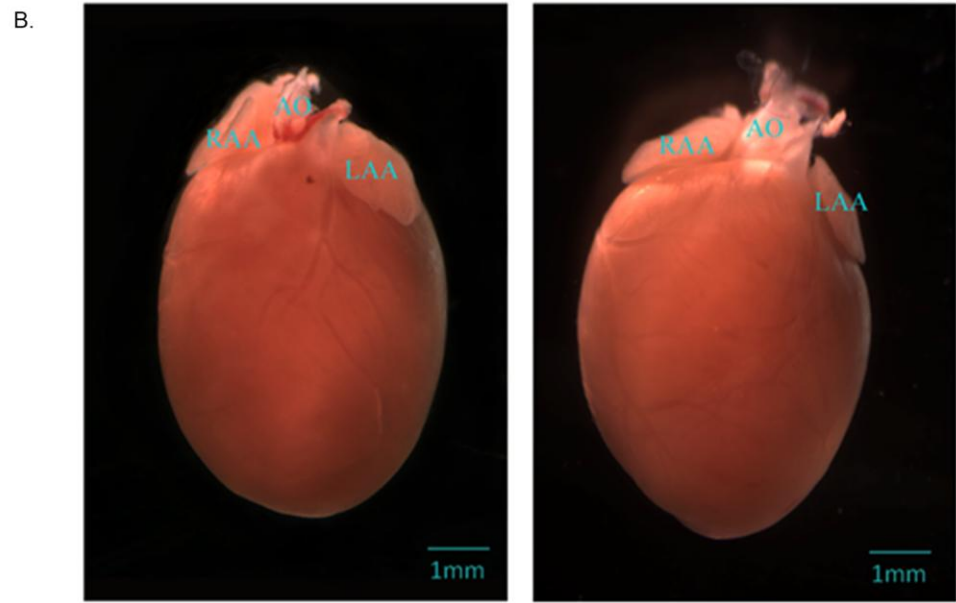
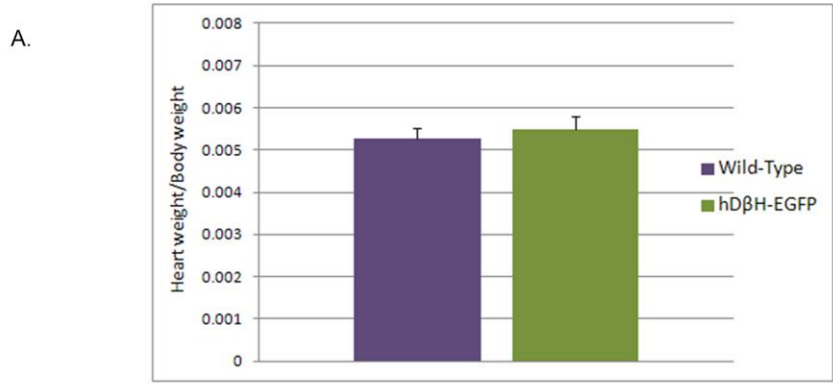


Figure 20. Adult transgenic hD β H-EGFP hearts are structurally normal

A, Mean \pm SEM heart weight/body weight ratio in transgenic versus non-transgenic mice between 12 and 38 weeks of age. Values are from 10 mice per genotype. $P > 0.05$ by t-test. **B**, Photographs of a non-transgenic (left) and a transgenic heart. LAA = left atrial appendage; AO = aorta. **C**, Micrographs of longitudinal sections through a non-transgenic and transgenic heart. H & E stain. RA = right atrium, LA = left atrium, LV = left ventricle.

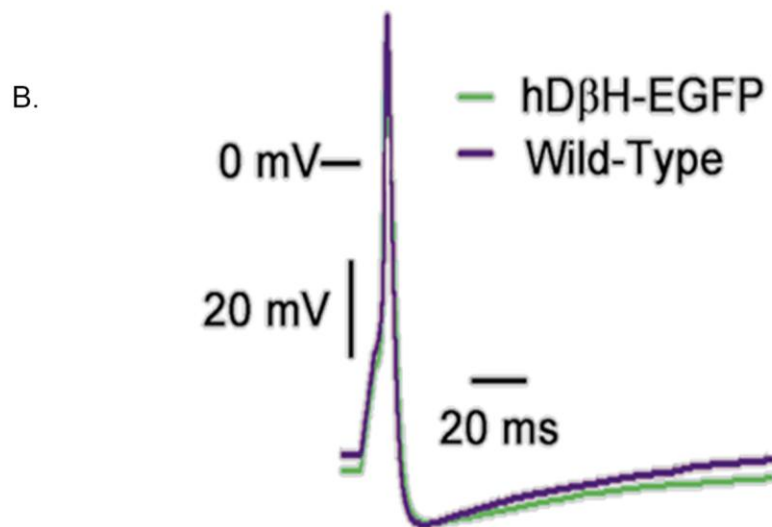
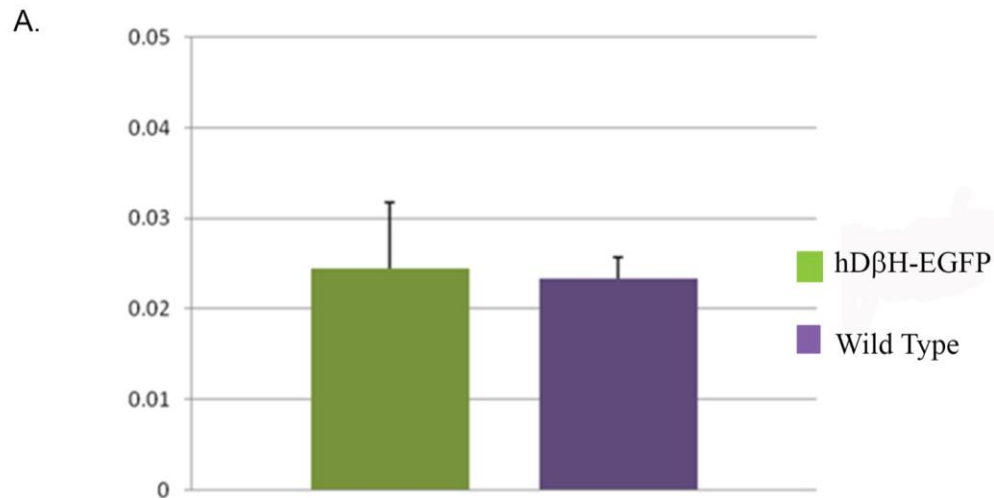
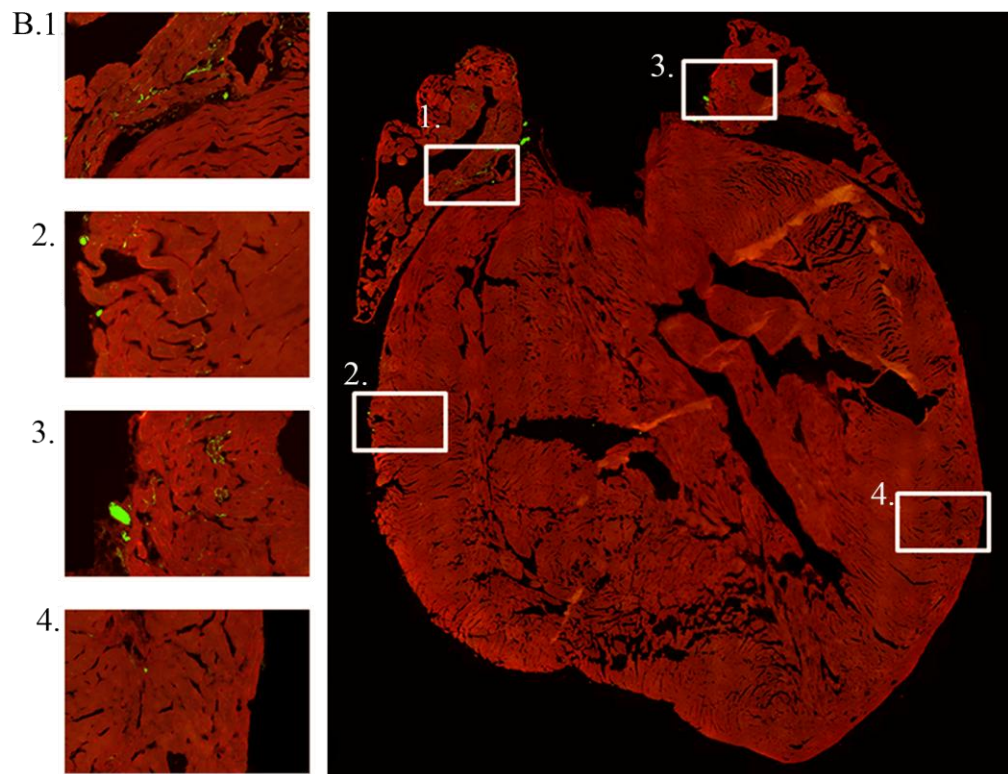
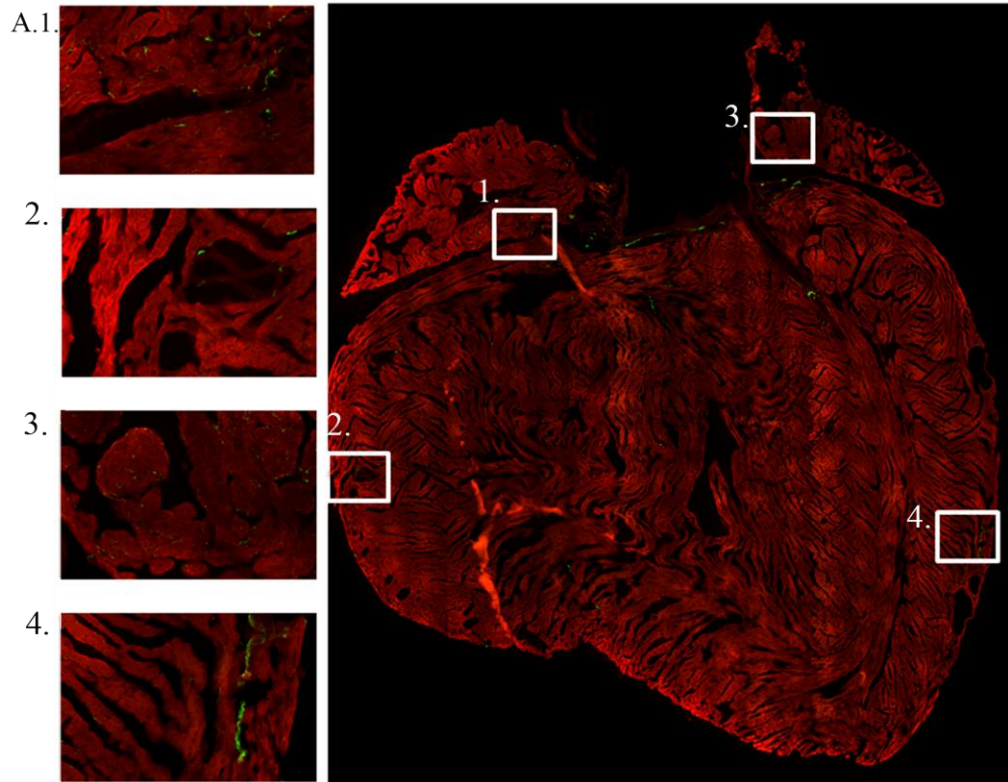


Figure 21. *Prolonged EGFP expression does not alter neuron density in peripheral sympathetic ganglia or their electrical properties*

A, Mean \pm SEM density of neurons in peripheral sympathetic ganglia. Values are from 6 midsections per genotype distributed among three mice per genotype (one each from the cervical and stellate ganglion per mouse). $P > 0.05$ by t-test. **B**, Representative transmembrane action potentials in a non-transgenic and transgenic neuron.



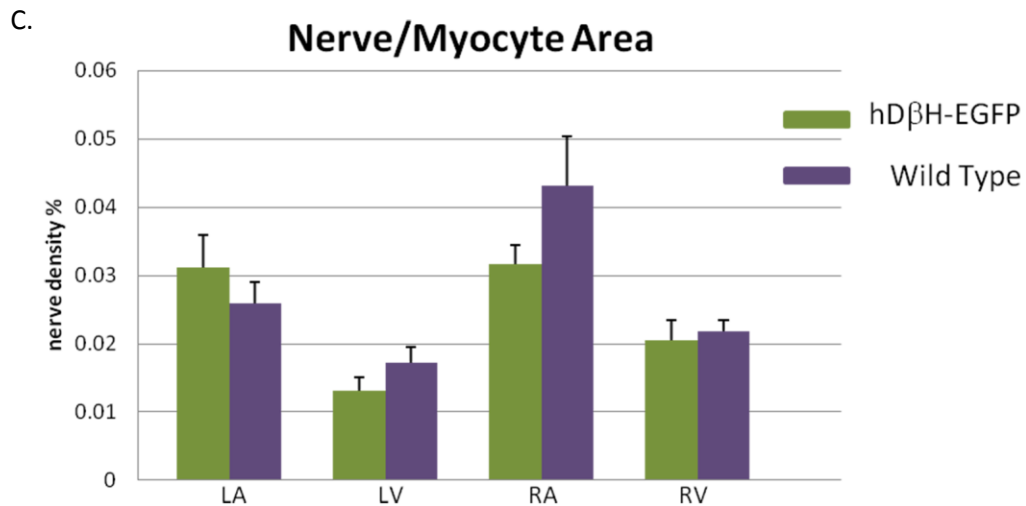


Figure 22. Adult transgenic hearts have normal sympathetic innervation density

A and **B**, Fluorescence micrographs of sections from a non-transgenic (A) and transgenic heart (B) double immunostained with antibodies against TH (green) and α -actinin (red). Numbered left panels show zoom-in views of the correspondingly numbered boxed regions in the right panels. **C**, Bar graphs of mean \pm SEM sympathetic nerve density in different regions of control and transgenic hearts. Values are from eighty $410 \times 250 \mu\text{m}^2$ images per genotype (5 images each from 4 regions per heart). LA = left atrium, LV = left ventricle, RA = right atrium, RV = right ventricle. $P > 0.05$ for comparisons between genotypes by t-test.

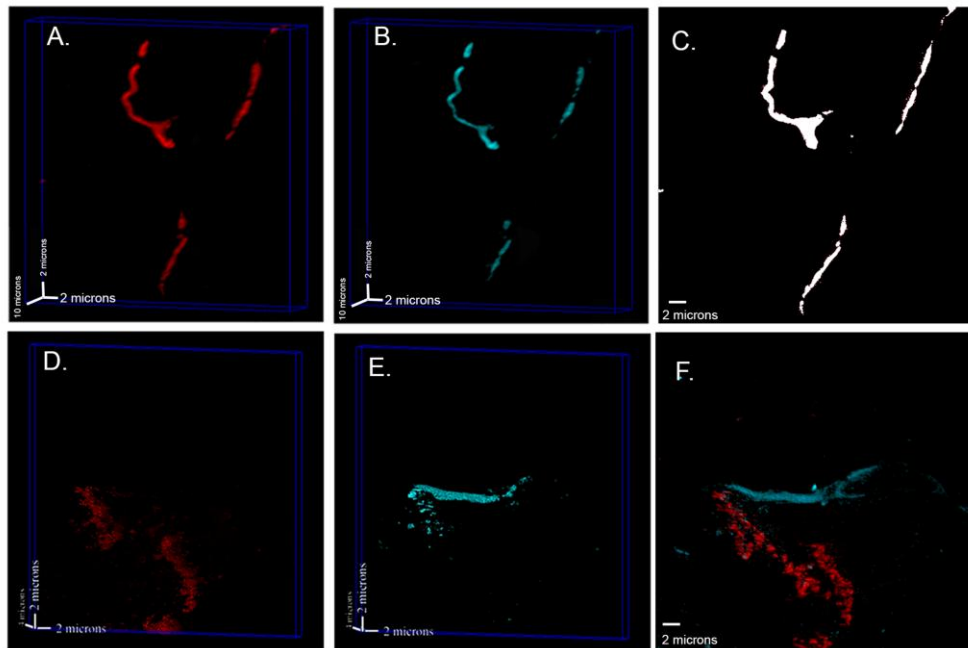


Figure 23. Determination of the empirical upper and lower limits of co-localization

A and **B**, Pair of volume-rendered confocal z-stacks obtained from a cardiac section incubated with a tyrosine hydroxylase primary antibody and two secondary antibodies labeled with Alexa546 (A) or Alexa633 (B). The x, y and z dimensions of the imaged volume were 52.7, 52.7 and 10 μm , respectively. **C**, Co-localization map of the maximum intensity xy projection of the merged two-channel z-stack. If the pixel is white, then both fluorophores occupy that pixel. **D** and **E**, Pair of volume-rendered confocal z-stacks obtained from a cardiac section reacted with primary antibodies against Cx43 and tyrosine hydroxylase, followed by secondary antibodies conjugated with Alexa546 (D) and Alexa633 (E). **F**, Co-localization map of the maximum intensity xy projection of the two-channel merged z-stack.

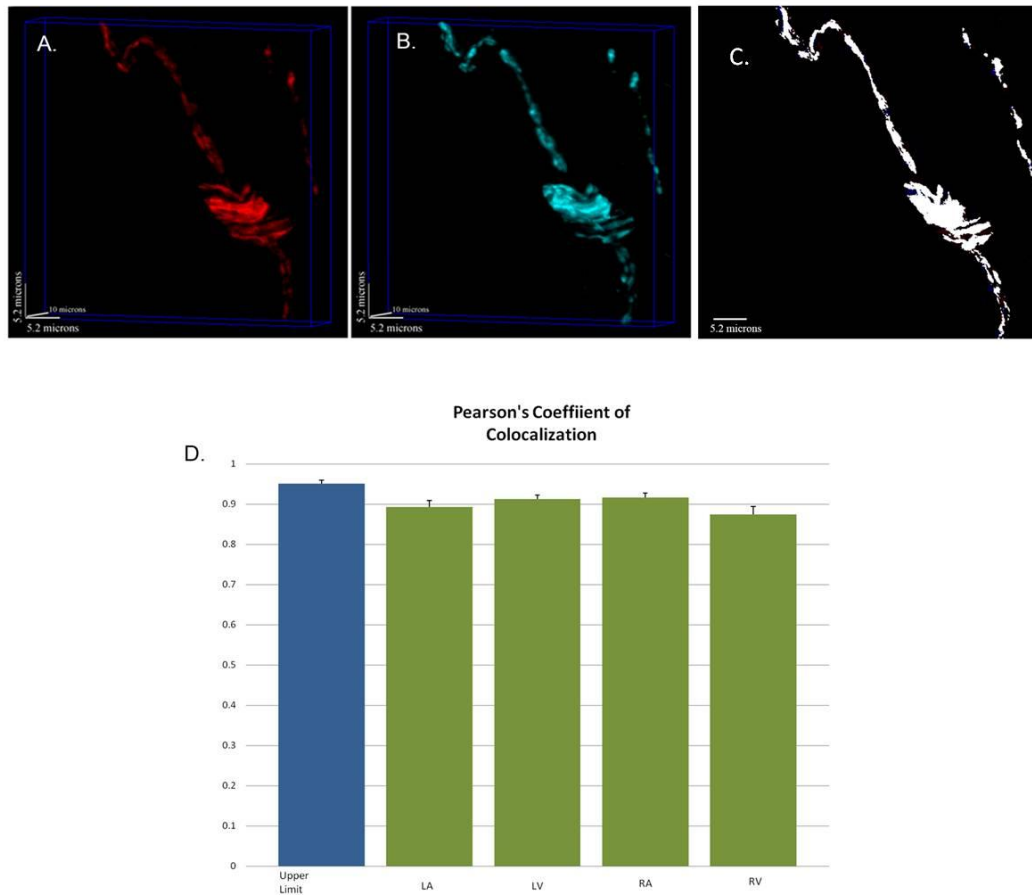


Figure 24. *Intracardiac distribution of EGFP tracks sympathetic nerves*

A, Pair of volume-rendered confocal z-stacks obtained from a cardiac section ($52.7 \times 52.7 \times 10 \mu\text{m}^3$) co-stained with tyrosine hydroxylase (**A**; Alexa546 label) and GFP (**B**; Alexa633 label) antibodies.

C, Co-localization map of the maximum intensity xy projection of the merged stack. If the pixel is white, both proteins occupy that pixel.

D, Bar graphs of mean \pm SEM Pearson's co-localization coefficients for the right ventricle (RV), right atrium (RA), left atrium (LA), and left ventricle (LV).

Values are from 15 image stacks each per region equally distributed among 3 hearts. There was no significant difference between the regions or between each region and the empirical upper limit ($P > 0.05$ by ANOVA and Dunn's *post hoc* analyses). Only the value for the RV was significantly smaller than the empirical upper limit ($P < 0.05$).

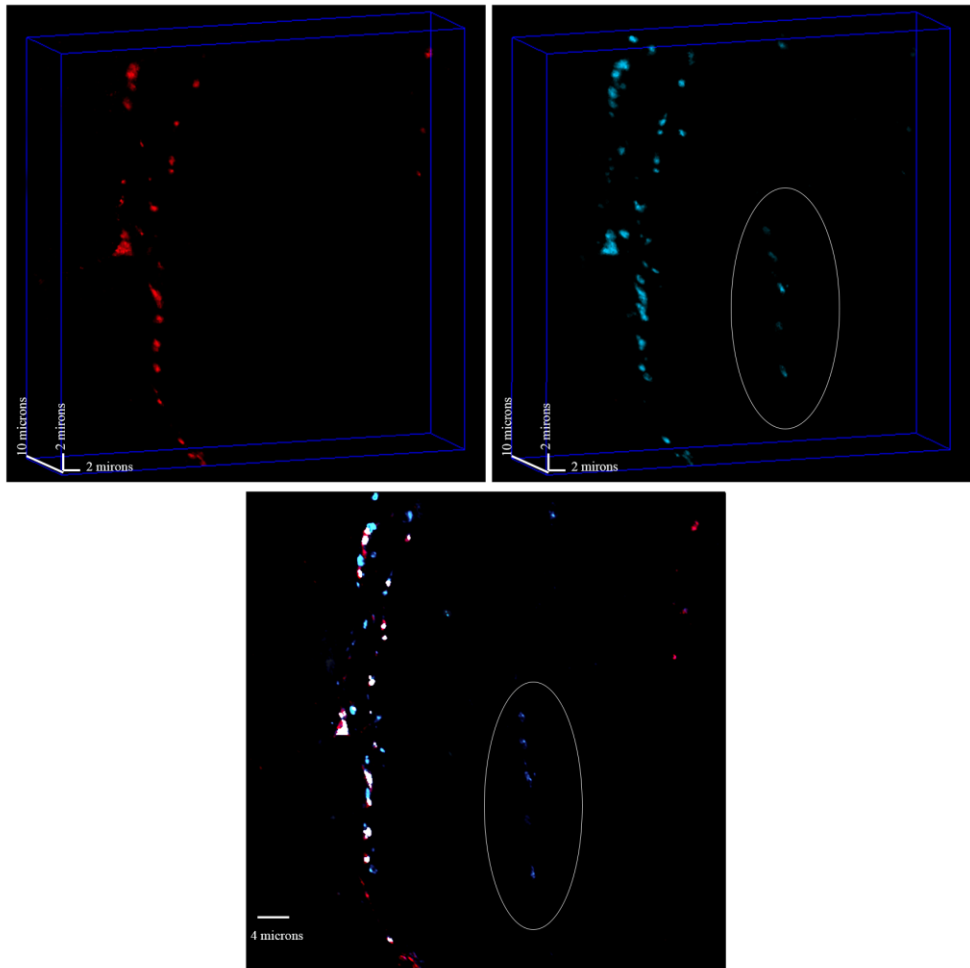
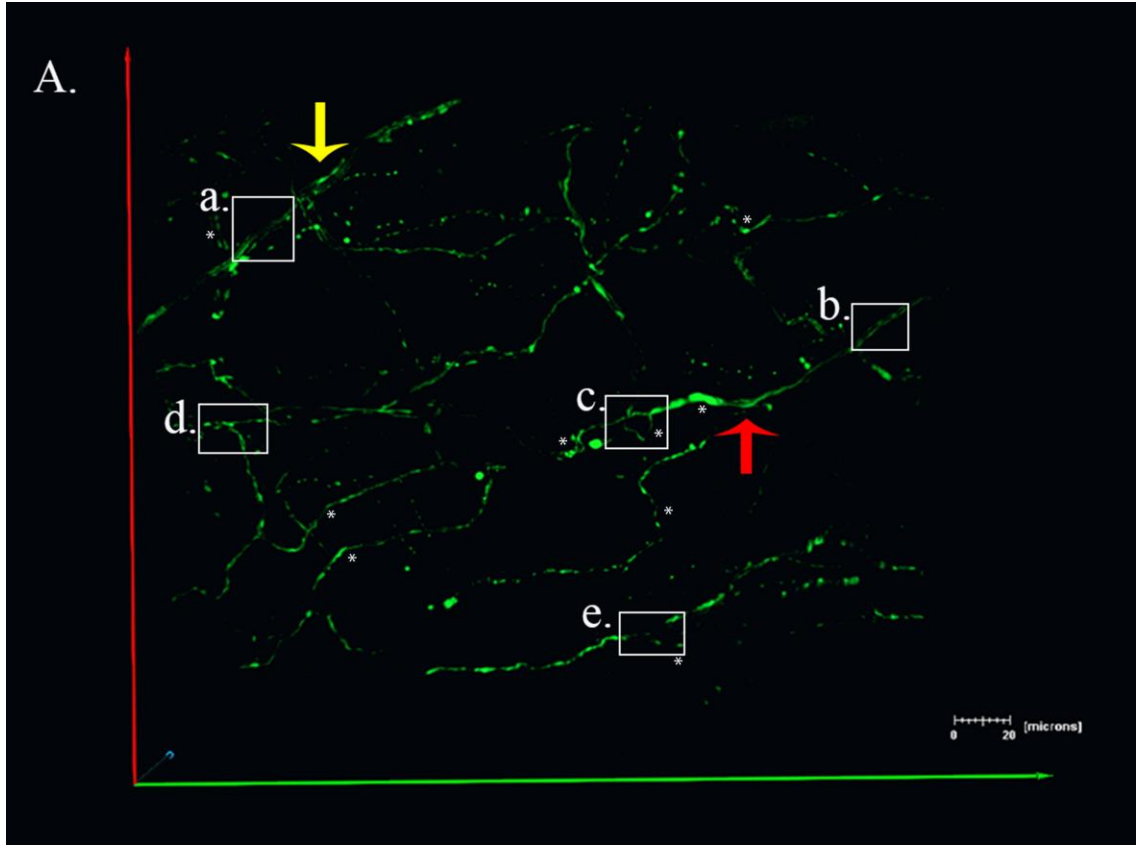
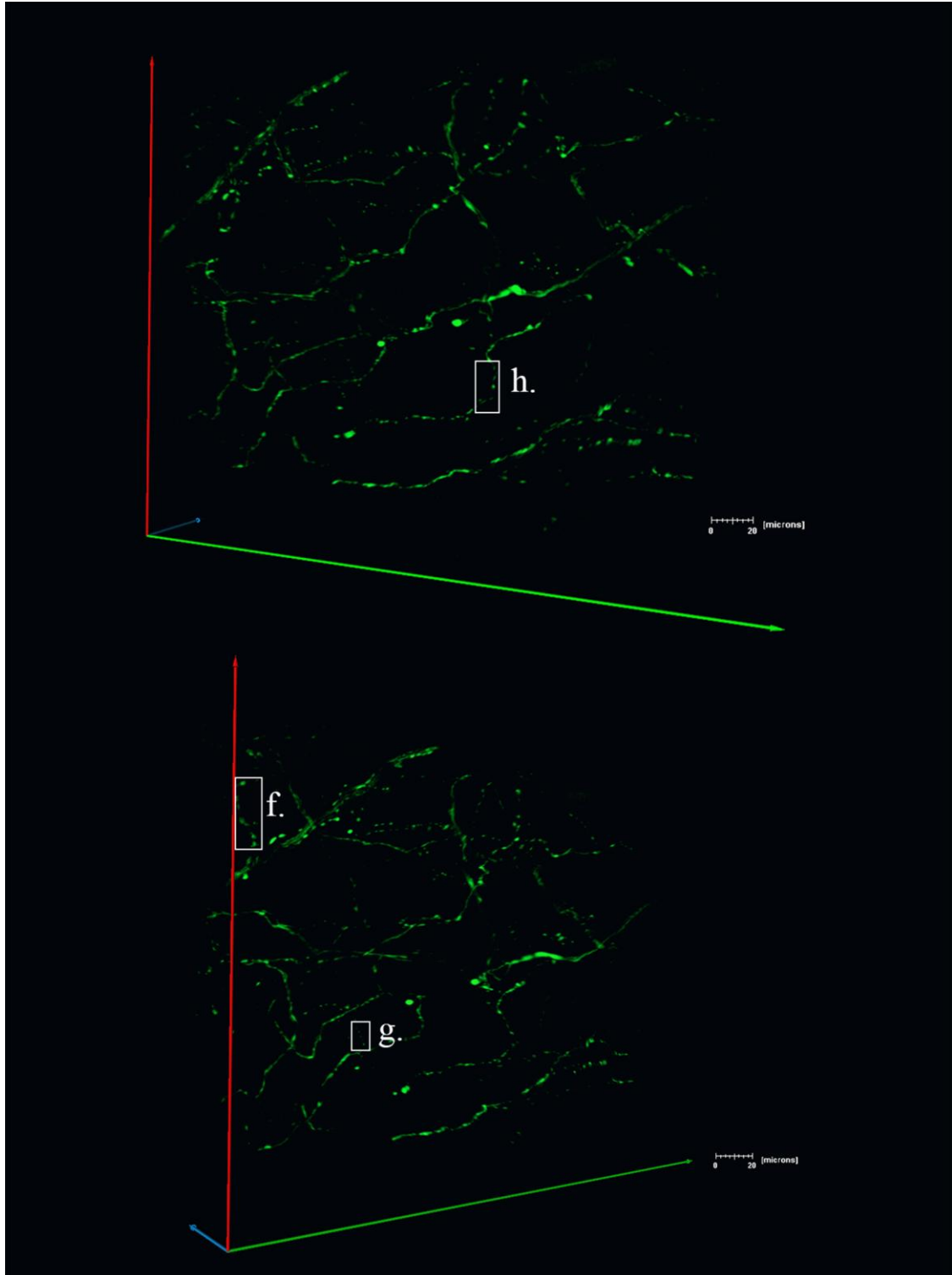
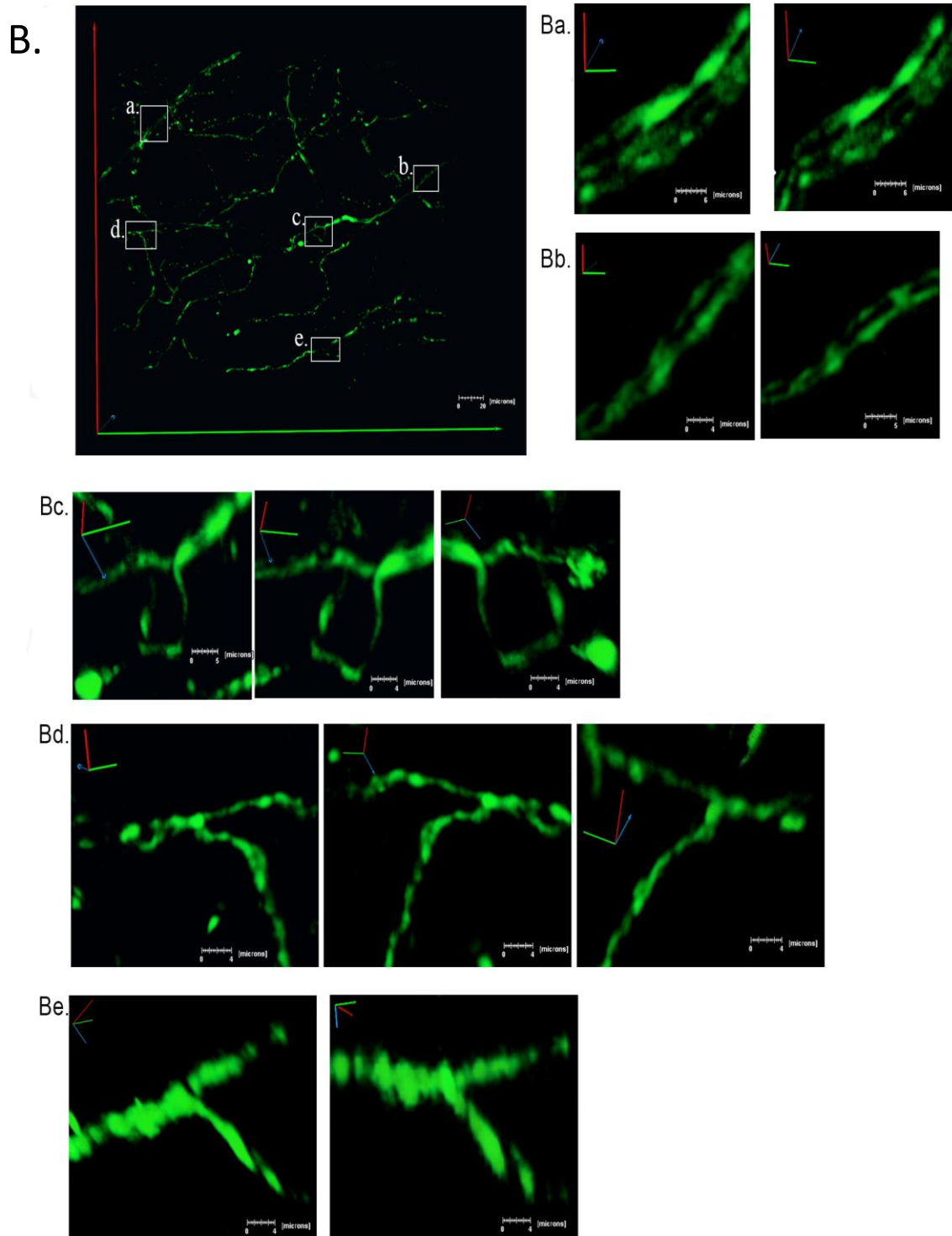
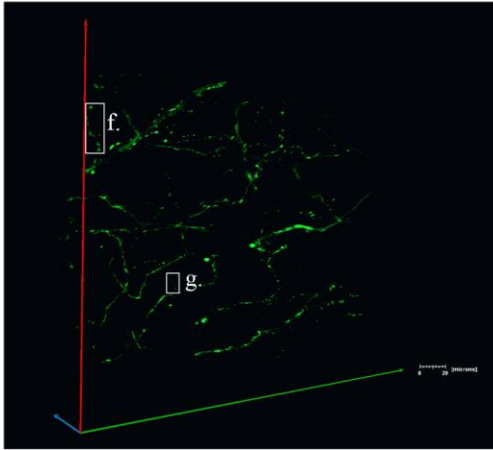


Figure 25. Rare example of an intracardiac TH-expressing nerve not expressing EGFP

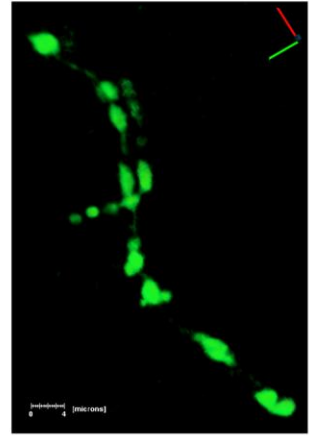
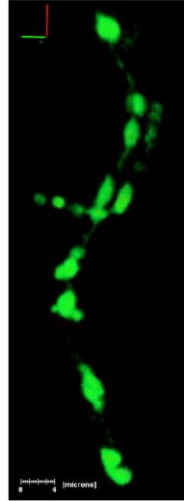




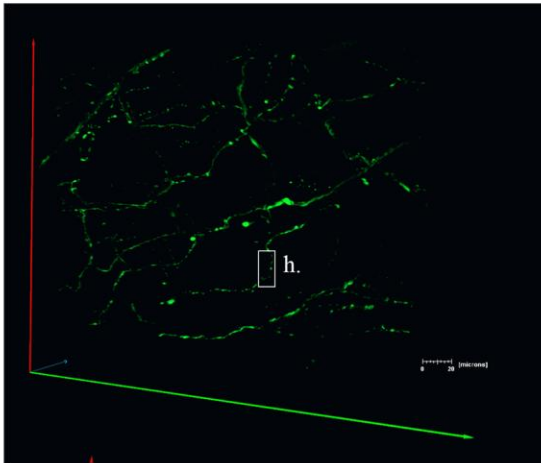
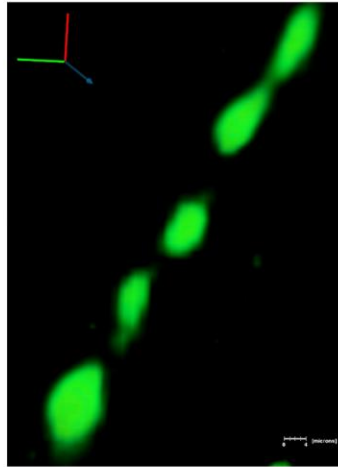




Bf.



Bg.



Bh.

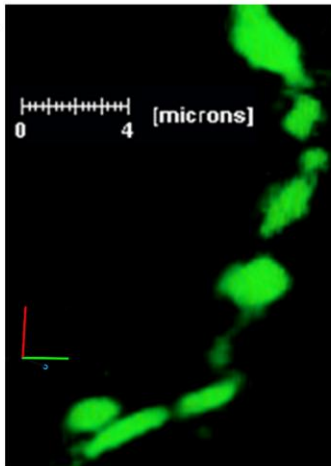


Figure 26. Three-dimensional reconstruction of the sympathetic neurite network within a portion of the outermost left ventricular epicardial layer in a living, adult hDβH-EGFP heart

A, 3D rendering of the subepicardial sympathetic arbor from three different view angles. All sympathetic axons (labeled with EGFP) in a 230 μm by 280 μm by 50 μm segment were imaged by TPLSM. A montage of 9 (3 x 3) overlapping image stacks provided the dataset for reconstruction. Images (512 x 512) were collected at a voxel size of 0.2 μm x 0.2 μm x 0.5 μm with 16-bit resolution. **B**, Magnified views of the boxed regions labeled a through j in (A). Ba and Bb, three- (Ba) and two-axon bundle (Bb) on the epicardial surface; Bc, branching of an axon while its constituent two axons did not branch; Bd – Bg, binary (Bd and Be) and tertiary (Bf) axonal branching; Bg and Bh, intramyocardial axonal segments with boutons. Small letters refer to the correspondingly labeled boxed regions in (A).

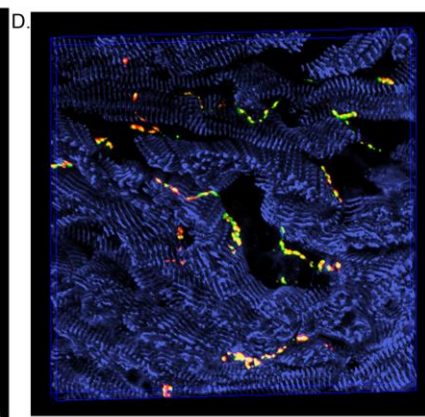
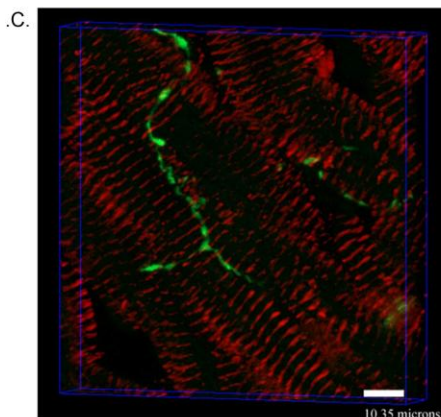
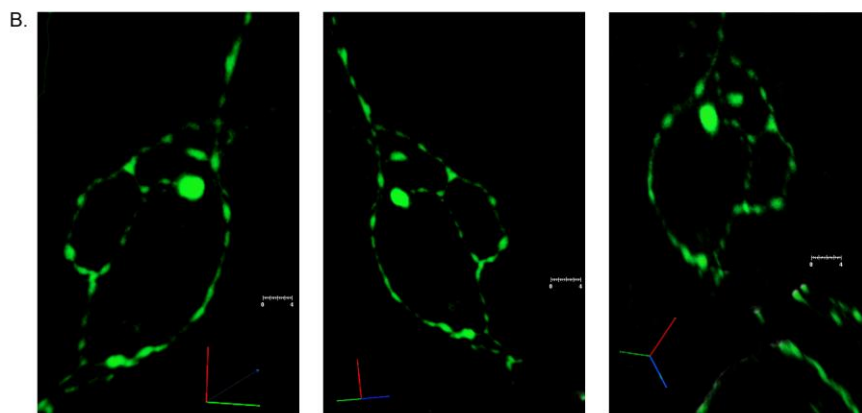
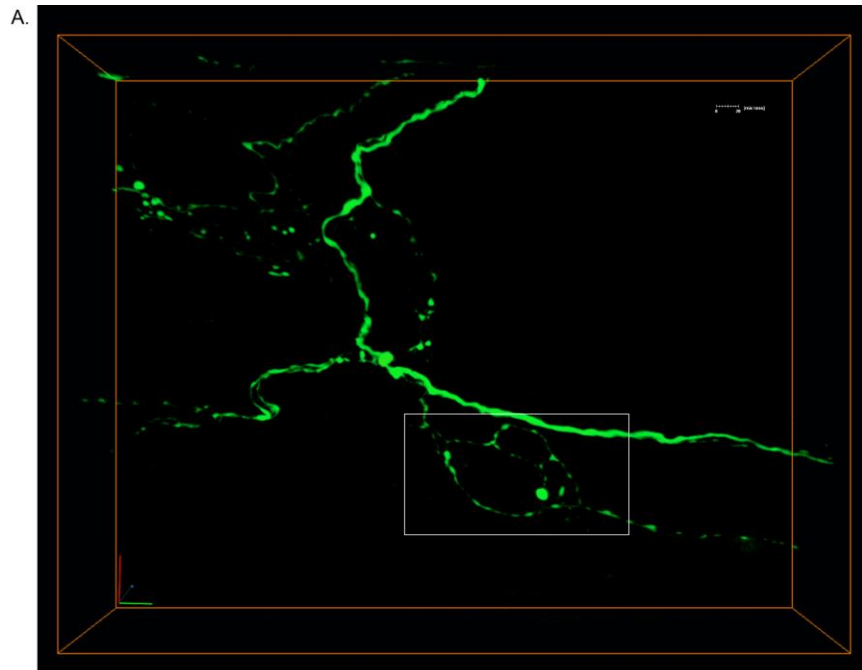
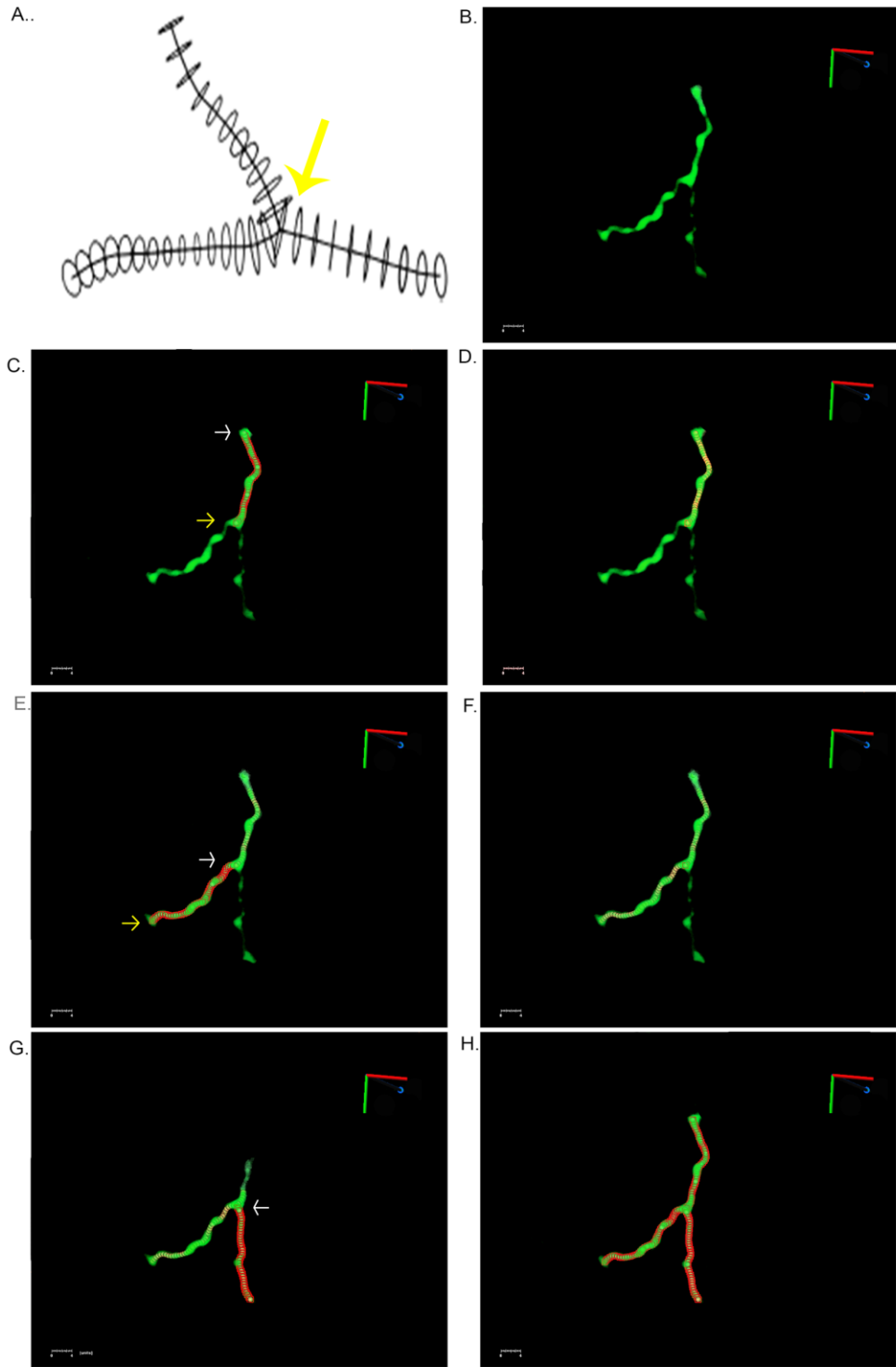


Figure 27. Similar morphology of intramural sympathetic neurites in living and fixed cardiac tissue

A, 3D reconstruction of a branching sympathetic axon in the outermost left ventricular epicardial layer of a Langendorff-perfused hD β H-EGFP heart. All EGFP-expressing axons in a 130 μ m by 165 μ m by 40 μ m segment were imaged by TPLSM. The montage of 7 overlapping image stacks provided the data set for reconstruction. **B**, Magnified views of the boxed region in A. **C**, Volume rendering of a confocal image stack that was acquired from a 10 μ m thick cardiac section double immunostained for tyrosine hydroxylase (green) and the cardiomyocyte marker α -actinin (red). **D**, Volume rendering of a confocal image stack obtained from a 10 μ m thick cardiac section triple immunostained for tyrosine hydroxylase (red), synapsin I (green), and sarcomeric α -actinin (cyan). Yellow fluorescent regions, indicating co-localization of tyrosine hydroxylase and synapsin I, superimpose on axonal boutons, suggesting they constitute neurotransmitter release sites.



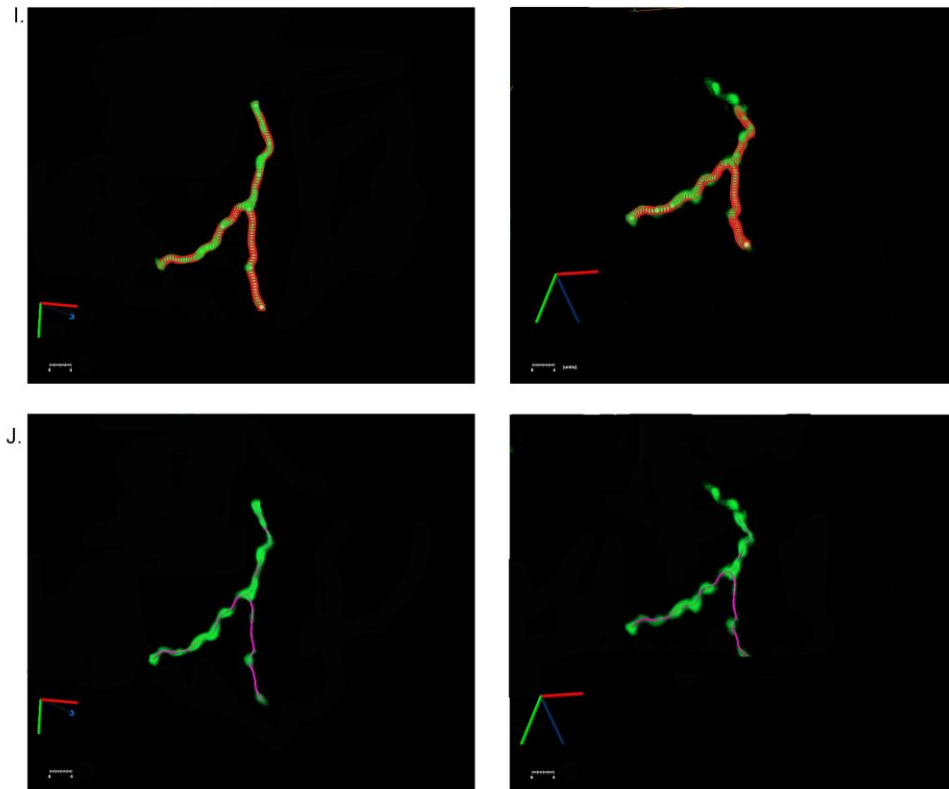


Figure 28: *Method for semi-automated 3D skeletonization of axonal arbors from two-photon imaging stacks*

A, Schematic 3D representation of a bifurcating axon by three tubes attached to each other at a branching point (arrow). The shape of an axonal segment is approximated by a discrete series of circular cylinders ('snaxels') of variable diameter and variable axis orientation. A fitting algorithm is used to determine values for each snaxel's axis and diameter that provide maximal congruency of the reconstructed segment with the image data^[82]. **B**, Volume rendering of a portion of a two-photon image stack obtained from a living hDβH-EGFP heart. **C**, Superimposition of preliminary snaxels (represented by red spheres of equal diameter) on the traced portion of the image data. White and yellow arrow denote start and end point, respectively, of the traced segment. **D**, Best-fit alignment of individual snaxels on the traced image data in C following application of the fitting algorithm. **E** and **F**, Extension of 3D tracing by adding a new

piece of skeleton to the preexisting segment. Preliminary snaxels are seeded between the start and end point (denoted by the white and yellow arrow, respectively) of the to-be-traced segment. Their 3D coordinates are subsequently adjusted to obtain maximal congruency of the reconstructed segment with the two-photon image data (F). **G** and **H**, Addition of a newly reconstructed branch to the rest of the skeleton using the seed-and-fit algorithm. Arrow in G denotes a branching point. **I**, Overlay of the 3D original image data and the 3D tracing, shown at two different view angles. **J**, Superimposition of the 3D original data onto the 3D midline skeleton. The magenta line was obtained by removing each snaxel's outer contour and subsequently connecting the center coordinates of all snaxels. The same view angles as in I are shown.

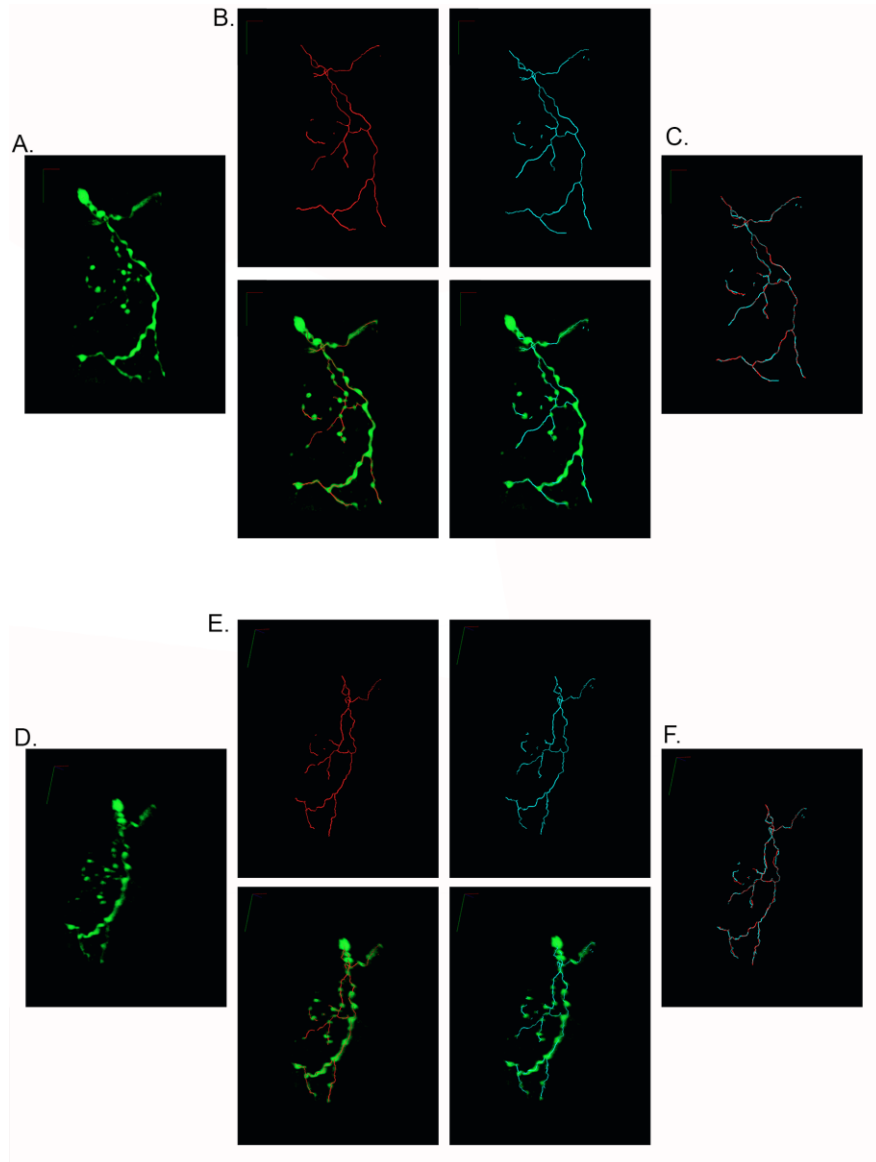


Figure 29. *User invariance of 3D neurite tracing*

A and **D**, Volume rendering of the EGFP-expressing sympathetic axon network in the left ventricular subepicardium of a live $h\beta H$ -EGFP heart. The same image stack is shown at two different view angles. View angles in **B** and **C** and view angles in **E** and **F** are identical to those in **A** and **D**, respectively. **B** and **E**, Upper rows: 3D midline skeletons by user 1 (red) and user 2 (cyan). Lower rows: overlays of the **D** original image data and each user's 3D skeleton. **C** and **F**, Superimposition of each user's 3D skeleton.

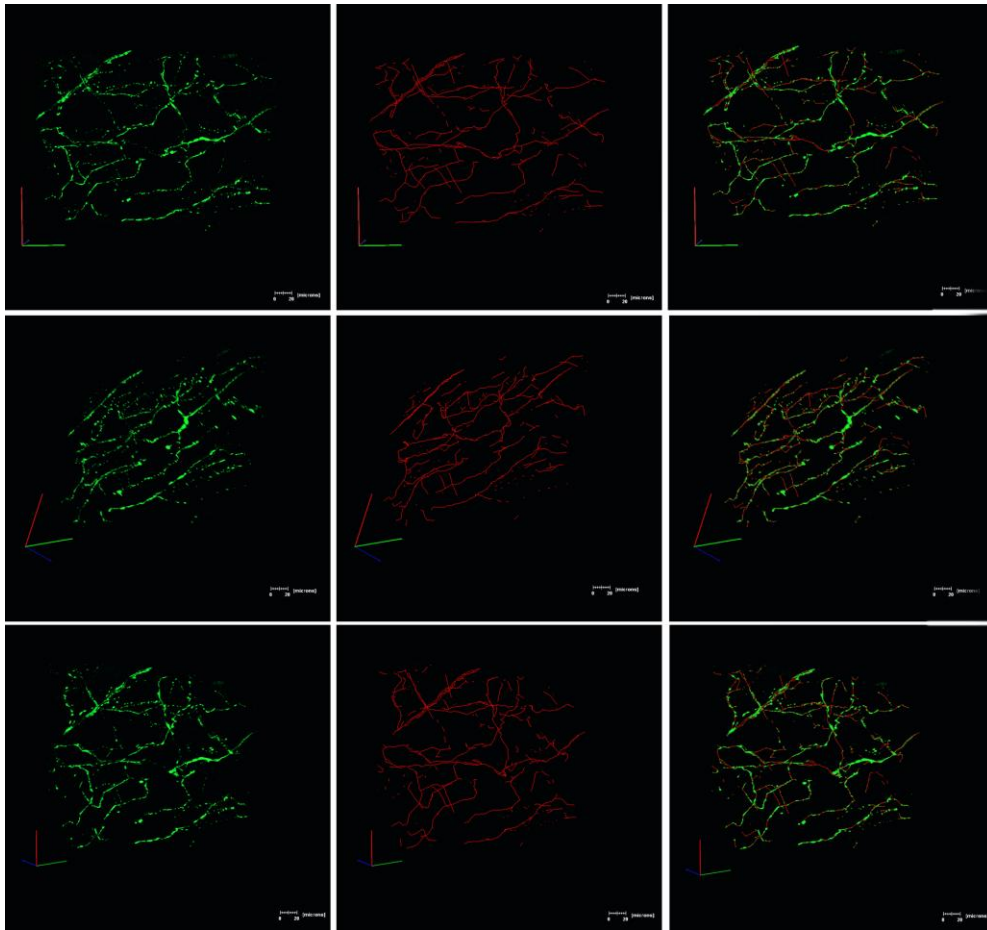
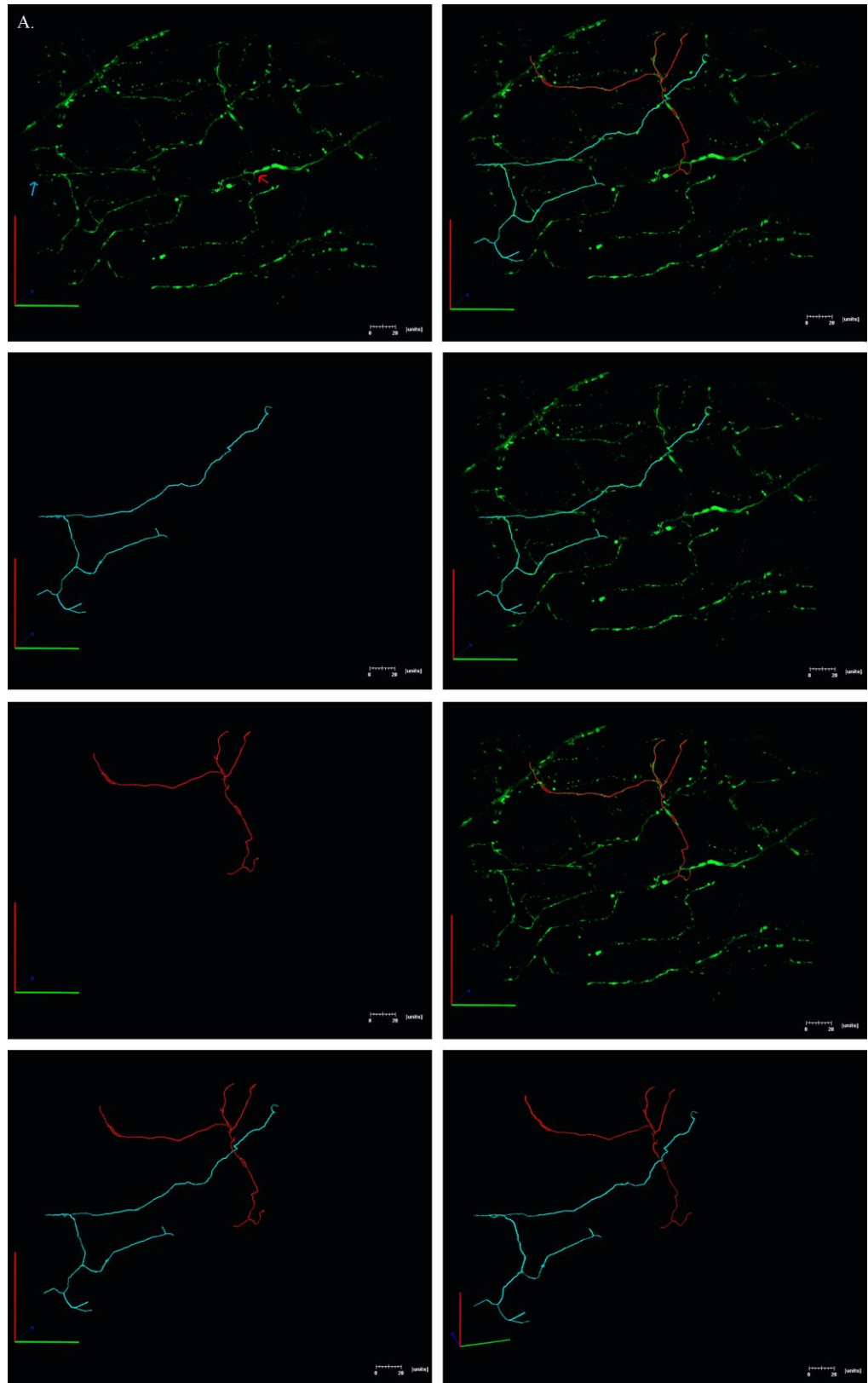
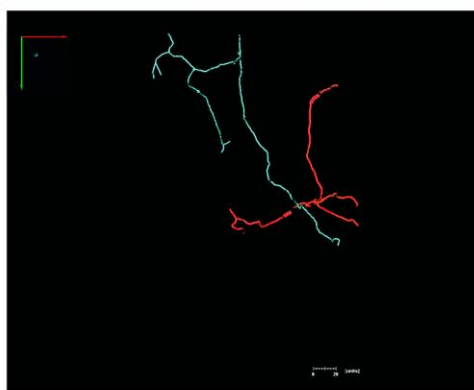
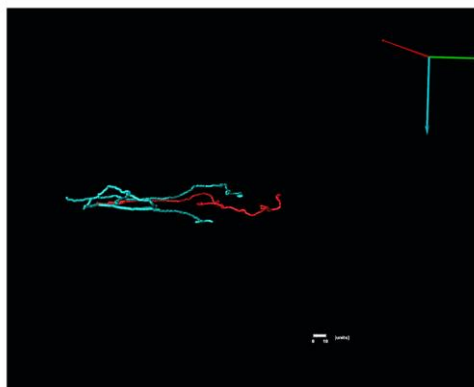
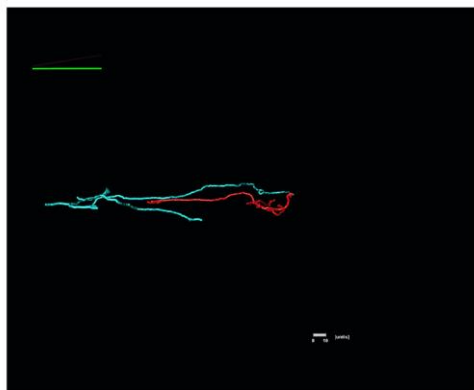
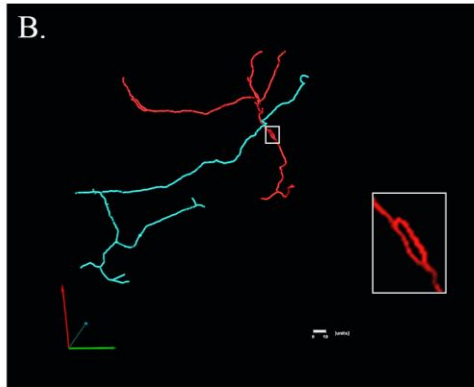


Figure 30. 3D rendering of skeletonized sympathetic arbors within a finite volume of the left ventricular subepicardium

A complete 3D skeleton of all green fluorescent neurites was generated using the semi-automated tracing algorithm and rendered in 3D. In each row, the left, middle and right panel show the 3D original imaging data, the 3D skeleton, and the overlay of the 3D original data and the 3D skeleton, respectively. The same data are displayed at three different view angles, one each per row.





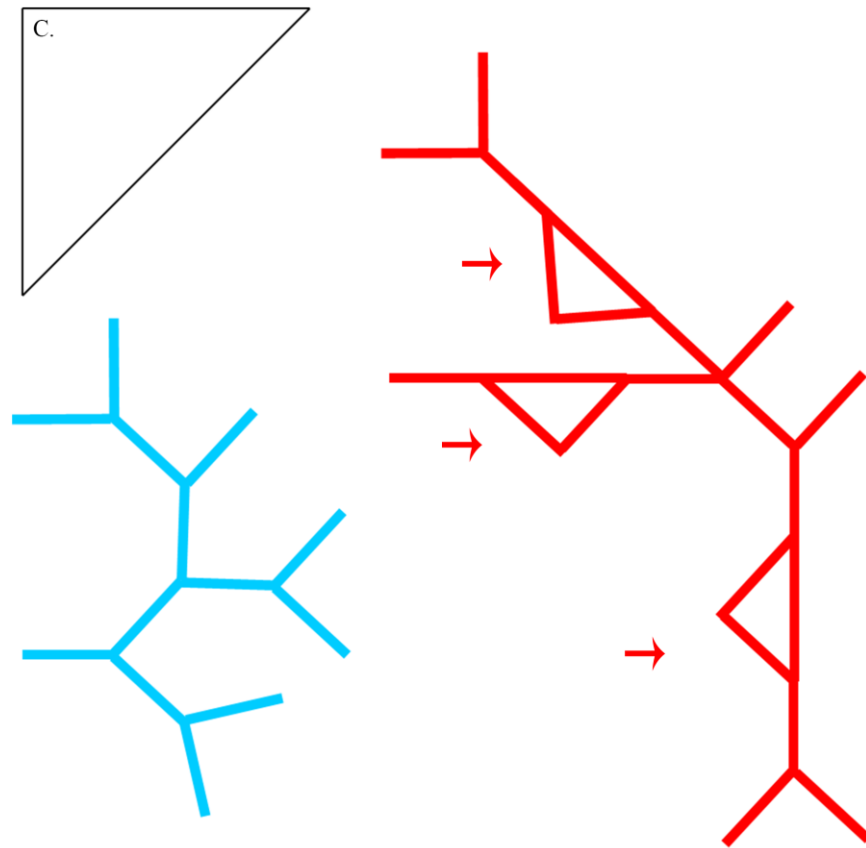


Figure 31. Branching pattern of sympathetic subtrees

A, Two examples of sympathetic subtrees in the subepicardial layer of the left ventricular free wall of a living hD β H-EGFP heart. The subtrees' trajectories (cyan and red traces in the right panel) were obtained by highlighting all axonal segments that were physically linked to their respective upstream reference points. The two reference points were chosen to be the entry point of a subtree initial segment into the imaged volume (cyan arrow) and the first branching point of a subtree close to its epicardial parent bundle (red arrow). Portions of the two-photon imaging data shown in Figure were used for subtree analyses. **B**, 3D renderings of the two skeletons in **A** from four different angles. **C**, Axograms of the two skeletonized trajectories in **B**. Asterisks denote start points for 3D tracing. Arrows denote axonal loops.

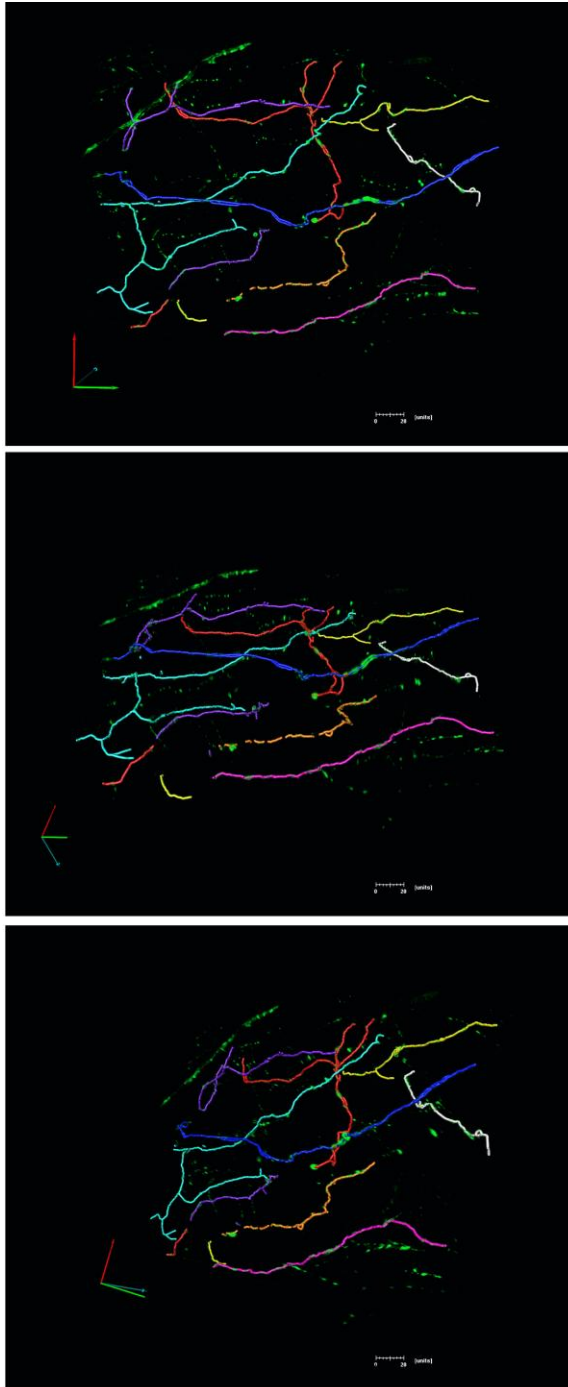
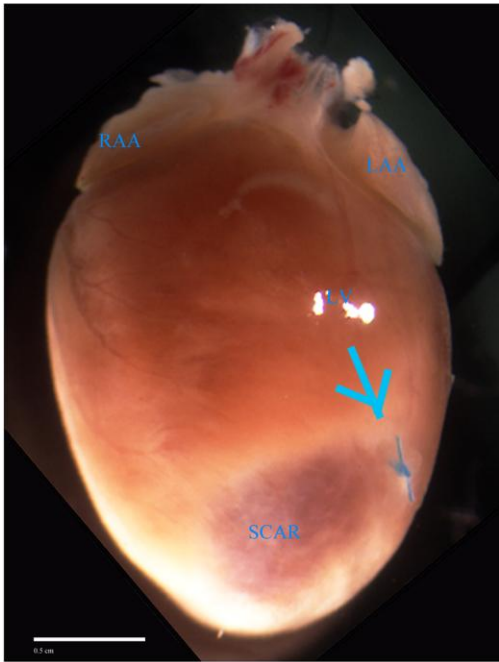


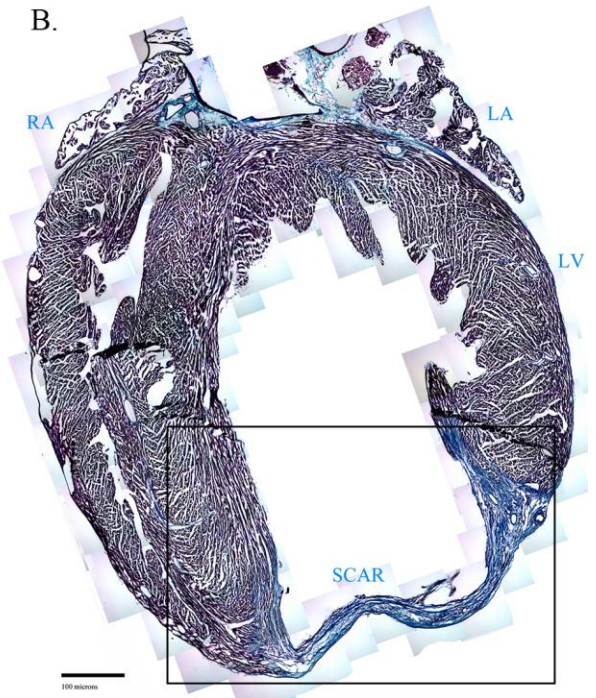
Figure 32. Subtree arbors arrange to not overlap very much within the local sympathetic network

Volume-rendered skeletons were obtained for each individually identified subtree using the 3D tracing algorithm and assigned different colors. The 3D color map is shown from three different view angles.

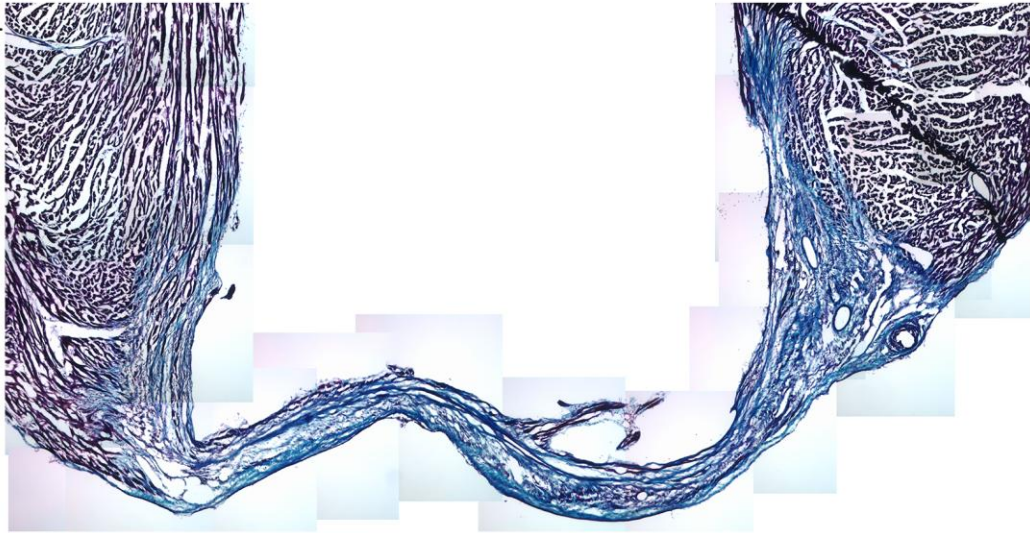
A.



B.



C.



D.

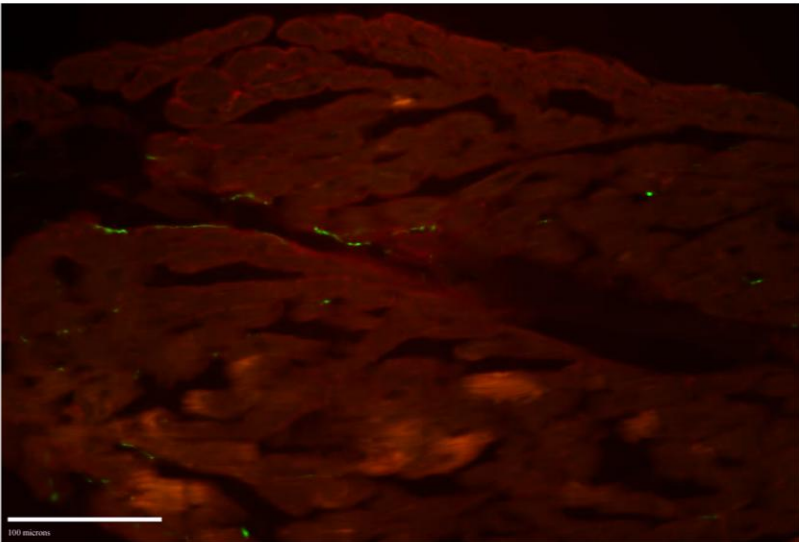
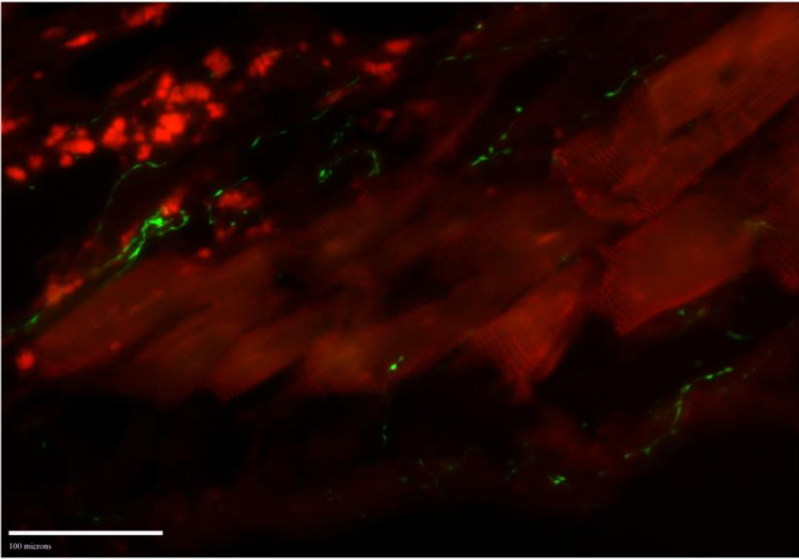
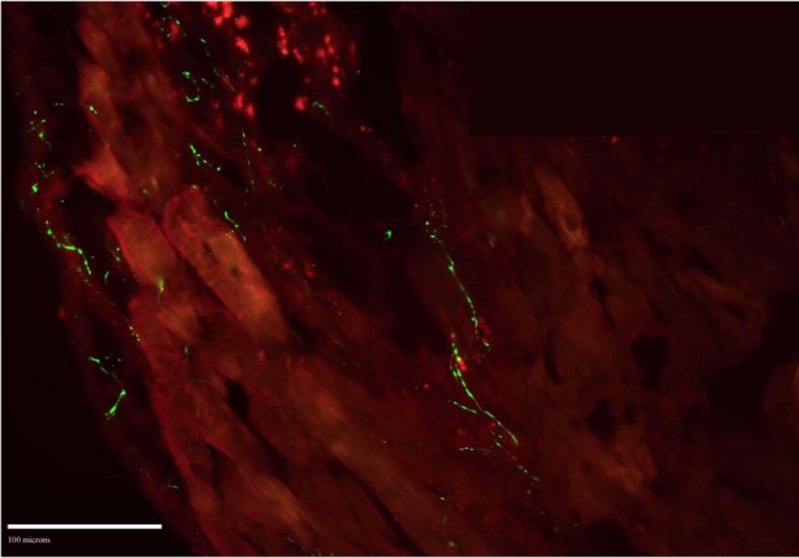


Figure 33. Sympathetic remodeling in chronically infarcted myocardium

A, Adult hD β H-EGFP heart with anterior myocardial infarction at two weeks after permanent ligation of the distal left anterior descending coronary artery. Arrow denotes ligation suture. Arrowheads outline infarct scar. RAA, right atrial appendage; LAA, left atrial appendage; LV, left ventricle; Scale bar, 5 mm. **B**, Masson's trichrome stain of a 10 μ m thick section from the heart in (A). Red: cytoplasm; blue: collagen. RA, right atrium; LA, left atrium; LV, left ventricle. Scale bar, 300 μ m. **C**, Magnified view of the boxed region in B. **D**, Dual immunostaining for tyrosine hydroxylase (green) and sarcomeric α -actinin (red) in the peri-infarct zone (upper two panels) and in a basal zone remote from the infarct (lower panel). Sections were obtained from the same heart shown in (A). Scale bar, 100 μ m.

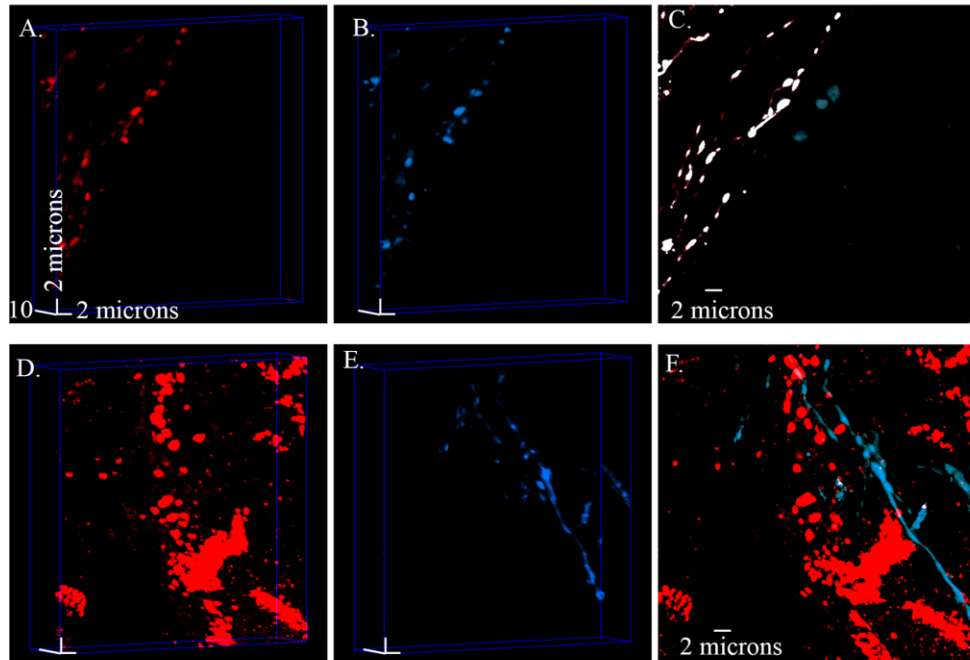


Figure 34. Determination of the empirical upper and lower limits of co-localization in infarcted non-transgenic heart

A and **B**, Pair of volume-rendered confocal z-stacks obtained from a cardiac section incubated with a tyrosine hydroxylase primary antibody and two secondary antibodies labeled with Alexa546 (**A**) or Alexa633 (**B**). The x, y and z dimensions of the imaged volume were 52.7, 52.7 and 10 μm , respectively. **C**, Co-localization map of the maximum intensity xy projection of the merged two-channel z-stack. If the pixel is white, then both fluorophores occupy that pixel. **D** and **E**, Pair of volume-rendered confocal z-stacks obtained from a cardiac section reacted with primary antibodies against Cx43 and tyrosine hydroxylase, followed by secondary antibodies conjugated with Alexa546 (**D**) and Alexa633 (**E**). **F**, Co-localization map of the maximum intensity xy projection of the two-channel merged z-stack.

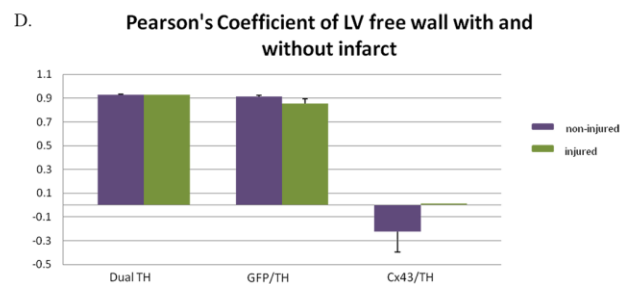
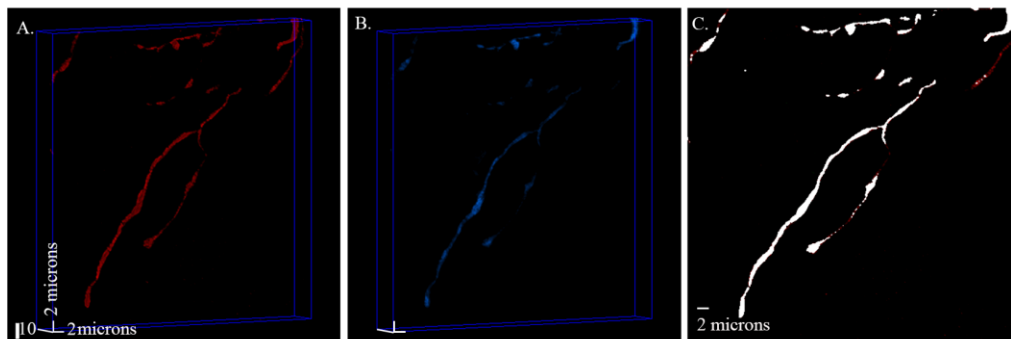
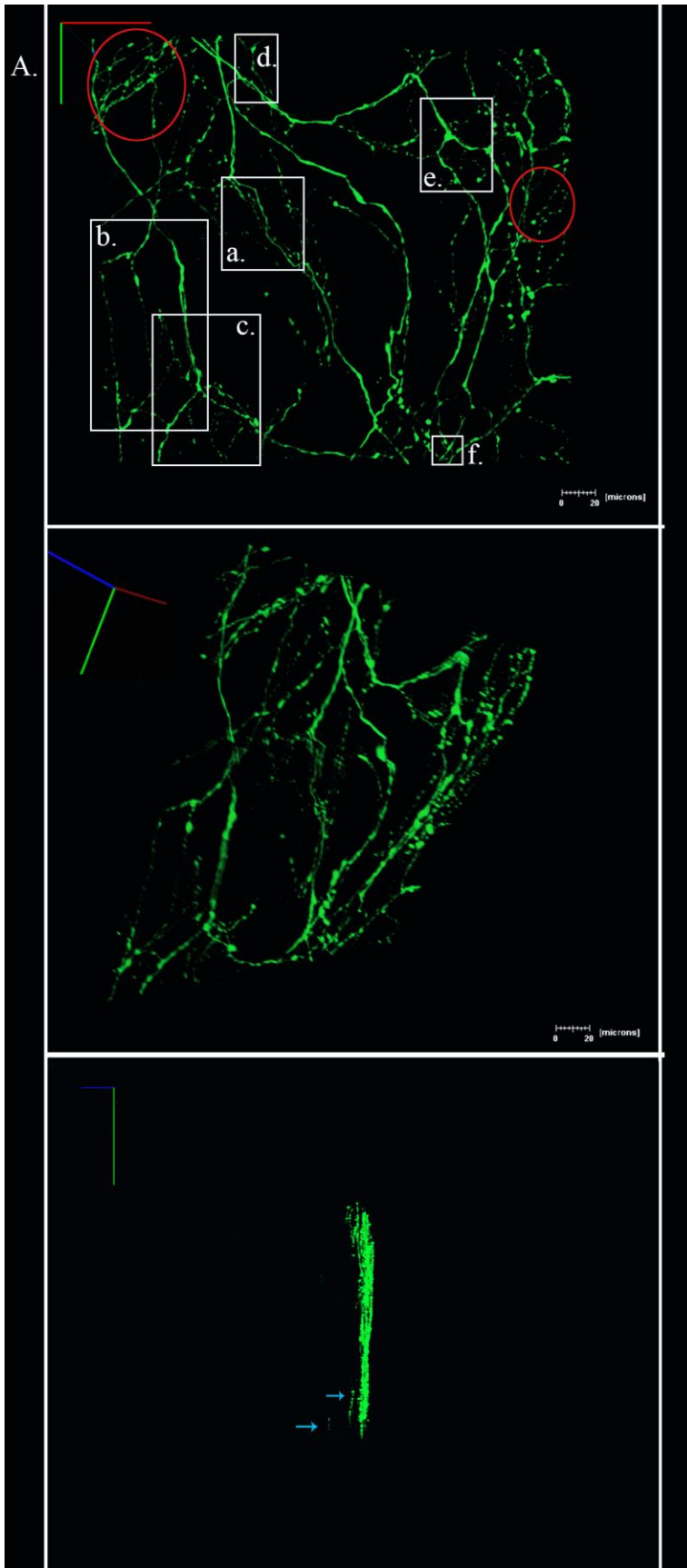
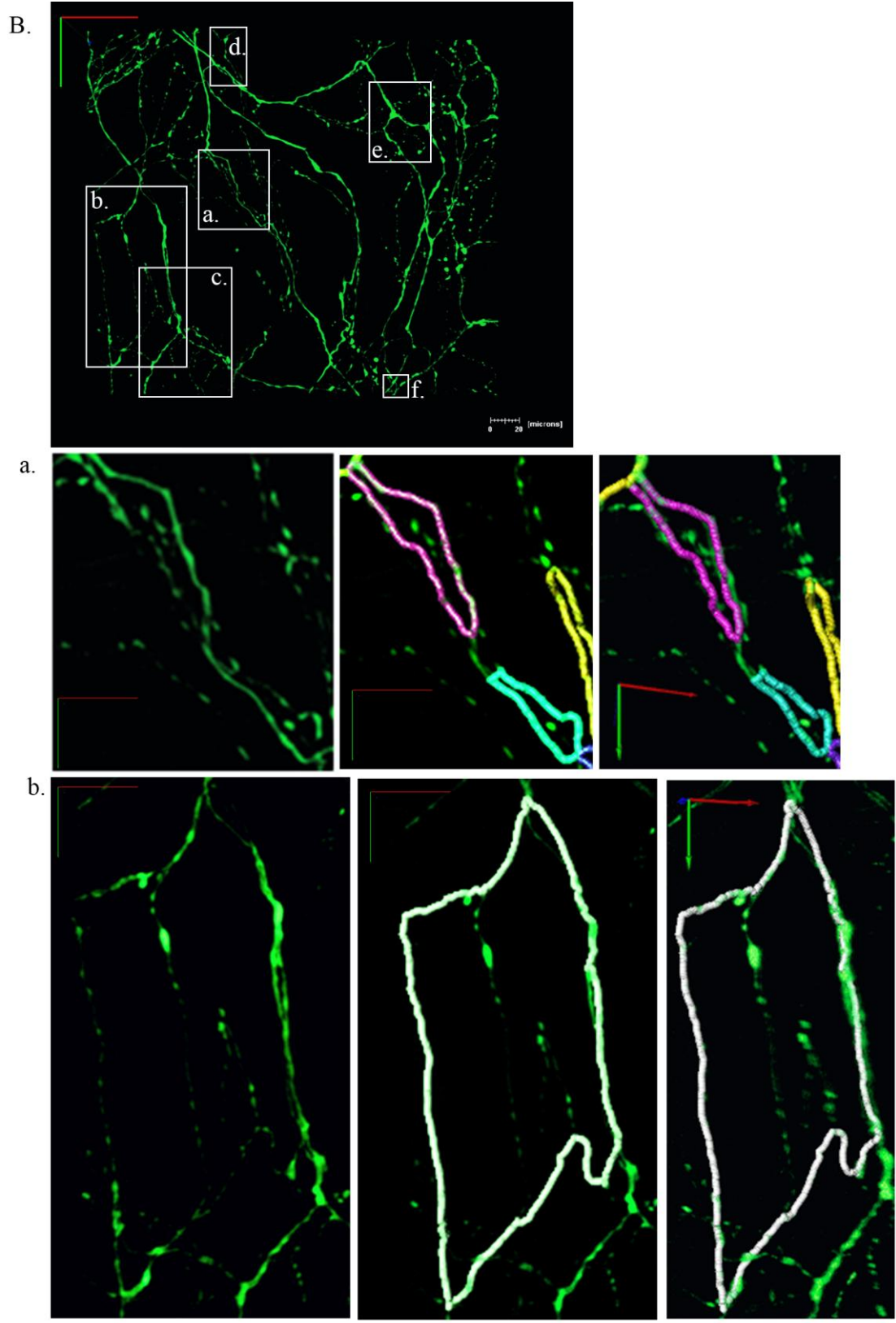


Figure 35. Intracardiac distribution of EGFP tracks sympathetic axons in chronically infarcted heart

A, Pair of volume-rendered confocal z-stacks obtained from a cardiac section ($52.7 \times 52.7 \times 10 \mu\text{m}^3$) co-stained with tyrosine hydroxylase (A; Alexa546 label) and GFP (B; Alexa633 label) antibodies. **C**, Co-localization map of the maximum intensity xy projection of the merged stack. If the pixel is white, both proteins occupy that pixel. **D**, Bar graphs of mean \pm SEM Pearson's co-localization coefficients for the peri-infarct zone and LV anterior free wall from infarcted and non-injured h β H-EGFP hearts, respectively. Values are from 5 image stacks each per region in a chronically infarcted heart. There was no significant difference between the injured and non-injured hearts ($P > 0.05$ by Kruskal-Wallis test for multiple comparisons).





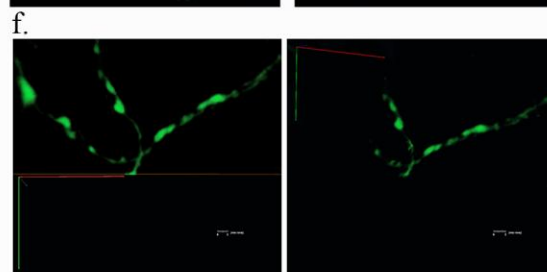
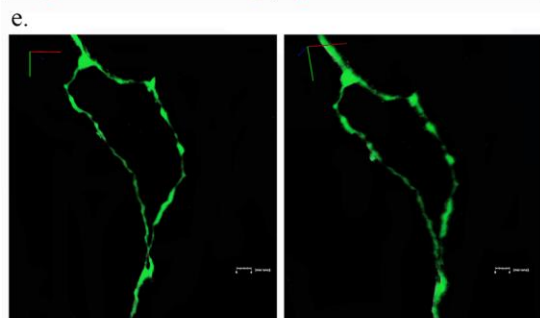
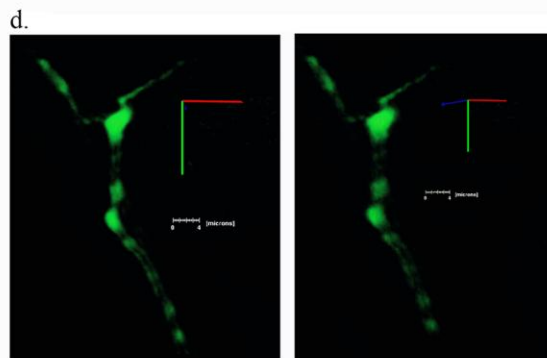
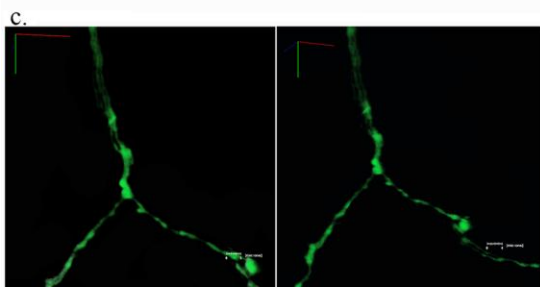
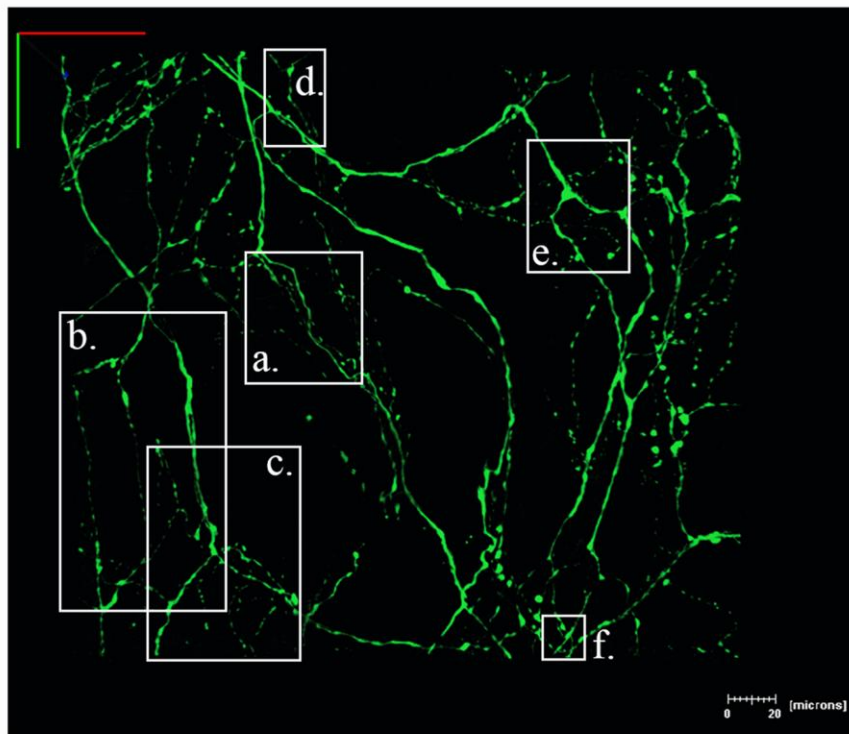


Figure 36. Three-dimensional reconstruction of the local sympathetic neurite network within the epicardial border zone of a 2-week-old myocardial infarction in a living, adult hD β H-EGFP heart

A, 3D rendering of the subepicardial sympathetic arbor from three different view angles. All sympathetic axons (labeled with EGFP) in a 250 μ m by 280 μ m by 50 μ m segment were imaged by TPLSM. A montage of 9 (3 x 3) overlapping image stacks provided the dataset for reconstruction using AMIRA software. Images (512 x 512) were collected at a voxel size of 0.2 μ m x 0.2 μ m x 0.5 μ m with 12-bit resolution. Arrowheads denote axonal fragments at increased tissue depth. **B**, Magnified views of the boxed regions labeled a through j in (A). a, two connected loops of short length; b, axonal loop with long circumferential length; c and d, branching of dual-axon bundles while their constituent axons do not branch; e, bifurcation and punctuated pattern; f, trifurcation and punctuated pattern.

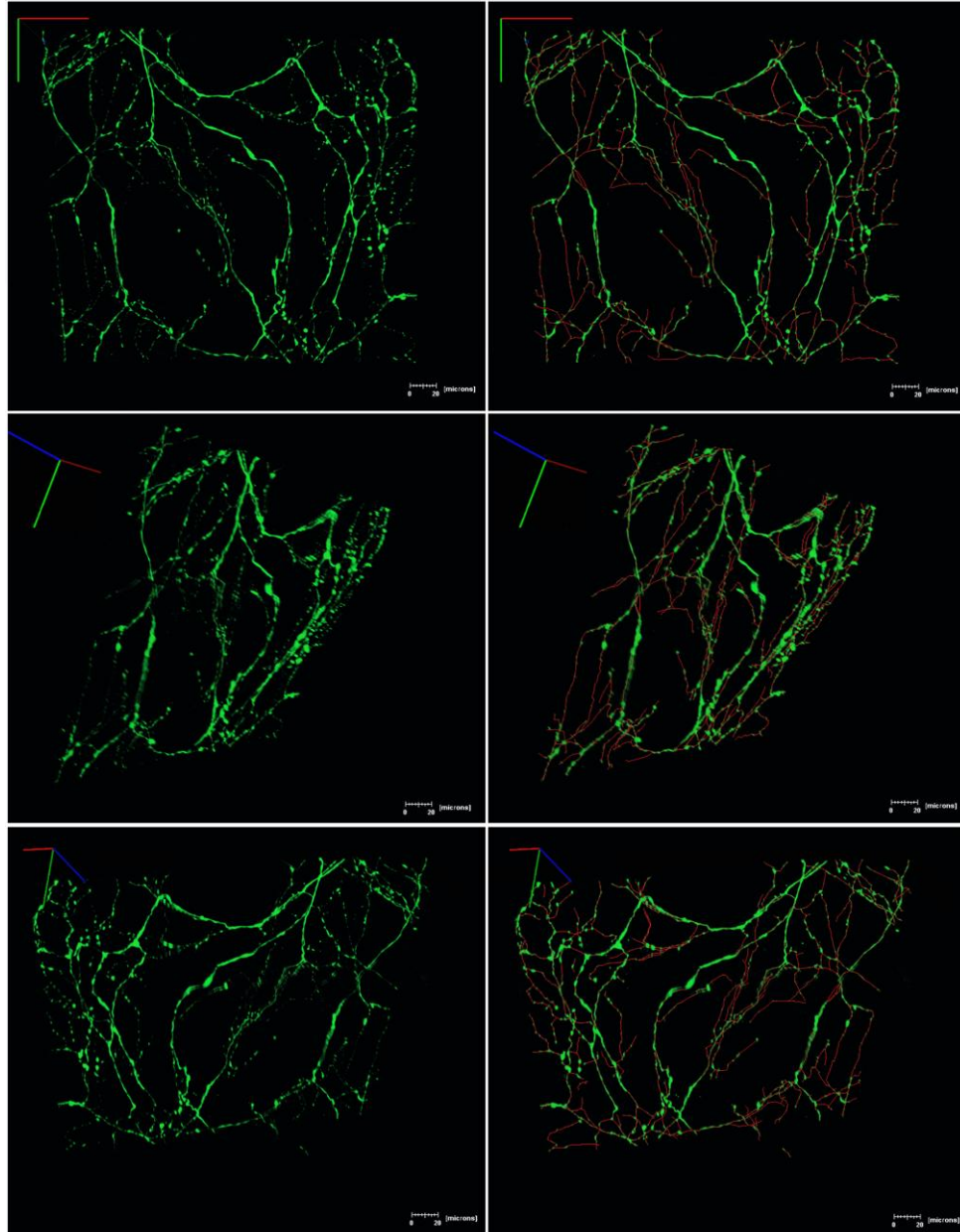


Figure 37. *3D rendering of the skeletonized sympathetic arbor within a finite volume of the epicardial border zone of a 2-week-old myocardial infarction in a living $h\beta H$ -EGFP heart*

A complete 3D skeleton (red tracings) of all green fluorescent neurites was generated using the semi-automated tracing algorithm and superimposed onto the 3D rendering of the two-photon image data. The 3D rendering of the overlay is shown from three different view angles (A – C).

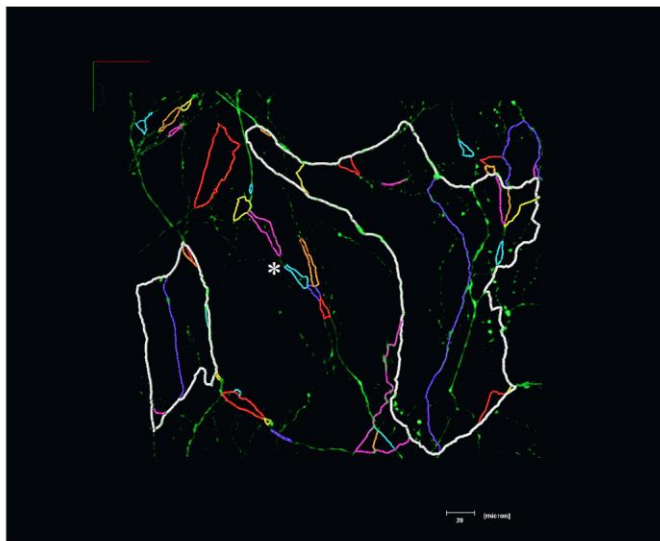
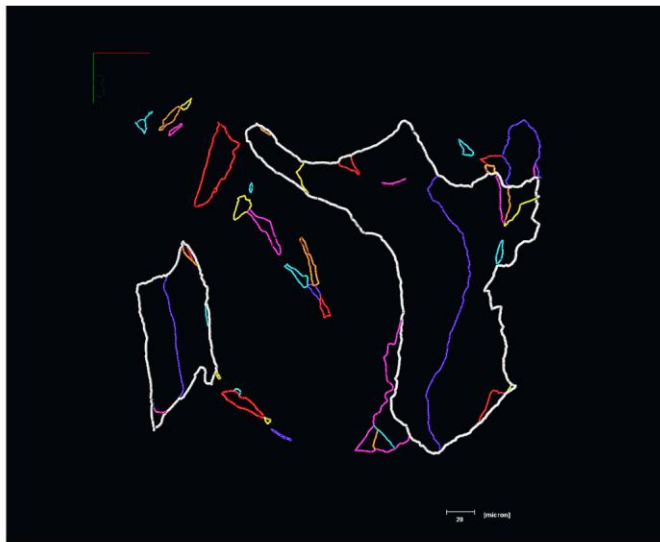
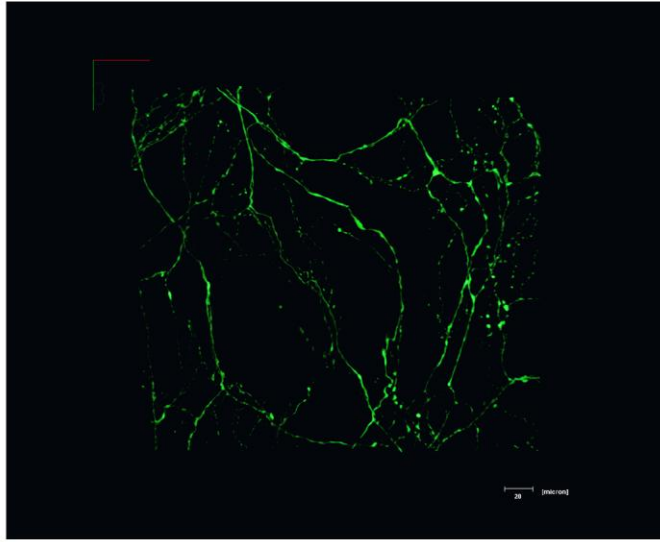


Figure 38. Multiple-loop architecture of the sympathetic circuitry in the epicardial infarct border zone

Individual loops that were found to be physically linked with each other within selected subvolumes were identified and tracked sequentially in 3D. Their colored trajectories were superimposed onto the volume-rendered two-photon image data to generate a loop map. 3D overlays are presented from three different view angles. Arrowheads denote juxtaposed loops linked in series via short axonal segments.

IV. References

1. Brodal, P., ed. *The Central Nervous System: Structure and Function*. 3rd ed. 2004, Oxford University Press US.
2. Hassankhani, A., et al., *Overexpression of NGF within the Heart of Transgenic Mice Causes Hyperinnervation, Cardiac Enlargement, and Hyperplasia of Ectopic Cells*. *Developmental Biology*, 1995. 169(1): p. 309-321.
3. Shcherbakova, O.G., et al., *Organization of β_2 -adrenoceptor signaling compartments by sympathetic innervation of cardiac myocytes*. *The Journal of Cell Biology*, 2007. 176(4): p. 521-533.
4. Mercer, E.H., et al., *The dopamine [β]-hydroxylase gene promoter directs expression of *E. coli lacZ* to sympathetic and other neurons in adult transgenic mice*. *Neuron*, 1991. 7(5): p. 703-716.
5. Gibbins, P.J.a.l., *Electrophysiological and Morphological Diversity of Mouse Sympathetic Neurons*. *Journal of Neurophysiology*, 1999. 82: p. 2747-2764
6. Silverthorn, D.U., *Human Physiology an integrated approach*. fifth ed 2010. Pearson/Benjamin Cummings.
7. Rubenstein, L.A., R.J. Zauhar, and R.G. Lanzara, *Molecular dynamics of a biophysical model for β_2 -adrenergic and G protein-coupled receptor activation*. *Journal of Molecular Graphics and Modelling*, 2006. 25(4): p. 396-409.
8. Zhong, J., J.R. Hume, and K.D. Keef, *β_2 -Adrenergic receptor stimulation of L-type Ca^{2+} channels in rabbit portal vein myocytes involves both β_1 and β_3 G protein subunits*. *The Journal of Physiology*, 2001. 531(1): p. 105-115.
9. Norris, G.W., *Cardiac Arrhythmia. From a practical standpoint in light of recent investigations*. *The American Journal of the Medical Sciences*, 1908. 136(1): p. 46-66.
10. Inoue, H. and D. Zipes, *Results of sympathetic denervation in the canine heart: supersensitivity that may be arrhythmogenic*. *Circulation*, 1987. 75(4): p. 877-887.
11. Miyazaki, T., H.P. Pride, and D.P. Zipes, *Modulation of cardiac autonomic neurotransmission by epicardial superfusion. Effects of hexamethonium and tetrodotoxin*. *Circulation Research*, 1989. 65(5): p. 1212-9.

12. Zipes, D.P. and M. Rubart, *Neural modulation of cardiac arrhythmias and sudden cardiac death*. Heart Rhythm, 2006. 3(1): p. 108-13.
13. Kimura, K., M. Ieda, and K. Fukuda, *Development, maturation, and transdifferentiation of cardiac sympathetic nerves*. Circ Res, 2012. 110(2): p. 325-36.
14. Mühlfeld, C., et al., *An unbiased stereological method for efficiently quantifying the innervation of the heart and other organs based on total length estimations*. Journal of Applied Physiology, 2010. 108(5): p. 1402-1409.
15. Shcherbakova, O.G., et al., *Organization of beta-adrenoceptor signaling compartments by sympathetic innervation of cardiac myocytes*. J Cell Biol, 2007. 176(4): p. 521-33.
16. Wei, D.-S., et al., *Compartmentalized and Binary Behavior of Terminal Dendrites in Hippocampal Pyramidal Neurons*. Science, 2001. 293(5538): p. 2272-2275.
17. Swadlow HA, K.J., Waxman SG., *Modulation of impulse conduction along the axonal tree*. Annu Rev Biophys Bioeng., 1980. 9: p. 143-179.
18. Ferrante M, M.M., Ascoli GA, *Functional impact of dendritic branch-point morphology*. J Neurosci., 2013. 33(5): p. 2156-65.
19. Kamino, K., *Optical approaches to ontogeny of electrical activity and related functional organization during early heart development*. Physiological Reviews, 1991. 71(1): p. 53-91.
20. Liu, Q.-Y., et al., *Sympathetic innervation modulates repolarizing K⁺ currents in rat epicardial myocytes*. Am J Physiol Heart Circ Physiol, 1998. 274(3): p. H915-922.
21. Ieda, M., et al., *Sema3a maintains normal heart rhythm through sympathetic innervation patterning*. Nat Med, 2007. 13(5): p. 604-612.
22. Protas, L., et al., *Neuropeptide Y Is an Essential In Vivo Developmental Regulator of Cardiac I_{Ca,L}*. Circulation Research, 2003. 93(10): p. 972-979.
23. Ji-Fang Zhang, R.B.R., Steven A. Siegelbaum, *Sympathetic neurons mediate developmental change in cardiac sodium channel gating through long-term neurotransmitter action*. Neuron, 1992. 9(1): p. 97-103.

24. Hopkins DA, A.J., *Localization of sympathetic postganglionic and parasympathetic preganglionic neurons which innervate different regions of the dog heart.* J Comp Neurol., 1984. 229(2): p. 186-98.
25. Zhou, S., et al., *Mechanisms of Cardiac Nerve Sprouting After Myocardial Infarction in Dogs.* Circulation Research, 2004. 95(1): p. 76-83.
26. Cao, J.-M., et al., *Relationship Between Regional Cardiac Hyperinnervation and Ventricular Arrhythmia.* Circulation, 2000. 101(16): p. 1960-1969.
27. Shelton, D.L. and L.F. Reichardt, *Expression of the beta-nerve growth factor gene correlates with the density of sympathetic innervation in effector organs.* Proceedings of the National Academy of Sciences, 1984. 81(24): p. 7951-7955.
28. Ieda, M., et al., *Nerve Growth Factor Is Critical for Cardiac Sensory Innervation and Rescues Neuropathy in Diabetic Hearts.* Circulation, 2006. 114(22): p. 2351-2363.
29. Heath BM, X.J., Dong E, An RH, Brooks A, Liang C, Federoff HJ, Kass RS. , *Overexpression of nerve growth factor in the heart alters ion channel activity and beta-adrenergic signalling in an adult transgenic mouse.* J Physiol, 1998. 512(Pt. 3): p. 779-91.
30. Lamé, M.W., et al., *Protein Targets of Monocrotaline Pyrrole in Pulmonary Artery Endothelial Cells.* Journal of Biological Chemistry, 2000. 275(37): p. 29091-29099.
31. Kimura, K., et al., *Cardiac sympathetic rejuvenation: a link between nerve function and cardiac hypertrophy.* Circ Res, 2007. 100(12): p. 1755-64.
32. Cao, J.-M., et al., *Nerve Sprouting and Sudden Cardiac Death.* Circ Res, 2000. 86(7): p. 816-821.
33. Stanton, M.S., et al., *Regional sympathetic denervation after myocardial infarction in humans detected noninvasively using I-123-metaiodobenzylguanidine.* J Am Coll Cardiol, 1989. 14(6): p. 1519-26.
34. Stanton, M.S. and D.P. Zipes, *Modulation of drug effects by regional sympathetic denervation and supersensitivity.* Circulation, 1991. 84(4): p. 1709-14.
35. Charkoudian, N. and J.A. Rabbitts, *Sympathetic Neural Mechanisms in Human Cardiovascular Health and Disease.* Mayo Clinic Proceedings, 2009. 84(9): p. 822-830.

36. Chen, P.-S., et al., *Sympathetic nerve sprouting, electrical remodeling and the mechanisms of sudden cardiac death*. Cardiovascular Research, 2001. 50(2): p. 409-416.
37. Pawley, J.B., ed. *Handbook of Biological Microscopy*. 3rd ed. 2006, Springer Science + Business Media, LLC: New York, NY.
38. Blaufuss Medical Multimedia Laboratories. *Heart Sounds and Cardiac Arrhythmias*. Available from: <http://www.blaufuss.org/>.
39. Rubart, M., *Two-Photon Microscopy of Cells and Tissue*. Circ Res, 2004. 95(12): p. 1154-1166.
40. Hanson, K.M., et al., *Two-Photon Fluorescence Lifetime Imaging of the Skin Stratum Corneum pH Gradient*. Biophysical Journal, 2002. 83(3): p. 1682-1690.
41. Yunzhou Shi, D.Z., Terry B. Huff, Xiaofei Wang, Riyi Shi, Xiao-Ming Xu, and Ji-Xin Chenga, *Longitudinal in vivo coherent anti-Stokes Raman scattering imaging of demyelination and remyelination in injured spinal cord*. Journal of Biomedical Optics, 2011. 16(10).
42. Ding, J.B., K.T. Takasaki, and B.L. Sabatini, *Supraresolution Imaging in Brain Slices using Stimulated-Emission Depletion Two-Photon Laser Scanning Microscopy*. Neuron, 2009. 63(4): p. 429-437.
43. Helmchen, F. and W. Denk, *Deep tissue two-photon microscopy*. Nat Meth, 2005. 2(12): p. 932-940.
44. Warren R. Zipfel, R.M.W., Richard Christie, Alexander Yu Nikitin, Bradley T. Hyman, and Watt W. Webb, *Live tissue intrinsic emission microscopy using multiphoton-excited native fluorescence and second harmonic generation*. Proc Natl Acad Sci U S A, 2003. 100(12): p. 7075-7080.
45. Ghosh, A.N.v.d.P.a.P.K., *Selective Neuronal Expression of Green Fluorescent Protein with Cytomegalovirus Promoter Reveals Entire Neuronal Arbor in Transgenic Mice* Journal of Neurosciences, 1998. 18(24): p. 10640-10651.
46. Abematsu, M., et al., *Neurons derived from transplanted neural stem cells restore disrupted neuronal circuitry in a mouse model of spinal cord injury*. The Journal of Clinical Investigation, 2010. 120(9): p. 3255-3266.
47. Ori-McKenney, K. and R. Vallee, *Neuronal migration defects in the Loa dynein mutant mouse*. Neural Development, 2011. 6(1): p. 26.

48. Holtmaat, A., et al., *Imaging of experience-dependent structural plasticity in the mouse neocortex in vivo*. Behavioural Brain Research, 2008. 192(1): p. 20-25.
49. Livet, J., et al., *Transgenic strategies for combinatorial expression of fluorescent proteins in the nervous system*. Nature, 2007. 450(7166): p. 56-62.
50. Sakurai, T., et al., *Structure and Function of Human Prepro-orexin Gene*. Journal of Biological Chemistry, 1999. 274(25): p. 17771-17776.
51. Hogan B, C.F., lacy L, *Manipulating the Mouse Embryo - A Laboratory Manual*, 1986, Cold Spring Harbor Laboratory: New York.
52. Rubart M, P.K., Nakajima H, Soonpaa MH, Nakajima HO, Field LJ., *Physiological coupling of donor and host cardiomyocytes after cellular transplantation*. Circ Res, 2003. 92(11): p. 1217-24.
53. Scriven, D.R.L., R.M. Lynch, and E.D.W. Moore, *Image acquisition for colocalization using optical microscopy*. American Journal of Physiology - Cell Physiology, 2008. 294(5): p. C1119-C1122.
54. Rasband, W. *Online Manual for the WCIF-ImageJ collection*. Available from:
http://www.uhnresearch.ca/facilities/wcif/imagej/about_this_manual.htm.
55. Herz, J., et al., *Expanding Two-Photon Intravital Microscopy to the Infrared by Means of Optical Parametric Oscillator*. Biophysical Journal. 98(4): p. 715-723.
56. Young PA, C.S., Byars JM, Decca RS, Dunn KW., *The effects of spherical aberration on multiphoton fluorescence excitation microscopy*. J Microsc., 2011. 242(2): p. 157-65.
57. Kawano H, K.T., Abe Y, Mizuno H, Miyawaki A., *Two-photon dual-color imaging using fluorescent proteins*. Nat Methods., 2008. 5(5): p. 373-4.
58. J., P., *Immunohistochemical evidence for dopaminergic neurons in the rat superior cervical ganglion*. Proc R Soc Lond B Biol Sci, 1984. 222(1228): p. 357-62.
59. McGowan R, C.R., Peterson A, Sapienza C., *Cellular mosaicism in the methylation and expression of hemizygous loci in the mouse*. Genes Dev., 1989. 3(11): p. 1669-76.

60. Huang WY, A.J., Douglas PS, Izumo S. , *Transgenic expression of green fluorescence protein can cause dilated cardiomyopathy*. Nat Med., 2000. 6(5): p. 482-3.
61. Liu, H.S., Jan, M.S., Chou, C.K., Chen, P.H., and Ke, N.J., *Is green fluorescent protein toxic to the living cells?* Biochem. Biophys. Res. Commun, 1999. 260: p. 712-717.
62. Anderson RH, S.M., Sanchez-Quintana D, Loukas M, Lunkenheimer PP., *The three-dimensional arrangement of the myocytes in the ventricular walls*. Clin Anat., 2009. 22(1): p. 64-76.
63. Satoh H, D.L., Blatter LA, Bers DM., *Surface:volume relationship in cardiac myocytes studied with confocal microscopy and membrane capacitance measurements: species-dependence and developmental effects*. Biophys J., 1996. 70(3): p. 1494-504.
64. Kass, M., Wittkin, A., Terzopoulos, D, *Snakes: active contour models*. Int. J. Comp. Vis, 1988. 1(4): p. 321-331.
65. Long JB, S.S., *Quantifying perivascular sympathetic innervation: regional differences in male C57BL/6 mice at 3 and 20 months*. J Neurosci Methods., 2009. 184(1): p. 124-8.
66. Cabo C, Y.J., Boyden PA, Chen S, Hussain W, Duffy HS, Ciaccio EJ, Peters NS, Wit AL, *Heterogeneous gap junction remodeling in reentrant circuits in the epicardial border zone of the healing canine infarct*. Cardiovasc Res, 2006. 72(2): p. 241-9.
67. Vladimirov N, T.Y., Traub RD., *Shortest Loops are Pacemakers in Random Networks of Electrically Coupled Axons*. Front Comput Neurosci., 2012. 6(17).
68. Feng G, M.R., Bernstein M, Keller-Peck C, Nguyen QT, Wallace M, Nerbonne JM, Lichtman JW, Sanes JR., *imaging neuronal subsets in transgenic mice expressing multiple spectral variants of GFP*. Neuron, 2000. 28(1): p. 41-51.
69. Kanazawa H, I.M., Kimura K, Arai T, Kawaguchi-Manabe H, Matsushashi T, Endo J, Sano M, Kawakami T, Kimura T, Monkawa T, Hayashi M, Iwanami A, Okano H, Okada Y, Ishibashi-Ueda H, Ogawa S, Fukuda K, *Heart failure causes cholinergic transdifferentiation of cardiac sympathetic nerves via gp130-signaling cytokines in rodents*. J Clin Invest, 2010. 120(2): p. 408-21.

70. Xie W, S.J., Mao J, Zhang JM. , *Highly localized interactions between sensory neurons and sprouting sympathetic fibers observed in a transgenic tyrosine hydroxylase reporter mouse*. Mol Pain, 2011. 7(53).
71. Li W, K.D., Van Winkle DM, Habecker BA., *Infarction alters both the distribution and noradrenergic properties of cardiac sympathetic neurons*. Am J Physiol Heart Circ Physiol., 2004. 286(6): p. H2229-36.
72. Bruce AF, R.S., Dupont E, Severs NJ., *Gap junction remodelling in human heart failure is associated with increased interaction of connexin43 with ZO-1*. Cardiovasc Res, 2008. 77(4): p. 757-65.
73. Clarke GL, B.A., Tague SE, Hasan W, Smith PG., *β -adrenoceptor blockers increase cardiac sympathetic innervation by inhibiting autoreceptor suppression of axon growth*. J Neurosci., 2010. 30(37): p. 12446-54.
74. Goldfinger MD, R.V., Pearson JC., *Theoretical studies of impulse propagation in serotonergic axons*. Biol Cybern, 1992. 66(5): p. 399-406.
75. Debanne D, C.E., Bialowas A, Carlier E, Alcaraz G., *Axon physiology*. Physiol. Rev., 2011. 91(2): p. 555-602.
76. Schmidt-Hieber C, J.P., Bischofberger J., *Action potential initiation and propagation in hippocampal mossy fibre axons*. J Physiol, 2009. 586(7): p. 1849-57.
77. Andersen P, S.A., Raastad M, *The hippocampal lamella hypothesis revisited*. Brain Research, 2000. 886(1-2): p. 165-171.
78. Rueckel M, M.-B.J., Denk W., *Adaptive wavefront correction in two-photon microscopy using coherence-gated wavefront sensing*. Proc Natl Acad Sci U S A, 2006. 103(46): p. 17137-42.
79. Shimosawa T, Y.K., Kondo T, Hayashi S, Shitamukai A, Konno D, Matsuzaki F, Takayama J, Onami S, Nakayama H, Kosugi Y, Watanabe TM, Fujita K, Mimori-Kiyosue Y., *Improving spinning disk confocal microscopy by preventing pinhole cross-talk for intravital imaging*. Proc Natl Acad Sci U S A, 2013. 119(9): p. 3399-404.
80. Nagatsu, T., M. Levitt, and S. Udenfriend, *Tyrosine Hydroxylase*. Journal of Biological Chemistry, 1964. 239(9): p. 2910-2917.
81. Knollmann, B.C. and D.M. Roden, *A genetic framework for improving arrhythmia therapy*. Nature, 2008. 451(7181): p. 929-936.

82. Schmitt, S., et al., *New methods for the computer-assisted 3-D reconstruction of neurons from confocal image stacks*. NeuroImage, 2004. 23(4): p. 1283-1298.

Curriculum Vitae

Kim Renee Freeman

Education

Ph.D., Biomedical Imaging and Biophysics
Indiana University, Indianapolis, IN.....2013

M.S., Cell Biology (Lipid Biophysics)
Purdue School of Science, Indianapolis, IN2006

B.S., Cell & Structural Biology (minor in Chemistry)
University of Illinois, Urbana-Champaign, IL1998

Professional Experience

PCR, electrophoresis, immunohistochemistry, immunocytochemistry, cryosectioning, epifluorescent microscopy, confocal microscopy, two-photon microscopy, transmission electron microscopy, intravital imaging, langendorff perfusion, western blotting, image analysis and rendering, cell culture, aseptic technique, cell transfection, laboratory organization, TLC, iontophoresis, organic synthesis, epifluorescent microscopy, immunohistochemistry, immunocytochemistry, proliferation assays, cellular adhesion assays, HPLC, organic synthesis, lyophilization, teaching basic laboratory techniques, exam development, exam proctoring

Papers

Freeman K, Tao W, Sun H, Soonpaa MH, Rubart M. In situ three-dimensional reconstruction of mouse heart sympathetic innervation by two-photon excitation fluorescence imaging. J Neurosci Methods. 2013 Sep 18 [Epub ahead of print].

Min Wu, Kevin Harvey, Nargiz Ruzmetov, Zachary Welch, Laura Sech, Kim Jackson, William Stillwell, Gary Zaloga, and Rafat Siddiqui. Omega-3 polyunsaturated fatty acids attenuate breast cancer growth through activation of a neutral sphingomyelinase-mediated pathway. Int. J. Cancer: 117, 340-348 (2005).

Published Abstracts for Talks at Regional Conferences

38th annual South Eastern Regional Lipid Conference, Nov 12-14, 2003. The Mediterranean Diet: a molecular study. Kim Jackson, Rafat Siddiqui, SR Shaikh, Alicia Castillo, Mustapha Zeruga, and William Stillwell.

36th annual Central Regional Meeting of the American Chemical Society, June 2-4, 2004 Synthesis and characterization of novel fatty acid conjugated anti-cancer agents Kim Jackson, Rafat Siddiqui, and William Stillwell

39th annual South Eastern Regional Lipid Conference, Nov 3-5 2004 Development and characterization of a novel anti-cancer agent using a polyunsaturated fatty acid conjugated to a commonly utilized anesthetic Kim Jackson, Rafat Siddiqui, and William Stillwell

3rd Annual Spring Meeting of the Indiana Microscopy Society, April 20, 2007. TPLSM Quantification of Intact Heart Sympathetic Innervation. Kim Jackson and Michael Rubart

Microscopy and Microanalysis, August 3-7, 2008. Imaging Cardiac Sympathetic Neurons: a Correlative Study Using Fluorescence and TEM. Kim Jackson, Caroline Miller, Vince Gattone, and Michael Rubart

34th Annual Midwest Pediatric Cardiology Society Scientific Session. September 23-24, 2010. Three dimensional Imaging of Sympathetic Innervation in Living Heart. Kim Freeman and Michael Rubart

Published Abstracts for Posters

Federation of American Societies for Experimental Biology March 31-April 5, 2005. Synthesis and characterization of a novel fatty acid conjugated anti-cancer agent. Kim Jackson, Rafat Siddiqui, and William Stillwell

International Gap Junction Conference, British Columbia August 13-18 2005. The Role of docosahexaenoic acid and PKC in connexin43 phosphorylation regulated gap junction intercellular signaling. Kim Jackson, William Stillwell, Rafat Siddiqui, Alonso Moreno

Permeability and directional selectivity of heteromeric Cx43-Cx45 depends on permeant charge and is regulated by phosphorylation. Osman Ahmed, Faraz Sandhu, Kim Jackson, Alonso Moreno.

American Heart Association Scientific Sessions, Orlando, FL. Nov14-18, 2009. Two-Photon Fluorescence Imaging of Sympathetic Innervation in Living Mouse Heart. Kim Freeman and Michael Rubart

Other Skills and Qualifications

Image Analysis: Image J, Fiji, Amira, Neurolucida, Zeiss LSM, Olympus Fluoview, Voxx, Photoshop (CS3, CS4, & CS5), Metamorph. Office tools: Microsoft Office 2003/2007/2010 including Microsoft Excel, Microsoft Word, and Microsoft PowerPoint in all formats, Endnote, Mozilla Firefox, Internet Explorer, Windows Movie Maker, Adobe Acrobat 9/X Pro, Adobe Flash, Adobe Dreamweaver, Adobe Captivate.